

UNIVERSITY OF BELGRADE
FACULTY OF MECHANICAL ENGINEERING



MOHAMED ETOUHAMI M. SWEI

**CREEP CRACK GROWTH IN
STEEL WELDED JOINTS**

DOCTORAL DISSERTATION

BELGRADE 2018

УНИВЕРЗИТЕТ У БЕОГРАДУ
МАШИНСКИ ФАКУЛТЕТ



МОХАМЕД ЕТОУХАМИ М. СВЕИ

**РАСТ ПРСЛИНЕ УСЛЕД ПУЗАЊА У
ЗАВАРЕНИМ СПОЈЕВИМА ОД
ЧЕЛИКА**

Докторска дисертација

БЕОГРАД, 2018

Dedicated to my parents, wife, kids, and mentors

Mentor of Doctoral Dissertation

Prof. Dr. Aleksandar Sedmak

University of Belgrade, Faculty of Mechanical Engineering

Members of Committee

Dr. Aleksandar Sedmak

Faculty of Mechanical Engineering, Belgrade

Dr. Aleksandar Grbović

Faculty of Mechanical Engineering, Belgrade

Dr. Gordana Bakić

Faculty of Mechanical Engineering, Belgrade

Dr. Zorana Golubović

Innovation Center of Faculty of Mechanical Engineering, Belgrade

Dr. Ljubica Milović

Faculty of Technology and Metallurgy, Belgrade

Date of Defense:

ACKNOWLEDGEMENT

I wish to express my thanks to my supervisor and mentor Dr. Aleksandar Sedmak for his comprehensive and informative discussions valuable guidance and support, the same encouragement and dedication has also been extended to me by Dr. Aleksandar Grbović, whom I learned a great deal from his experience and knowledge of finite element codes which implemented in my experimental validations. Appreciation is also extended to Dr. Blagoj Petrovski who was generous with his insight and guidance and contributions of experimental data, I learned how to conduct numerical and experimental fracture mechanics in related work to my study.

The appreciation is extended to my friend Mr. Simon Sedmak for his time and efforts and my Libyan colleagues for their support.

I sincerely thank my mother and father for their devoted love, encouragement, and support. Finally, I am grateful to my wife Amal, my daughters Eman, Noor, Mawada, Hedaya, and son Abduraouf for their love, encouragement, and understanding throughout my long endeavor.

CREEP CRACK GROWTH IN STEEL WELDED JOINTS

ABSTRACT:

The welding technology is one of the most commonly used methods to join structural components in power plants. This operation may lead to strong modifications of the mechanical properties of the base metal, which is obviously the case for P91 steel. The present study aims at predicting the creep flow and damage behavior of welded components made of P91 steel. Study of the high temperature creep analyses of welded structures, as well as material properties generation, stress analysis, parametric considerations, and components failure life assessment [1]. High chromium alloy steel P91 (9Cr1Mo-NbV) is highly required in high-temperature productions facilities. Operating under creep conditions, i.e. high temperature and/or high stress, the welds made from this steel are potential failure locations and, therefore, life-limiting for the entire plant. In this thesis, the results of creep and creep crack growth (CCG) tests, which were conducted on P91 welds, are reported. These tests were carried out on welds constituents, i.e. base metal (BM) and weld metal (WM), and heat affected zone (HAZ), for the P91 material at 600°C. For the cross-weld tests, interest was focused on the Type IV region, a narrow zone at one end of the heat affected zone (HAZ) at the side of the BM. Also reported, in this thesis, are the results of the Finite Element analyses for predicting the creep and creep crack growth in the P91 weldment.

The P91 steel weldment is considered for investigations of creep behavior and creep crack growth at the service temperature of 600 °C, creep crack growth was experimentally carried out on CT specimen for different weldment zones. The mechanical properties and data collected from numerous tensile creep testing, crack initiations and creep crack growth tests are analyzed according to standard codes, the assessment methods are used to predict the failure in weldment [2]. The data obtained from high temperature crack initiation and growth tests were analyzed and used for two most widely used defect assessment methods, the British Time Dependent Failure Assessment Diagram (TDFAD) of R5 and German Two-Criteria-Diagram (2CD) methods. The assessment methods developed originally for base metals, never the less can predict reasonably the failure in

weldments of the studied material. The fracture mechanics parameter C^* was used to correlate the CCG rates in the P91 weldment CT specimens. The load line displacement rates and the CCG data, for the CT specimens, were used to calculate C^* values according to ASTM E 1457-15 [3]. Further, FE analyses were carried out to obtain the values of C^* , based on the steady-state value of the contour integral $C(t)$. Stationary crack CT models were used to obtain the C^* values. Damage mechanics theory and equations were used to predict the creep and CCG for the P91 weldment using the FE code, ABAQUS. Both the Kachanov-Rabotnov and Liu-Murakami damage models were used. In order to use these models, material properties have to be determined. The results of creep and creep rupture tests were used to determine those properties. It was found that both damage models could be used to predict the creep behavior of the tested materials. However, the Liu and Murakami model was favored over the Kachanov model in predicting the CCG in the CT specimens.

The results of experimental observations generally show significant differences in the creep properties in weldment zones with different microstructure. Thus, HAZ has higher creep strain rate and less time to rupture comparing to the same characteristics of the base material and weld metal. In general, results of finite element creep modeling predicted the critical damage accumulation and further rupture with crack initiation in the fine-grained and inter-critical HAZ [4]. Such a type of fracture agrees with the experiments, and the weldment crack location is of type IV due to the classification of damage types in weldments. However, failures due cracks within the weld metal have been encountered in practice, these cracks have types I and II in the classification scheme for damage types in weldments as presented in Figure 1-2.

Keywords: Creep crack growth, P91 weldments, finite element damage analysis

Scientific field: Mechanical Engineering

Narrow scientific field: Fracture Mechanics

UDC number:

621.791.05 : 669.15'24 : 539.434(043.3)

620.178.38 : 621.311 : 624.04(043.3)

РАСТ ПРСЛИНЕ УСЛЕД ПУЗАЊА У ЗАВАРЕНИМ СПОЈЕВИМА ОД ЧЕЛИКА

Rezime:

Zavarivanje predstavlja jednu od najrasprostranjenijih metoda spajanja nosećih elemenata u elektranama. Pri zavarivanju dolazi do značajnih promena u mehaničkim osobinama osnovnog materijala, u ovom slučaju čelika P91. Cilj ovog istraživanja je predviđanje toka puzanja i ponašanja zavarenih komponenti od čelika P91 pri oštećenju. Istraživanje je obuhvatilo analizu zavarenih konstrukcija izloženih puzanju na visokim temperaturama, kao i analizu mehaničkih osobina, napona i parametara otkaza i procene radnog veka [1]. Čelik sa povišenim sadržajem hroma, P91 (91Cr1Mo-NbV) je veoma pogodan za proizvodne pogone u kojima se radi na povišenim temperaturama. U slučaju rada pod uslovima puzanja, tj. Pri visokim temperaturama i/ili naponima, zavareni spojevima predstavljaju lokacije potencijalnog otkaza, i time ograničavaju radni vek celokupne elektrane. U ovoj tezi su prikazani rezultati ispitivanja puzanja i rasta prsline usled puzanja (Creep crack growth – CCG), koja su izvršena na zavarnim spojevima od čelika P91. Ova ispitivanja su izvršena za sve oblasti zavarnog spoja, odnosno osnovni materijal (OM), metal šava (MŠ) i zonu uticaja toplote (ZUT), pri temperaturi od 600°C. Za potrebe ispitivanja zavarnog spoja kao celine, posebna pažnja je posvećena oblasti prsline Tipa IV, koja predstavlja usku zonu na kraju ZUT-a, sa strane osnovnog materijala. U ovom istraživanju su takođe prikazani rezultati analize metodom konačnih elemenata, koji predviđaju puzanje i rast prsline usled puzanja u zavarnom spoju od čelika P91.

Zavarni spoj od čelika P91 je uzet u razmatranje za potrebe ovog ispitivanja rasta prsline usled puzanja pri radnoj temperaturi od 600°C, pri čemu je puzanje eksperimentalno izazvano na CT epruvetama, u četiri različite zone u zavarnom spoju. Mehaničke osobine i podaci dobijeni iz brojnih ispitivanja puzanja pri zatezanju, kao i ispitivanja inicijacije i rasta prsline usled puzanja su analizirani u skladu sa standardima, primenom metoda procene otkaza zavarenih spojeva [2]. Podaci dobijeni iz ispitivanja inicijacije i rasta prsline prvi visokom temperaturama su analizirani i upotrebljeni za dve najčešće

primenjivane metode ocene grešaka (Britanska TDFAD od R5 i nemačka 2CD metoda), koje su izvorno razvijene za osnovni material, ali bez obzira na to su se pokazale pouzdanim pri proceni otkaza zavarenih spojeva od predmetnog čelika.

Parametar mehanike loma C^* je primenjen kako bi se uspostavila veza između brzina rasta prsline usled puzanja u epruvetama za zatezanje od čelika P91. Vrednosti C^* su proračunate, u skladu sa standardom ASTM E 1457-15 [3], na osnovu podataka dobijenih iz dijagrama pomeranje napadne tačke sile – vreme (LLD –t) i dužina prsline – vreme (a –t) sila- pomeranje i ispitivanja rasta prsline usled puzanja. Sledeći korak se sastojao u određivanju C^* parametra primenom metode konačnih elemenata, na osnovu vrednosti konturnog integral $C(t)$. Ove vrednosti su određene na osnovu CT modela stacionarne prsline.

Teorija i jednačine mehanike oštećenja su korišćene u cilju predviđanja puzanja i rasta prsline usled puzanja zavarenih spojeva od P91, primenom softvera za MKE, ABAQUS-a. Primenjeni su Kachanov-Rabotnov i Liu-Murakami modeli oštećenja. Rezultati ispitivanja puzanja i loma usled puzanja su upotrebljeni za određivanje ovih parametara. Pokazalo se da oba modela mogu da pouzdano predvideti ponašanje ispitivanih materijala pri puzanju. Međutim, model Liu-Murakami se pokazao boljim u proceni rasta prsline usled puzanja CT epruveta.

Rezultati eksperimentalnih istraživanja su uglavnom pokazali značajne razlike u ponašanju pri puzanju u zonama zavarenog spoja sa različitim mikrostrukturama. Stoga, ZUT ima veću brzinu rasta prsline i manje vremena do loma u poređenju sa odgovarajućim osobinama osnovnog materijala i metala šava. Sveukupno gledano, rezultati modeliranja puzanja konačnim elementima su predvideli akumulaciju puzanja i inicijaciju prsline u sitnozrnoj i međukritičnoj ZUT [4]. Takva vrsta loma bila je uskladu sa eksperimentom, i lokacijom prsline Tipa IV u zavarenom spoju, usled klasifikacije tipa oštećenja. Međutim, u praksi su primećeni otkazi usled prsline u metalu šava (Tip I i II), u klasifikacionoj semi vrsta oštećenja u zavarenim spojevima, kao što je prikazano na slici 1.2.

LIST OF PUBLICATIONS:

Journal articles:

1. A. Sedmak, **M. Swei**, B. Petrovski: "Creep crack growth properties of P91 and P22 welded joints", FATIGUE & FRACTURE OF ENGINEERING MATERIALS & STRUCTURES, 2017, 40(8):1267-1275
2. **M. Swei**, A. Sedmak, B. Petrovski, Z. Golubovic, K. I. Azzabi. "Creep crack growth behavior of P91 steel weldments" Thermal Science, (2017), <https://doi.org/10.2298/TSCII170729240S>
3. **M. Swei**, A. Sedmak, B. Petrovski, Lj. Milović, A. Grbović. "Application of modified Finite Element Method to Creep crack growth simulation", accepted for Structural Integrity and Life, Vol.18, No. 2, (2018)

Conferences proceedings:

1. Aleksandar Sedmak, Blagoj Petrovski, **Mohamed Swei**, "ANALYSIS OF CREEP CRACK INITIATION AND GROWTH DATA OF P91 WELDMENTS AT 600 °C", NT2F16 – Dubrovnik, Croatia, 26.5.2016

NOMENCLATURE

\dot{V}_c	Creep component of load line displacement rate for compact tension specimens in creep crack growth tests
\dot{V}_p	Plastic component of load line displacement rate
\dot{V}_t	Total load line displacement rate in creep crack growth tests
$\dot{\epsilon}_{ave}$	Average creep strain rate
$\dot{\epsilon}_{eq}$	Equivalent creep strain rate
$\dot{\epsilon}_{ij}$	Creep strain rate tensor
$\dot{\epsilon}_{min}$	Minimum creep strain rate
S_{ij}	Deviatoric stress tensor
\dot{V}	Load line displacement rate in creep crack growth tests
\dot{a}	Creep crack growth rate
ϵ_p	Plastic strain
σ_{eq}	Equivalent, von Mises, stress
$\Delta\epsilon^c$	Creep strain increment
A	Material constant in Norton's creep law, Kachanov creep damage model, and Liu and Murakami creep damage model
a	Crack length
A'	Material constant in Norton creep model for average strain rate
B	Material constant in Kachanov creep damage model or full thickness of compact tension specimens
B _N	Net thickness of compact tension specimens
C	Material constant in Monkman-Grant relationship
C(t)	Contour integral characterizing stresses and strains at the crack tip in creeping cracked bodies
C*	Fracture mechanics parameter used to correlate creep crack growth rates creeping cracked bodies
D	Material constants in the relationship

D_1	Material constant in Ramberg-Osgood relationship
D_i	Inner diameter
D_o	Outer diameter
E	Modulus of elasticity
J	J contour integral
K	Stress intensity factor
M	Material constant in both Kachanov, and Liu and Murakami creep damage models; $M = B(1 + \phi)$
n	Material constant in Norton's creep law, Kachanov creep damage model, and Liu and Murakami creep damage model
n'	Material constant in Norton creep model for average strain rate
P	Applied load to compact tension specimens
P_L	Limiting load
q	Material constant in the relationship $\dot{a} = D(C^*)^q$
Q	Mismatch factor of heterogamous compact tension specimens
q_2	Material constant in Liu and Murakami creep damage model
t	Time
t_f	Failure time
t_T	Transient time
W	Width of compact tension specimen
X, Y, Z	Cartesian coordinates
α	Multiaxial parameter; material constant
β	Material constant in Monkman-Grant relationship
Δt	Time increment
ν	Poisson's ratio
σ	Stress
σ_1	Maximum principal stress
σ_h	Hydrostatic stress
σ_{non}	Nominal stress

σ_r	Rupture stress
σ_{ref}	Reference stress
σ_{ut}	Ultimate tensile stress
σ_y	Yield stress
χ	Material constant in both Kachanov, and Liu and Murakami creep damage models
ω	Damage parameter, ranging from 0 (no damage) to 1 (full damage)
c	Creep strain
f	Strain at failure
ϕ	Material constant in Kachanov creep damage model

ABBREVIATIONS

2D	Two dimensional
3D	Three dimensional
ASTM	American Society for Testing and Materials
Ave. SR	Average strain rate
CCG	Creep crack growth
CCRB	Circumferential cracked round bar
COD	Crack opening displacement
CT	Compact tension
DC	Direct current
DENT	Double edged notched in tension specimens
EBW	Electron Beam Welding
EDM	Electric discharge machining
FE	Finite element
GTAW	Gas Tungsten Arc Welding
HAZ	Heat affected zone
ID	Inner diameter
LLD	Load line displacement

MMA	Manual metal arc
Mo	Molybdenum
Mod.	Modified
mpc	Multipoint constraint
MSR	Minimum strain rate
OD	Outer diameter
PD	Potential difference
PM	Parent material
RSM	The Reference Stress Method
SEM	Scanning Electron Microscopy
W	Tungsten
WM	Weld metal

TABLE OF CONTENTS

ACKNOWLEDGEMENT..... IV

ABSTRACT..... V

LIST OF PUBLICATIONS..... IX

NOMENCLATURE..... X

TABLE OF CONTENTS..... XIV

LIST OF FIGURES..... XVIII

LIST OF TABLES..... XXI

1 INTRODUCTION 1

 1.1 Steel Weldments 2

 1.2 Cracks in Welded Joints..... 3

 1.2.1 Type IV Cracks 4

 1.3 The Hardness Variations in Weldment..... 5

 1.4 Flaw Assessment of Weldment 6

 1.5 Creep Crack Growth 7

 1.6 Objectives and Scope of Work 9

 1.7 Arrangement of Thesis 10

2 LITERATURE REVIEW 12

 2.1 Fracture Mechanics Theories 13

 2.1.1 Linear Elastic Fracture Mechanics 13

 2.1.1.1 Stress Function Methods..... 14

 2.1.1.2 Energy Methods 16

 2.1.2 Small-Scale Yielding..... 18

 2.1.3 Elastic-Plastic Fracture Mechanics 20

 2.1.4 Crack Opening Displacement Criterion 20

 2.1.5 The J Contour Integral 22

 2.1.5.1 HRR Fields..... 24

 2.1.5.2 J-Integral Estimation Methods 25

 2.1.5.3 Estimation of J for CT specimen by EPRI 28

2.1.5.4	Estimation of J in Terms of Strain at Reference Stress Approach	29
2.2	Definition of Creep	29
2.2.1	Creep Mechanisms	30
2.2.2	Creep Curves	31
2.2.3	Power-Law Representation of Creep	33
2.2.4	Creep Constitutive Modelling.....	35
2.2.4.1	Constitutive Equation Selection	36
2.2.4.2	Predicting Service Life	36
2.2.5	Secondary and Average Creep Strain Rates	37
2.2.6	Creep Strength	38
2.2.7	Creep Resistant Martensitic Steels.....	39
2.2.8	Mod - 9Cr1Mo Steel (P91).....	40
2.3	Deformation and Fracture at High Temperature	42
2.3.1	Deformations under Creep Conditions	43
2.3.2	Elastic-Plastic Deformation	43
2.3.3	Ramberg-Osgood Material Model.....	44
2.3.4	Multi-axial Deformation	46
2.3.5	Limit Load and Reference Stress Concepts	46
2.4	Time-Dependent Fracture Mechanics.....	47
2.4.1	Creep Crack Growth	47
2.4.2	Crack-Tip Parameters	50
2.4.3	The C* Parameter.....	51
2.4.4	Creep Crack Growth Models	54
2.4.4.1	NSW Model	54
2.4.4.2	Modified NSW Model.....	56
2.4.5	Creep Crack Initiation.....	57
3	DAMAGE MECHANICS APPROACH OF WELDMENTS MODELING AT ALL CREEP STAGES ...	59
3.1	Introduction	59
3.2	Continuum Damage Mechanics	60
3.3	Creep Constitutive Models.....	61
3.3.1	The Kachanov and Rabotnov Model	62

3.3.2	The Liu and Murakami Model	64
3.3.3	The Cocks and Ashby Model	65
3.3.4	The Wen and Tu Model	66
3.4	The Effects of Stress Level and Stress State on the Creep Ductility	67
3.5	Estimations of Material Constants for Damage Models	69
3.6	Implementation of Finite Element Method to Creep-Damage Research	71
4	EXPERIMENTAL INVESTIGATIONS OF CREEP BEHAVIOUR IN P91 WELDMENTS.....	74
4.1	P91 Steel Weldment and Specimens	74
4.1.1	Similar Weldments	76
4.1.2	Mechanical and Creep properties	77
4.1.2.1	P91 Weldments Uniaxial Creep Tests	80
4.1.2.2	Creep Test Data for Different Temperatures	81
4.1.3	CT Specimens	83
4.2	Creep Crack Growth Behavior of P91 Weldments	85
4.2.1	The DCPD method of Crack Length Measuring	88
4.2.1.1	Test Procedures.....	91
4.2.1.2	Load Line Displacement	92
4.2.1.3	Crack Length.....	94
4.2.2	Validity of Test Results	95
4.3	Creep Crack Initiation in P91 Weldment.....	99
4.3.1	Initial Creep Crack Growth Rates	99
4.3.2	Creep Crack Initiation Time Predictions.....	100
4.3.3	The Behavior of Creep Crack Initiation	103
4.4	Experimental Determination of C^* Integral	106
4.4.1	Time Dependent Failure Assessment Diagram (TDFAD) Approach	111
4.4.2	Application of Two Criteria Diagram (2CD)	114
5	MODELLING OF CREEP CRACK GROWTH AND DAMAGE BEHAVIOUR OF P91 STEEL WELDMENT	116
5.1	Finite Element Model.....	116
5.1.1	The Load Line Displacement (LLD) FE Prediction	119
5.1.2	The Fracture Parameter (C^*) FE Prediction.....	121

5.1.3	FE Modelling of CT Specimen Growing Crack	125
5.1.4	FE Evaluations of C* by Secondary and Average Creep Strain Rates	129
5.2	Creep and Damage Models of P91 Steel Weldments	130
5.2.1	Determination of Material Constants for Creep Damage Models	132
5.2.1.1	Determination of Norton Model Material Constants (A and n)	132
5.2.1.2	Determination of Material Constants for Damage Models (M, χ , B, φ , α and q_2)	133
5.3	CCG Predictions by Damage Models	135
6	CONCLUSIONS AND RECOMMENDATIONS	140
7	References	143

LIST OF FIGURES:

Figure 1-1 Schematic of the sub-zones of the HAZ [8]. 3

Figure 1-2 Types of cracking in weld joint of steel [10]..... 4

Figure 1-3 Type IV crack in P91 Steel [11] 5

Figure 1-4 Representative micro-hardness across a typical P91 weldment [12]..... 6

Figure 1-5 Creep crack growth of welded joint [18]..... 8

Figure 2-1 Coordinate system describing a crack in an arbitrary body [16]. 14

Figure 2-2 Crack extension in an arbitrary cracked body [16]..... 16

Figure 2-3 Elastic load displacement response for crack sizes differing by d_a [16]..... 17

Figure 2-4 Schematic stress field ahead of a crack in small-scale yielding 19

Figure 2-5 Crack-tip blunting and crack opening displacement δ 21

Figure 2-6 Stress-strain behavior of an elastic-plastic material 22

Figure 2-7 Integration contour around a crack tip..... 24

Figure 2-8 Load-displacement response and definition of (a) plastic displacement Δ_p and plastic area A_p (b) plastic secant area A_{sec} , under the load-plastic curve [31] 26

Figure 2-9 Creep mechanisms (a) Vacancy diffusion (b) Interstitial diffusion..... 31

Figure 2-10 Definitions of creep strain rates representation in creep curve [36]. 32

Figure 2-11 Representation of rupture times versus applied stress [36]. 33

Figure 2-12 Variation of creep rate with stress [35]. 34

Figure 2-13 Schematic creep curve illustrating secondary and average creep rates [38]..... 37

Figure 2-14 Comparison of nominal pipe thickness for different steels [10]..... 41

Figure 2-15 Microstructure of Mod. P91 BM [41]. 42

Figure 2-16 Typical stress-strain in Ramberg-Osgood material model 45

Figure 2-17 Creep response zones at a crack tip [25] 49

Figure 2-18 Schematic representation of levels of creep deformation [46] 51

Figure 2-19 Definition of crack tip coordinates and creep process zone size, r_c [50] 55

Figure 2-20 Dependence of (a) $\sigma \epsilon \dot{\epsilon}$ and (b) $\epsilon \dot{\epsilon} * \theta$ on angle θ and n [53]..... 57

Figure 2-21 Development of crack blunting and crack initiation [51]. 58

Figure 3-1 Creep deformation and damage evolution parameter [55]. 59

Figure 3-2 schematic illustration of a typical creep behavior [58]..... 61

Figure 3-3 Morphology of crack growth with creep voids and microcracks in the area near the macroscopic crack in a C(T) specimen [67]..... 67

Figure 3-4 Variation of creep ductility (in terms of reduction in area) against normalized stress 68

Figure 3-5 Effect of stress triaxiality on creep ductility for bar specimens at elevated temperature..... 69

Figure 3-6 Creep analysis procedures in a commercial FEM Abaqus code with conventional creep laws and with user-defined creep-damage models [56]..... 73

Figure 4-1 Schematic of CT specimens (a) starter crack position of HAZ 75

Figure 4-2 P91 Pipe circumferential weldment [80]. 77

Figure 4-3 Uniaxial creep test specimen 78

Figure 4-4 Stress-strain curves of P91 weldment tensile specimens at 600 °C.....	79
Figure 4-5 Stress and temperature dependence of creep rupture life [81].	80
Figure 4-6 Creep test data for P91 weldment at 600 °C.....	81
Figure 4-7 Creep strain vs. time of P91 parent material for different temperatures.....	82
Figure 4-8 Time-temperature regions at specified reference stress [82]	82
Figure 4-9 Specifications and dimensions of CT specimens(a) Base metal specimen and side groove (b) Cross weld specimen consist of BM, WM and HAZ	84
Figure 4-10 Compact tension specimens extracting from P91 steel welded joint. WM, BM and HAZ [5]......	85
Figure 4-11 Steady state Creep rates as a function of stress for P91 weldment at 600 °C.....	86
Figure 4-12 Comparison of creep rate of weldments versus stress	88
Figure 4-13 DCPD system including a CT specimen	89
Figure 4-14 High temperature experimental set-up	92
Figure 4-15 Load Line Displacement of P91 weldment at 600 °C	93
Figure 4-16 Crack extension comparison of P91 weldment at 600 °C [87].....	95
Figure 4-17 Crack growth rate versus crack extension of P91 weldment [5]	98
Figure 4-18 Creep crack growth in a welded joint [5]	99
Figure 4-19 Creep crack initiation resistance of P91 weldment with NSW bounds at $\Delta a = 0.2$ mm	101
Figure 4-20 Creep crack initiation resistance of P91 weldment with NSW bounds at $\Delta a = 0.5$ mm	102
Figure 4-21 Comparison of CCI resistance behavior in terms of K of P91 steel weldment [91]	104
Figure 4-22 Comparison of CCI resistance behavior in terms of C^* of P91 steel weldment [91]	104
Figure 4-23 Crack initiation resistance of P91 weldment zones at 600 °C in terms of K and C^* correlated with the time to crack initiation at $\Delta a = 0.2$ mm [92].	105
Figure 4-24 Crack initiation resistance of P91 weldment zones at 600 °C in terms of K and C^* correlated with the time to crack initiation at $\Delta a = 0.5$ mm [92].	106
Figure 4-25 Correlation of creep crack growth rate with K for different weldment zones of P91 steel at 600 °C	110
Figure 4-26 Correlation of creep crack growth rate with C^* for different weldment zones of P91 steel at 600 °C	111
Figure 4-27 TDFAD of P91 weldment at 600 °C for crack growth $\Delta a = 0.2$ mm and 0.5mm .	113
Figure 4-28 2CD of P91 weldment at 600 °C for crack growth $\Delta a = 0.2$ mm and 0.5mm	115
Figure 5-1 CT Dimensions and arrangement of tested CT specimen	117
Figure 5-2 CT specimen FE modelling for CCG simulations.....	118
Figure 5-3 Finite element simulation results and comparison with the experimental CCG data	120
Figure 5-4 Finite element simulation results and comparison with the experimental CCG data	121
Figure 5-5 FE CT model using collapsed elements ahead of the crack tip	122

Figure 5-6 FE CT model using quadrilateral 8-node elements ahead of crack tip 123

Figure 5-7 FE $C(t)$ integral by quadrilateral 4-node and collapsed elements for P91 weldment
 124

Figure 5-8 Variations of time increment Δt and contour integral $C(t)$ for P91 weldment..... 125

Figure 5-9 Fine meshed crack segments ahead of crack tip..... 126

Figure 5-10 Released elements of the growing crack mode 127

Figure 5-11 FE C^* predictions for growing crack models vs. experimental data 127

Figure 5-12 Comparison of FE obtained C^* vs. CCG with experimental data [87] 128

Figure 5-13 FE C^* versus creep crack length for minimum and average creep strain rate..... 130

Figure 5-14 Schematic of node release modeling for creep crack growth [87] 131

Figure 5-15 Uniaxial creep strain versus time curves for P91 weldment at 600 °C 134

Figure 5-16 Damage contour plot for creep analysis using the node release model 136

Figure 5-17 Predicted crack growth for node-release and growing crack models 137

Figure 5-18 FE simulations of P91 (a) 3D model CT specimen (b) Crack tip detail [107] 138

Figure 5-19 FE simulation results of C^* and comparison with the experimental CCG data [107]
 139

LIST OF TABLES:

Table 2-1 Definition of H, H'and A for CT specimen geometry [32] 27

Table 2-2 Classical representations of primary, secondary and tertiary creep [8]. 35

Table 2-3 Chemical Compositions of 9% Cr and 12% Cr martensitic steels [39]. 40

Table 3-1 Material constants for damage models (σ in MPa and time in hour)..... 70

Table 4-1 Chemical Composition of P91 Weldment [80]..... 76

Table 4-2 Material Data Determined in Tensile and Creep Tests 78

Table 4-3 Steady-state creep rate as a function of stress of P91 weldments at 600 °C 87

Table 4-4 Details of the test conditions for the BM, WM and HAZ of P91steel at 600 °C 89

Table 4-5 The data attained from CT specimens of P91weldment tests 90

Table 4-6 Material constants collected from CCG tests of P91 weldments at 600 °C 109

Table 5-1 Details of CT specimens modelled and loading conditions 119

Table 5-2 FE models C* values and transient times for P91 weldment..... 124

Table 5-3 Material constants of minimum and average creep rates of P91 weldment at 600 °C
..... 129

Table 5-4 P91 weldment constants for damage models at 600 °C 135

1 INTRODUCTION

In order to improve energy efficiency and reduce CO₂ emissions and to prevent many of the failures in high temperature components in industrial power plants Efforts are made to increase the steam temperature of new power plants above 873 K. Substantial study effort since 1990's involved creep damage or cracking in welded joints. A common methodology is based on stress analysis of homogeneous material, without taking into account cracks, but in the case of welded joints, an analysis that is more complex is needed, including the effect of creep cracking. Steel weldment components used in power generation plants are continually exposed to high temperatures, failure processes such as creep crack growth (CCG), Safe, and accurate methods to predict creep crack growth (CCG) are therefore required in order to assess the reliability of such components. Evidence has shown that in many cases, creep damage in the form of cracks occur, in the heat affected zone (HAZ) region. For example, Type IV cracking generally occurs in the low temperature HAZ region, near to the parent material [5].

The operational and plant assessment experience indicates that in the majority of cases where a failure occurs in components, defects predominate near weldments. Therefore, time-dependent failure at high temperatures by creep crack initiation (CCI) and CCG in structural joints imposes a limit on component service life in plants. The most widely used standard for creep crack growth testing of metallic materials, by American Society for Testing and Materials ASTM E1457-15, is mainly addressing testing homogeneous materials in compact tension, C(T), type specimens [3]. Creep deformation of a steel in its creep range is inevitable circumstances after a period; therefore, a final structures failure due to creep crack growth may not be avoided but can be controlled. Flaw contained high-temperature components, which are subjected to creep loading, may fail by creep crack growth [1].

Martensitic heat resistance steel P91 is exceptional in resistance to oxidation, high-temperature strength and weldability, it has been widely used in fossil-fired power plants, boiler, pressure vessel, petroleum engineering, chemical plant and nuclear power station. P91 is mainly applied in the elevated temperature component in supercritical power plants, for instance, main stream, superheaters and reheaters [6]. Welds mainly fabricate most structures and components of industrial power plants; therefore, creep life assessment in welded joints is very important. The creep strength of weldments has been

established that of such high Cr steels decrease due to Type IV creep damage located in the fine-grained heat affected zone (HAZ). In addition, creep crack growth (CCG) can occur in components operated under elevated temperatures. Safe and accurate methods to predict creep crack growth (CCG) are required in order to assess the reliability of such components. Therefore, it is important to predict creep crack initiation and growth in the fine-grained HAZ region [7]. Experimental studies of cross-weld specimens performed to analyze the cause of type IV creep failure and obtain the criterion for the creep behavior. In general, weld boundary is approximately normal to the applied stress for uniaxial creep specimens.

1.1 Steel Weldments

Up until the end of the 19th century, a heating and hammering process called forge welding joined sections of metal together. Today, a variety of different welding processes are available, such that welding is extensively used as a fabrication process for joining materials in a wide range of compositions, part shapes and sizes. Welding is still the major joining technology for power plant components. The joint of components such as pipes and tubes can consist of similar metal welding (SMW) and dissimilar metal welding (DMW) [8]. The heat involved in the welding process intensely affects the microstructure and mechanical properties of creep resistant steels adjacent to the fusion line. The influenced region is known as heat-affected zone (HAZ). Several parameters govern the resulting microstructures and mechanical properties of the HAZ.

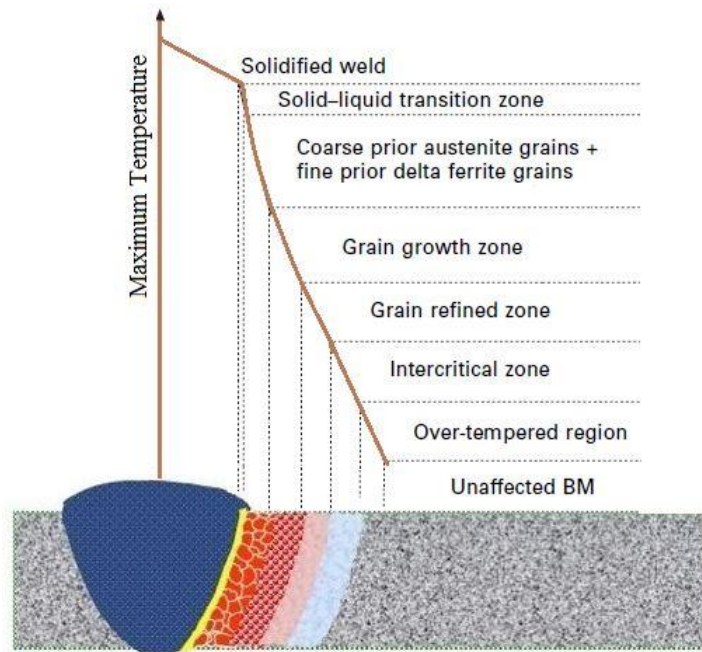


Figure 1-1 Schematic of the sub-zones of the HAZ [8].

The weldment is a combination of different material zones: parent metal, weld metal, and HAZ. Each zone may exhibit quite different material properties, which leads to great difficulties in understanding the creep behavior of a complete weldment. In order to obtain the necessary material data, some conventional tests were done separately on parent metal, weld metal and simulated HAZ. Further, the HAZ region may be divided into several different sub-regions, namely; coarse-grained zone (close to the fusion line), fine-grained zone (in the middle of HAZ) and inter-critical zone, usually referred to as the Type IV region (close to the PM/HAZ boundary) as presented in Figure 1-1. Highly complexity of the structure arises from the presence of the different materials that make the weld region [1].

1.2 Cracks in Welded Joints

Cracks in welded joints are categorized according to their locations. Type I and Type II cracks occur within weld metal, Type I is confined to weld metal whereas Type II may grow outside the weld metal and into the parent material. Type III cracks occur in coarse-grained HAZ. Type IV cracks initiate and grow in a narrow zone of HAZ material,

adjacent to the BM/HAZ boundary. Type IV cracking is the most severe form of cracks because it results in the highest rate of void formation, leading to early failure when compared with creep tests on the base metal homogenous specimens [9]

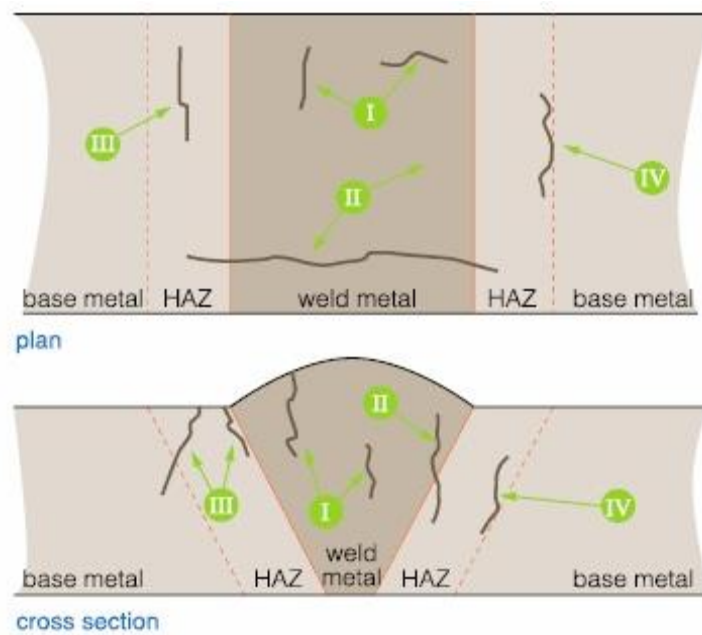


Figure 1-2 Types of cracking in weld joint of steel [10]

1.2.1 Type IV Cracks

Type-IV cracks appear in the inter-critical region of the HAZ in welded components, which operate under creep conditions. Type IV cracking can occur after as little as 40,000 hours in service and up to 200,000 hours or more. The phenomenon occurs because of an inherently weak zone at the edge of the visible HAZ. This low creep strength region is attributed to the partial transformation of ferrite to austenite during the welding thermal cycle and/or the over-tempering or softening of the material in this region. The cracking initiates from localized formation and growth of creep voids in the 'Type IV zone'. A significant feature of the subsequent cracking is that it can be relatively rapid. Tests performed and measured the creep crack growth in a P91 welded pipe, internal gas pressure, at 625°C was applied, and the initial cracks were located in the middle of the

HAZ region. It was found that the initial cracks deviated until they reached the Type IV region, and then they remained in that region, shown in Figure 1-3 [11].

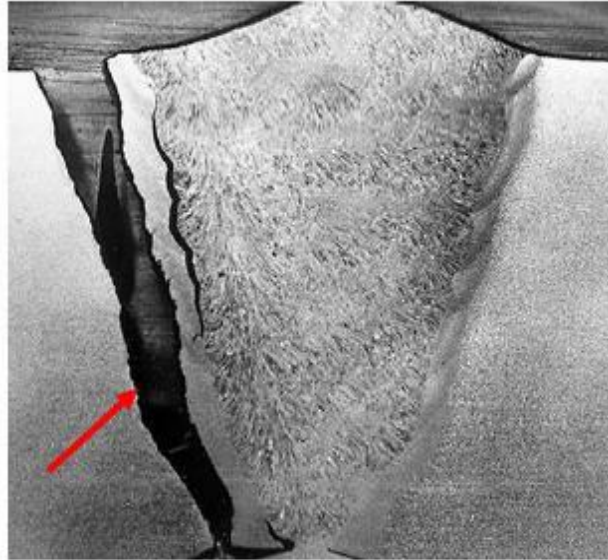


Figure 1-3 Type IV crack in P91 Steel [11]

1.3 The Hardness Variations in Weldment

The hardness results across the weldment are shown in Figure 1-4 the position of the fusion line is highlighted by the dotted line in the figure. As expected the change in grain size as a result of heating during welding leads to a change in the hardness of the heat affected zone. The change in the properties of the base metal start approximately 4 mm from the weld center, after this point, the hardness drops corresponding to the increase in the grain size for the large grained region of the HAZ closer to the fusion line, the hardness increases as the HAZ becomes finer grained and the hardness increases. The region of higher hardness on the left hand side of the figure corresponds to the weld material which, as previously mentioned is overmatched to the parent material. This change in hardness with microstructure is consistent with those previously reported in the literature for P91 steel heat affected zones [12].

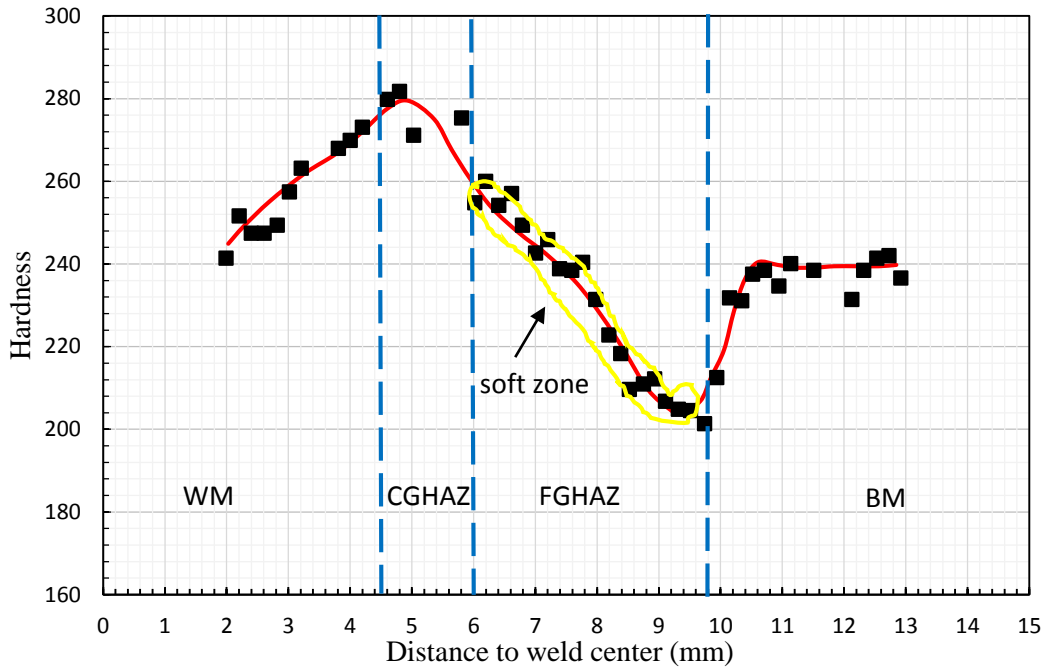


Figure 1-4 Representative micro-hardness across a typical P91 weldment [12]

1.4 Flaw Assessment of Weldment

Restriction of the high temperature component performance by the performance of the welds under service conditions. The broad engineering assessment approach requires three elements need to be addressed separately, these are processing, properties, and structural integrity that cover the design of the structure, material, and process selection to safety and reliability of the plant. Weldments are functionally graded materials with complex microstructure due to local effects of heat from the welding process. Additionally, the components of the weldment vary containing a range of interfaces possessing different local properties as in similar and dissimilar welds with or without filler metal [13]. Producers of High temperature fracture mechanics can be developed, through which the time-dependent effects of creep could be modeled, uses experimental uniaxial and crack growth data from simple laboratory test specimens in order to predict failure times under operating conditions. Furthermore, the improvement in non-destructive inspections and testing methods (NDT) has allowed smaller defects to be detected and the need for more reliable methods for prediction of crack

initiation/incubation periods and steady crack growth rates. The input into a code of practice for defect assessment should include a number of important variables that the designer must obtain. It is vital to obtain information such as plant history, loading conditions under normal and abnormal operating conditions, characterization of defects stress analysis of the cracked structure and the relevant material properties data. Under high temperature, operating conditions creep or fatigue could be the primary mechanism for initiating and growing a crack in components, crack propagation can continue until structural failure takes place [14].

1.5 Creep Crack Growth

Creep crack growth is the time-dependent extension of a macroscopic crack at elevated temperatures under more or less constant load. A macroscopic crack, as distinct from grain boundary cavities, is a crack, which is larger than the structural lengths of the material, which are relevant for crack growth (for example, the grain size). Failure by crack growth may predominate over homogeneous grain boundary cavitation in the whole cross section, if a crack initiated at a pre-existing defect or a sharp notch early in the lifetime of the component. If creep crack growth is a potential failure mode, design codes and inspection standards should provide a means to assess the relevance of cracks in high-temperature components. Such an assessment should include crack-like defects, which were detected by non-destructive evaluation, and, in critical applications, one must assume that cracks of a certain maximum size, which might have escaped detection, are present. A lifetime prediction should then be based on the expected growth rates of such defects in future service. In the analysis of creep crack growth it is convenient to distinguish two aspects [15]:

1. The continuum-mechanical deformation fields in the cracked body.
2. The micromechanisms of crack growth, which operate near the crack tip.

Methods for determining the creep crack growth properties of materials are broadly similar to those used to determine the uniaxial creep data. A cracked specimen is subjected to a constant load at elevated temperature and crack extension measured as a function of time [16]. The types of the specimen that are used most often are compact

tension (CT), single edge notch tension (SENT), single edge notch bend (SENB), center cracked plate (CCP) and double cantilever bend (DCB) test specimens. When these specimens are subjected to a constant load the magnitude of the stresses generated at the crack tip increases with crack extension.

Knowing that the creep strength of weldments of such high Cr steels decreases due to Type IV creep damage located in the fine-grained heat affected zone (HAZ). In addition, creep crack growth (CCG) can occur in components operated at elevated temperatures. Safe and accurate methods to predict creep crack growth (CCG) are required in order to assess the reliability of such components. Therefore, it is important to predict creep crack initiation and growth in the fine-grained HAZ region. Representation of CCG path of welded joint CT specimens indicated in Figure 1-5. With advances in finite element (FE) methods, compound models can be applied in the study of CCG where simple analytical solutions or approximate methods are no longer applicable, also the role of fracture mechanics parameters in estimating creep crack growth rates is examined using FE analysis, and the results are validated with experimental data [17].

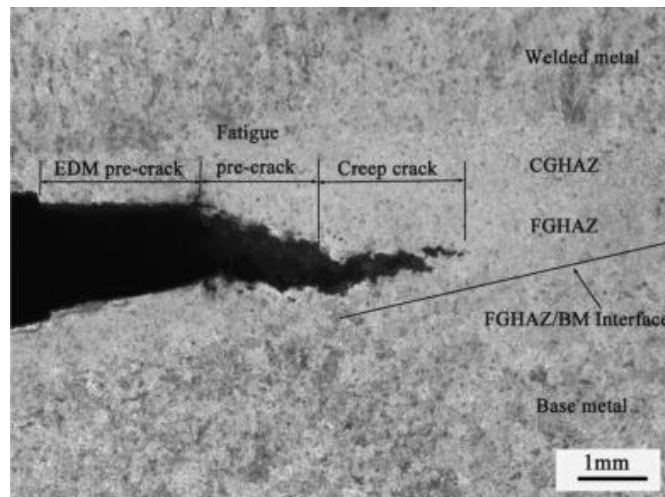


Figure 1-5 Creep crack growth of welded joint [18].

1.6 Objectives and Scope of Work

The objective of this thesis is to study and predict creep behavior and creep crack growth in P91 high temperature steel, which is used in the manufacturing of main steam pipes in power plants, chemical plants, and nuclear plants. The improved thermal efficiency of the power plant has been the main driver for the development of ferritic-martensitic 9-12%Cr creep-resistant steels that are also commonly known as creep strength enhanced ferritic steels. The target operating temperature for these steels is 650°C, with a common target design life of 100,000 h. The factors that govern the life of materials in high-temperature components include creep, fatigue, and corrosion, which, creep is a fundamental damage among them. The study of creep initiation and creep crack propagation in weldments materials helps in early predictions of structure and pipe components failure. Reliable and precise prediction remaining life provide maintenance of plant components and scheduling of safe replacement or repair in order to maximize plant efficiency [19].

The primary aim of this study is to investigate and simulate the effects of creep process, creep crack initiation, and growth for P91 steel components, employing both experimental methods and finite element modeling techniques. The main objectives are:

1. Study and predict creep and creep crack growth (CCG) in P91 high temperature steel at 600 °C.
2. To determine the elastic/plastic fracture mechanics parameter J-integral and its analogous creep fracture parameter C^* properties on a range of welded fracture mechanics specimens.
3. To perform high-temperature experimental testing to measure tensile, creep deformation, crack growth behaviors of the service-exposed base, and weld materials that can be employed in the creep process model.
4. To examine appropriate FE models to predict creep process properties, creep crack initiation (CCI) and creep crack growth (CCG) of welded components.
5. Understand and evaluate the creep deformation and damage models combine with constitutive equations for high chromium alloy steel P91.

1.7 Arrangement of Thesis

Succeeding this introduction, the literature review in Chapter 2 is divided into three parts. The first covers, in some detail the fracture mechanics theories and the elastic-plastic fracture mechanics also evaluations of fracture parameters. The second part reviews the general background to creep, high temperature materials and creep in welds, including Type IV cracks with the creep constitutive modeling. The third part reviews the time-dependent fracture mechanics and prediction of CCG using a damage mechanics approach. The effects and determination of material properties are also included with creep crack growth models.

Chapter 3 covers details of the damage mechanics approach of weldments modeling and creep constitutive models, reviewing the creep damage equations of four well Known models also presenting the effects of stress levels on the creep ductility of the P91 material. Lastly, the implementation of finite element method using the determined material constants for damage models to predict the creep crack growth analytically to validate the experimental data.

Chapter 4 presents in detail the experimental procedures of creep flow and creep crack initiations and growth testing of P91 weldment material, analysis of results data reached. Uniaxial and notched bar specimens were tested to obtain the materials creep and creep rupture data for parent material (BM) and weld metal (WM). Creep data for HAZ material also obtained using tensile testing and cross-weld uniaxial. Compact tension (CT) specimens were utilized to study creep crack growth in P91 weldments. Creep and creep crack growth tests were conducted at 600°C for the P91 material. Load line displacements were recorded from testing the CT specimens and crack length monitored using the potential difference (PD) method. The load line displacement rates and the corresponding crack lengths were then used to calculate C^* , a fracture mechanics parameter used to correlate creep crack growth rates of cracks in cracked specimens of CT specimens.

Chapter 5 outlines the modeling of creep damage behavior of P91 steel weldment with the use of modern mathematical constitutive models to predict material deformation and failure in engineering structures. The constitutive models are based on the notion of a

damage state variable (ω), which introduced in chapter 3, through the different creep damage models. Finite element analyses were conducted on a two dimensional (2D) FE model of a compact tension CT specimen and three material cases have been considered using material properties of BM, WM and HAZ for P91 steel at 600 °C. The FEM has been widely used to calculate C^* using CT specimens. Firstly, it was used to obtain FE steady state load line displacement rates, for CT specimens, which were then used to calculate C^* , and analyzed for P91 BM, WM and HAZ CT specimens with different loading conditions and same initial crack lengths.

Finally, Chapter 6 presents a general discussion, main conclusions, and the recommendations.

2 LITERATURE REVIEW

Power generation and petrochemical plants endure failures of high temperature components, based on the operational and plant assessment experience indicate that in the majority of cases where a failure occurs in components, defects predominate near weldments. Therefore, time dependent failure at high temperatures by creep crack initiation (CCI) and creep crack growth (CCG) in weldment joints imposes a limit on component service life in plants. Although the concepts used for time-dependent fracture analysis of homogeneous bodies applied for defect assessment of weldments, complex structure of weldments having various weldment zones, which exhibit particular interactions, requires a unique approach in testing and failure assessment.

The evaluation of mechanical properties of welded joints has received considerable attention in the past because weldments are often nucleation sites for catastrophic failures. The process of welding, during either primary fabrication or field repair, results in the development of metallurgical joints with heterogeneous microstructures and properties. The term "heterogeneous" indicates that the microstructures vary with the position; this is in direct distinction to formed base metals, which presumed to possess essentially homogeneous microstructures and mechanical properties [20].

The creep damage issue has been disputed for a long time. Creep damage has caused the attention of many researchers and industries. The European Creep Collaborative Committee (ECCC) is one of the organizations to collect information and data from 16 countries involving over 40 European organizations. ECCC provides a platform for co-operation of European industry and research to exchange and update of information and data for materials in the creep regime from different projects. ECCC also frequently produces guidelines for the generation, treatments, and assessment of large creep datasets for industry [21]. Creep Group of European Thematic Network (FITNET) indicate the need for novel methods in defect assessment of weldments and harmonies the existing knowledge in the industry and academic research for a combined defect assessment method for weldments [22].

2.1 Fracture Mechanics Theories

Fracture mechanics provides the basis for designing machine and structural components with materials containing defects such as crack, gives rational approach for assessing degree of safety or reliability of an in-service degraded machine component, and helps to calculate the life of a component with crack subjected to cyclically fluctuating load, corrosion, creep, or a combination of all these. A crack is a discontinuity, internal or external, in the material with zero tip radius. The development of the subject has been motivated by the severe safety requirements of the aerospace industry, nuclear power plants, and other safety-critical applications. The advancement in the understanding of the topic coupled with developments in material science, experimental methods, and numerical techniques such as finite element, boundary element, and meshless methods, has facilitated optimum design and minimization of material usage for an application.

2.1.1 Linear Elastic Fracture Mechanics

Linear Elastic Fracture Mechanics (LEFM) is the basic theory of fracture, originally developed by Griffith (1921 to 1924) and completed in its essential form by Irwin (1957, 1958) and Rice (1968). LEFM is a highly simplified, yet sophisticated, theory that deals with sharp cracks in elastic bodies. The stress near the crack tip is so high that some kind of inelasticity must take place in the immediate vicinity of the crack tip. However, if the size of the inelastic zone is small relative to the linear dimensions of the body (including the size of the crack itself), then the disturbance introduced by this small inelastic region is also small. Therefore, LEFM and point of failure can be verified exactly.

A crack in a two-dimensional body is considered as shown in Figure 2-1. Conditions of either plane stress or plane strain are assumed to apply and the crack length is $2a$ for an embedded defect. An important concept in fracture mechanics is that local to the crack tip the stress and strain fields vary with the coordinates in a manner which depends only on material properties apart from a single scaling parameter. The local variations with position are determined by solution of the equilibrium and compatibility equations in

conjunction with the boundary conditions on the crack surface. The effects of remote loading, geometry and crack size are all included in the single scaling parameter, which is termed the stress intensity factor, K .

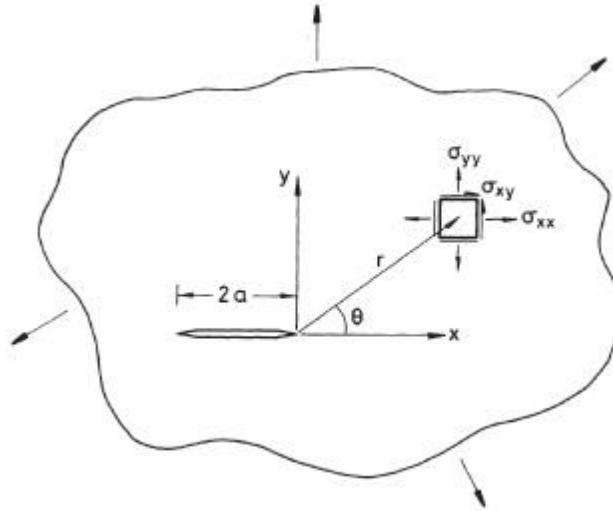


Figure 2-1 Coordinate system describing a crack in an arbitrary body [16].

2.1.1.1 Stress Function Methods

For elastic material behavior, the stresses close to the crack tip are given in terms of the coordinates of Figure 2-1 as

$$\begin{aligned}\sigma_{xx} &= \frac{K}{\sqrt{2\pi r}} \cos \frac{\theta}{2} \left(1 - \sin \frac{\theta}{2} \sin \frac{3\theta}{2} \right) + T \\ \sigma_{yy} &= \frac{K}{\sqrt{2\pi r}} \cos \frac{\theta}{2} \left(1 + \sin \frac{\theta}{2} \sin \frac{3\theta}{2} \right) \\ \sigma_{xy} &= \frac{K}{\sqrt{2\pi r}} \cos \frac{\theta}{2} \left(\sin \frac{\theta}{2} \cos \frac{3\theta}{2} \right)\end{aligned}\tag{2-1}$$

The form of these equations holds irrespective of the remote boundary conditions but these affect the parameter K that defines the amplitude of the crack tip singularity. The remote boundary conditions also affect the higher order terms but these are negligible except away from the crack tip region when r is not small compared with the crack size a or any other dimension such as remaining ligament. The second order term, the T stress, depends on geometry, crack size and the tractions parallel to the crack plane in the x -

direction and is sometimes used in two parameter descriptions of fracture. Here only the single parameter description involving K is considered. Then Equations (2-1), may be written in tensor notation as

$$\sigma_{ij} = Kr^{-1/2}f_{ij}(\theta) \quad (2-2)$$

As the body is linearly elastic, the strains local to the crack tip obey a similar equation, namely

$$\varepsilon_{ij}^e = \left(\frac{K}{E}\right)r^{-1/2}g_{ij}(\theta, \nu) \quad (2-3)$$

Where the functions g_{ij} depend on Poisson's ratio ν and on whether conditions of plane stress or plane strain apply. The functions g_{ij} can readily be derived from equation (2-1) by noting that the out-of-plane stress $\sigma_{zz} = 0$ in plane stress, and $\sigma_{zz} = \nu(\sigma_{xx} + \sigma_{yy})$ in plane strain.

As the body is linearly elastic, K must be directly proportional to applied load. K also depends on the geometry and crack size, a , and solutions are widely available in handbooks [23][24]. For an infinite plate loaded by a uniform tensile stress, σ , normal to a crack of size, $2a$

$$K = \sigma\sqrt{\pi a} \quad (2-4)$$

The solution for a crack in a finite body can be written

$$K = Y\sigma\sqrt{a} \quad (2-5)$$

Where Y is a non-dimensional function of crack size and component dimensions, stress intensity factor solutions for a number of common test specimen geometries are presented in reference [23].

An important consequence of Equations (2-2) and (2-3) is that the strain energy density varies as $(1/r)$ as the crack tip is approached. Using the summation convention for tensor notation involving repeated indices, the strain energy density is

$$\frac{1}{2}\sigma_{ij}\varepsilon_{ij}^e = \left(\frac{K^2}{E}\right)r^{-1}f(\theta, \nu) \quad (2-6)$$

Where the function $f(\theta, \nu)$ depends on whether conditions of plane stress or plane strain apply. By integrating equation (2-6) over a small circular region at the crack tip,

demonstrating that the energy stored within a finite region is finite, However, if the singularity was any stronger, the $r^{(-1/2)}$ singularity in stress and strain is the strongest singularity possible at the crack tip for an elastic material [16].

2.1.1.2 Energy Methods

An alternative characterization of the crack tip region for elastic materials is possible in terms of the energy release rate G , where G is the energy expended in extending a crack over unit area. A body of thickness B and arbitrary shape containing an edge crack of length a demonstrated in Figure 2-2. The line OA in Figure 2-3 represents its equivalent elastic load versus displacement diagram. At A the crack is allowed to extend by an amount da along the path AA' .

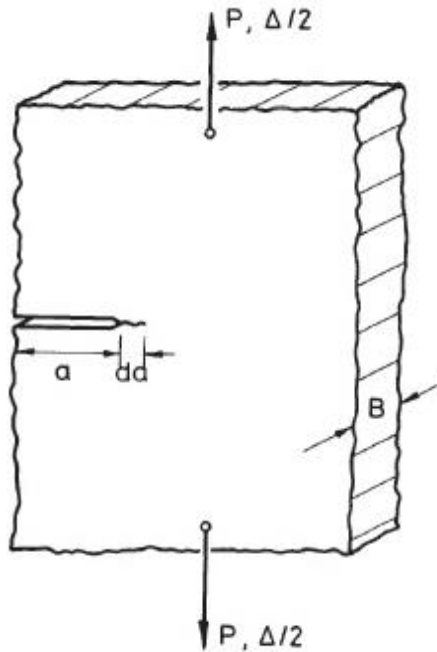


Figure 2-2 Crack extension in an arbitrary cracked body [16].

For an elastic material, the point A' is on the loading line OA' of the same body having a crack length $(a + da)$. The shaded area dU in Figure 2-3 is, therefore, the energy required to extend the crack by an amount da and G becomes

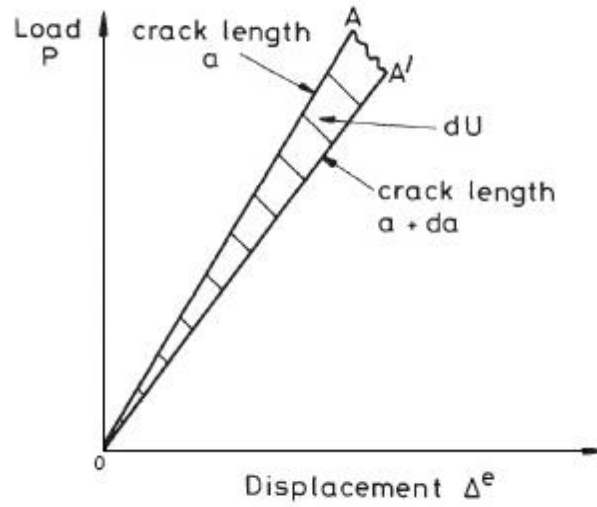


Figure 2-3 Elastic load displacement response for crack sizes differing by da [16].

$$G = \frac{dU}{Bda} \quad (2-7)$$

Equation (2-7) may be expressed in special forms for particular loading paths. For crack extension at constant load

$$G = \frac{P}{2B} \left. \frac{\partial \Delta^e}{\partial a} \right|_P \quad (2-8)$$

In addition, for crack extension at constant displacement it becomes

$$G = \frac{\Delta^e}{2B} \left. \frac{\partial P}{\partial a} \right|_{\Delta^e} \quad (2-9)$$

Equations (2-7) to (2-9) are convenient expressions for evaluating G experimentally or by computation for any cracked body. There is a direct link between the stress intensity factor and energy characterizations of fracture through [25].

$$G = \frac{K^2}{E'} \quad (2-10)$$

where

$$\begin{aligned} E' &= E && \text{in plane stress} \\ E' &= E/(1 - \nu^2) && \text{in plane strain} \end{aligned} \quad (2-11)$$

Consequently, the state of stress around a crack tip is characterized in terms of either K or G , which can both be evaluated as a function of load and crack length for any geometry. In the Griffith theory of fracture, it is assumed that unstable fracture takes place when K and G reach their corresponding critical values, K_c and G_c respectively. For mode I loading, the critical value of K for plane strain conditions is termed the fracture toughness, K_{Ic} , and this can be realized in the laboratory from the failure load of a cracked specimen and used to predict the failure load or critical crack size in a structure. However, at elevated temperatures time dependent crack growth can take place before this value is reached.

2.1.2 *Small-Scale Yielding*

The stresses near the crack tip extent to infinity as the crack tip is approached as predicted by equations (2-1). In elastic-plastic materials, yielding at the crack tip occurs to reduce the high stresses. However, in the case of small-scale yielding the plastic deformation is contained within a small zone around the crack tip. Provided the plastic zone is sufficiently small, the surrounding elastic region can still be characterized by the same equations. However, K must be increased, to K' , to describe the higher elastic stresses away from the crack tip required to balance the reduced stresses in the plastic zone. This is represented in Figure 2-4.

An approximate estimate of K' for small-scale yielding may be made by evaluating the stress intensity factor for a crack of size $(a + r_p)$, where r_p is a plastic zone size correction shown schematically in **Error! Reference source not found.**. The value of r_p is chosen to make the two shaded areas equal so that equilibrium is maintained. This is achieved by making r_p approximately equal to the distance over which the elastic stresses exceed yield. In plane stress, the stress, σ_{yy} , directly ahead of the crack ($\theta = 0$) is equal to the yield stress, σ_y when

$$r_p = \frac{K^2}{2\pi\sigma_y^2} \quad (2-12)$$

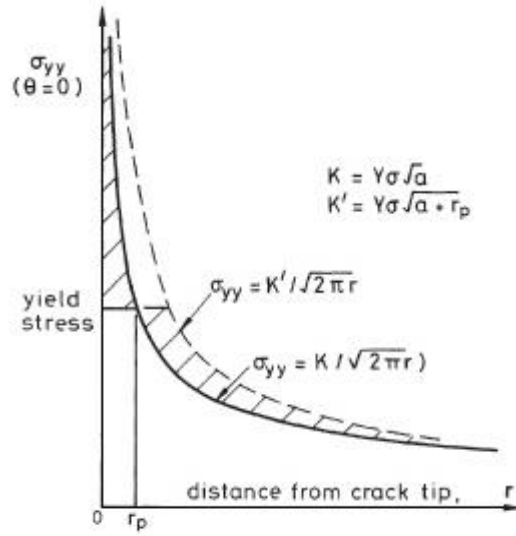


Figure 2-4 Schematic stress field ahead of a crack in small-scale yielding

This follows from the second part of equations (2-1) provided the plastic zone is buried within the region where the terms in $r^{(-1/2)}$ are dominant. In plane strain small-scale yielding, multi-axial constraint leads to yielding occurring when the stress, σ_{yy} directly ahead of the crack is approximately equal to $\sqrt{3}\sigma_y$, i.e. from equations (2-1) when

$$r_p = \frac{K^2}{6\pi\sigma_y^2} \quad (2-13)$$

Equations (2-12) and (2-13) may be written in the more general form

$$r_p = \frac{\beta K^2}{\sigma_y^2} \quad (2-14)$$

The multiplier β is influenced not only by whether conditions of plane stress or plane strain apply, but also by the remote tractions, geometry and the multi-axial yield condition, balancing of the load represented by the shaded area in Figure 2-4, and material strain hardening properties is also a function of angular position [25].

Within the plastic zone, K' characterizes the product of stress and strain, which retains the $(1/r)$ singularity of Equation (2-6). This equation is modified to

$$\sigma_{ij}\varepsilon_{ij} = \left(\frac{(K')^2}{E'}\right)r^{-1}f(\theta, material) \quad (2-15)$$

Where the angular function depends on strain hardening properties of the material and on condition of plane stress or plane strain. However, both stress and strain have an $r^{(-1/2)}$ singularity in the elastic case. In the plastic case, the stresses are lower and strains higher so that they correspond to a point on the material stress-strain curve with combined r^{-1} singularity.

2.1.3 Elastic-Plastic Fracture Mechanics

In the presence of a crack, metals give way to plastic deformation near the crack-tip prior to fracture. The degree of plastic deformation may be higher than the level that can be accommodated in the linear elastic fracture mechanics (LEFM). This has led to the development of elastic-plastic fracture mechanics (EPFM) or yielding fracture mechanics (YFM) to accommodate for ductile metals. In the early stages of the development, a simple plastic zone correction to the stress intensity factor was proposed; later an alternative plastic zone correction was developed. The first truly elastic-plastic fracture parameter, the crack tip opening displacement (CTOD), was proposed in 1961. Several years later, the J contour integral was developed, a parameter that approximates elastic-plastic deformation with a nonlinear elastic material assumption. The J integral can be viewed as both an energy parameter and a stress intensity-like quantity. In addition, J is uniquely related to CTOD under certain conditions.

2.1.4 Crack Opening Displacement Criterion

In the presence of plastic deformation, the sharp crack-tip is blunted and strains increase rapidly than the stresses. Strains become evident in the form of displacements, opening δ at the locations of crack-tip. Figure 2-5 represents the extent of deformations. It was observed through experiments of different metals that crack opens up considerably at the original physical crack-tip locations, and materials are stretched before fracturing, also defined the condition for extension of crack for such materials in terms of this opening. Since then, the crack opening displacement (COD) or crack-tip opening displacement (CTOD) regarded as a fracture resistance parameter.

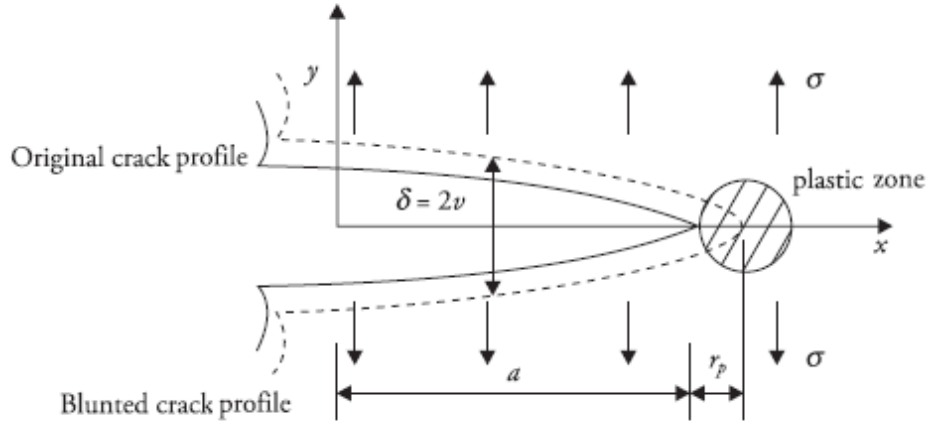


Figure 2-5 Crack-tip blunting and crack opening displacement δ

If there is plastic deformation at the crack-tip and the virtual crack size is $(a + r_p)$, then the crack opening is given by

$$\delta = \frac{4\sigma}{E} \sqrt{(a + r_p)^2 - x^2} \quad (2-16)$$

Therefore, the opening at the actual crack-tip ($x = a$) location is approximated by

$$\delta = \frac{4\sigma}{E} \sqrt{2ar_p} \quad (2-17)$$

CTOD evaluated using Irwin's plastic zone estimate and the equations for a center crack in an infinite elastic body. Specifically, from Equations (2-12) & (2-14) to obtain $\delta=2v(r_p)$ gives

$$\delta = \alpha \frac{K^2}{E\sigma_y} \quad (2-18)$$

Here, α is a numerical factor that in Wells' work was equal to $4/\pi$ and later recognized that the factor $4/\pi$ is inconsistent with an energy balance approach and subsequently

adopted $\alpha = 1$. Other values have been given from Dugdale's model for plain stress and plain strain respectively [26].

$$\delta \cong \frac{K^2}{E\sigma_y} \tag{2-19}$$

$$\delta \cong 0.49 \frac{K^2}{E\sigma_y}$$

The fracture occurs when δ goes beyond a critical value δ_c corresponding to the value of K_{IC} .

2.1.5 The J Contour Integral

The crack tip stress fields could be correlated with J –integral for nonlinear elastic materials, the use of J provides a means of directly extending LEFM behavior to fully plastic behavior Figure 2-6 illustrates the uniaxial stress-strain behavior of elastic-plastic and nonlinear elastic materials [27][28].

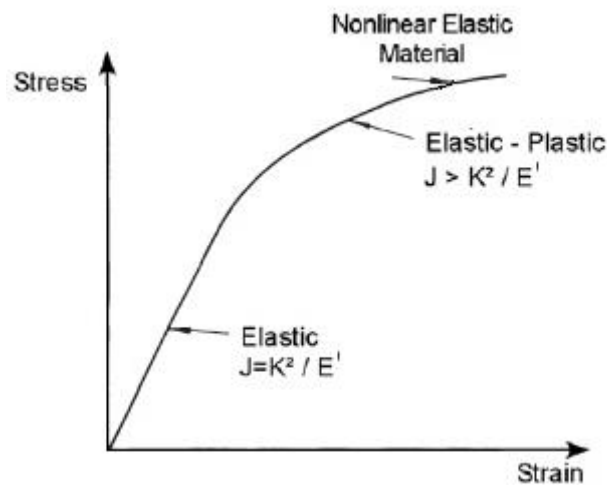


Figure 2-6 Stress-strain behavior of an elastic-plastic material

In a similar manner to the use of the stress intensity factor in LEFM, J integral can be used to describe the variations of stress and strain local to a crack tip under elastic-plastic conditions. This is defined such that the amplitude of the $(1/r)$ singularity in the product of stress and strain in Equations (2-6) and (2-15) becomes:

$$\sigma_{ij}\varepsilon_{ij} = Jr^{-1}f(\theta, material) \quad (2-20)$$

Under predominantly elastic conditions $J = G = K^2/E'$ and in small-scale yielding $J = (K')^2/E'$. For extensive conditions of plasticity occur in a structure, J is increased above these elastic values, which described schematically in Figure 2-6:

The value of J can be related to an integral defined on a contour surrounding a crack tip, Figure 2-7. The definition is [27]

$$J = \int_{\Gamma} \left[W_s dy - W_s \left(\frac{\partial u_i}{\partial x} \right) ds \right] \quad (2-21)$$

where W_s is strain energy density given by

$$W_s = \int_0^{\varepsilon_{ij}} \sigma_{ij} d\varepsilon_{ij} \quad (2-22)$$

with σ_{ij} and ε_{ij} the stress and strain tensors, respectively. T_i and u_i components of the traction and displacement vectors and s is arc length along Γ . The contour Γ is a path traversed anticlockwise which surrounds the crack tip as shown in Figure 2-7. For non-linear elastic material, J is path-independent and can be evaluated on any convenient contour when computations are performed. For linear elastic materials, J is equal to the energy release rate, G [16].

T_i would define the normal stresses acting at the boundaries. The components of the traction vector are given by

$$T_i = \sigma_{ij}n_j \quad (2-23)$$

where n_j are the components of the unit vector normal to Γ .

The Equation (2-20) has been examined for materials, which deform according to the idealized power law hardening expression

$$\varepsilon = \alpha\sigma_y \left(\frac{\sigma}{\sigma_y} \right)^n \quad (2-24)$$

where n , α , σ_y , ε_y are constants. The constants σ_y , ε_y are the yield stress and strain respectively, and $\varepsilon_y = \sigma_y/E$ when fitting Equation (2-24) to actual stress-strain data. As the product of stress and strain varies with $(1/r)$ by Equation (2-20), for the material law of Equation (2-20) the stress near the crack tip must vary as $(1/r)^{1/(N+1)}$.

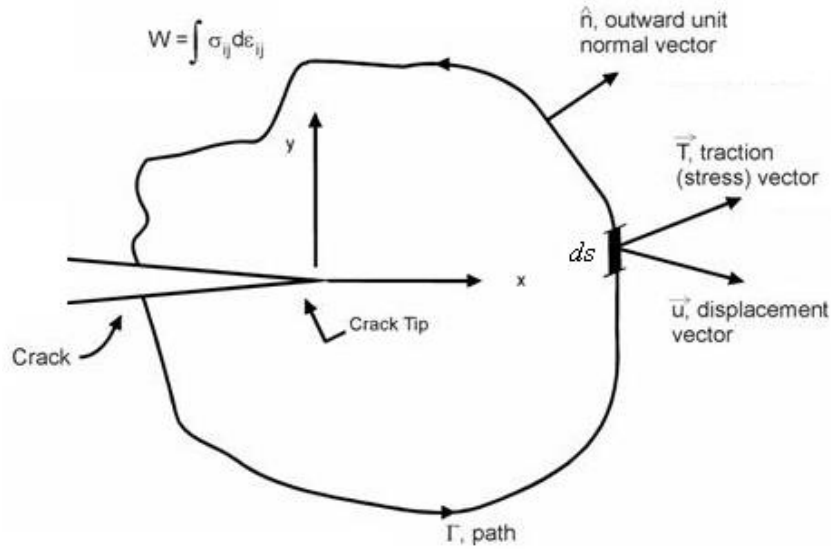


Figure 2-7 Integration contour around a crack tip

2.1.5.1 HRR Fields

As a criterion of fracture mechanics, the J -integral could be a crack tip stress or strain singularity for large-scale yielding for non-linear power-law hardening materials. Thus, J is a stress intensity parameter, which describes the amplitude of the stress and strain fields, known as HRR fields [29][30].

The HRR solutions can be expressed as

$$\sigma_{ij} = \sigma_y \left(\frac{J}{\alpha \sigma_y \varepsilon_y I_n r} \right)^{\frac{1}{n+1}} \tilde{\sigma}_{ij}(n, \theta) \quad (2-25)$$

$$\varepsilon_{ij} = \alpha \varepsilon_y \left(\frac{J}{\alpha \sigma_y \varepsilon_y I_n r} \right)^{\frac{1}{n+1}} \tilde{\varepsilon}_{ij}(n, \theta) \quad (2-26)$$

Where J is the J-integral (MPa. N or MN/m), θ and r are the polar coordinates centered at the crack tip, $\tilde{\sigma}_{ij}(n, \theta)$ and $\tilde{\varepsilon}_{ij}(n, \theta)$ are dimensionless functions that are functions of θ and n, I_n is a dimensionless integration constant that is a function of n. The numerical values of $\tilde{\sigma}_{ij}(n, \theta)$ and I_n are given in [30]. The values for the dimensionless constant I_N can be estimated from the following equations [16]

$$\begin{aligned} I_n &= 7.2\sqrt{0.12 + 1/n} - 2.9/n && \text{for plane stress} \\ I_n &= 10.3\sqrt{0.13 + 1/n} - 4.9/n && \text{for plane strain} \end{aligned} \quad (2-27)$$

2.1.5.2 J-Integral Estimation Methods

For a non-linear elastic material, J can be divided into elastic J_e and plastic J_p parts, written by

$$J = J_e + J_p \quad (2-28)$$

where the elastic part, J_e is related to the stress intensity factor K and the effective elastic modulus of the material E' which is equal to E and $E / (1-\nu^2)$ under plane stress and plane strain condition respectively

$$J_e = \frac{K^2}{K'} \quad (2-29)$$

J_p can be obtained from the plastic area under the load-displacement curve (Figure 2.9) based on the respond of load-line displacement (LLD) or crack mouth opening displacement (CMOD), expressed as [31]

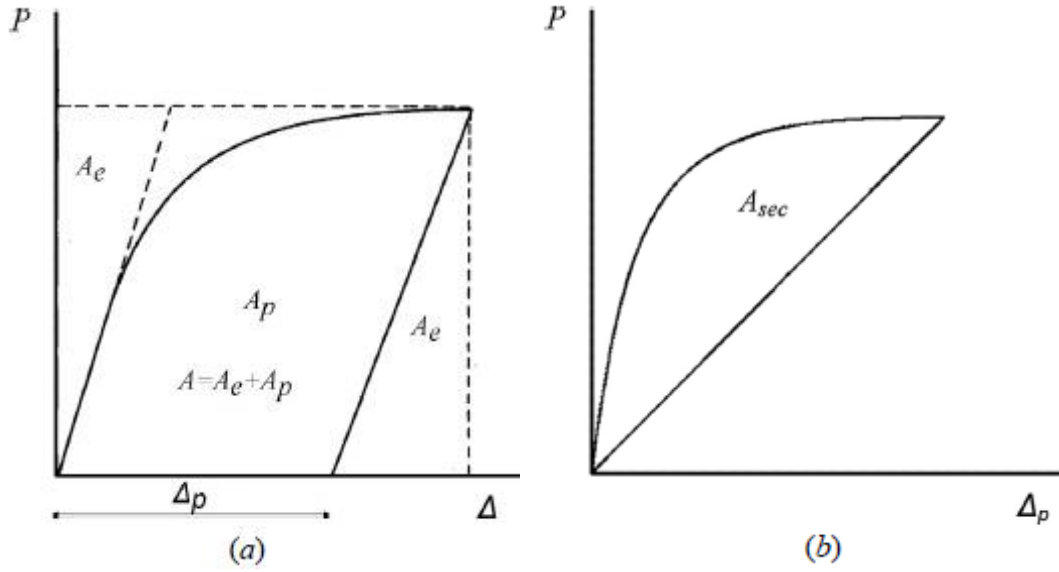


Figure 2-8 Load-displacement response and definition of (a) plastic displacement Δ_p and plastic area A_p (b) plastic secant area A_{sec} , under the load-plastic curve [31]

$$J_p = \frac{A_p^{LLD}}{B_n(W - a)} \eta^{LLD} \quad (2-30)$$

$$J_p = \frac{A_p^{CMOD}}{B_n(W - a)} \eta^{CMOD} \quad (2-31)$$

where B_n is the net thickness between the side grooves, A_p^{LLD} or A_p^{CMOD} is plastic area under the load versus load line displacement or crack mouth opening displacement, and η^{LLD} or η^{CMOD} is a nondimensional geometric factor obtained from load line displacement and crack mouth opening displacement respectively.

Both, A_p^{LLD} and A_p^{CMOD} can be obtained by integrating an appropriate load–displacement area for each cracked configurations. In addition, η is related to an appropriately chosen area of the load–displacement curve for each specimen. There are two areas, which can be selected, namely A_p and A_{sec} , shown in Figure 2-8 (a) and (b) separately. These areas are expressed as

$$A_p = \int_0^{\Delta_p} P d\Delta_p \quad (2-32)$$

$$A_{sec} = \int_0^{\Delta_p} P d\Delta_p - \frac{1}{2} P \Delta_p \quad (2-33)$$

For a power law hardening material based on Ramberg–Osgood material model, the plastic areas can then be simplified by [32]

$$A_p = \frac{n}{n+1} P \Delta_p \quad (2-34)$$

$$A_{sec} = \frac{1}{2} \frac{n}{n+1} P \Delta_p \quad (2-35)$$

Replacing the plastic areas in Equation (2-30) and (2-31) with Equation (2-34) or (2-35) the solution of J_p can be rewritten as

$$J_p = \frac{P \Delta_p}{B_n (W - a)} H' \eta \quad (2-36)$$

The parameter H' , which is used to simplify the definition of η for different geometries, relies on LLD and CMOD records and is dependent on n . The values of H'^{LLD} and H'^{CMOD} for the CT specimen geometry considered in this study are provided in Table 2-1

Table 2-1 Definition of H , H' and A for CT specimen geometry [32]

Specimen	H'^{LLD}	H'^{CMOD}	Associated Area	H'^{LLD}	H'^{CMOD}
CT	$N/(N+1)$	$N/(N+1)$	A_p	1	1

2.1.5.3 Estimation of J for CT specimen by EPRI

Electric Power Research Institution (EPRI) proposed an estimation method of J_p of cracked bodies for various fracture geometries, considering CT specimen the solution given as

$$J_p = \alpha \varepsilon_y \sigma_y (W - a) h_1(a/W, n) \left(\frac{P}{P_0} \right)^{n+1} \quad (2-37)$$

where $h_1(a/W, n)$ is the dimensionless function of the normalized crack length and stress exponent, P_0 is the limit load of unit thickness, values of which are made available in [25]. The EPRI estimation for the total value of J obtained by the sum of elastic components based on small-scale yielding solution and plastic components by

$$J_{EPRI} = \frac{K^2(a_e)}{E'} + \alpha \varepsilon_y \sigma_y (W - a) h_1(a/W, n) \left(\frac{P}{P_0} \right)^{n+1} \quad (2-38)$$

an effective crack length a_e defined by

$$a_e = a + \frac{1}{\beta \pi} \frac{(n-1)}{(n+1)} \left(\frac{K}{\sigma_y} \right)^2 \frac{1}{[1 + (P/P_0)^2]} \quad (2-39)$$

where $\beta = 2$ for plane stress, $\beta = 6$ for plane strain and $K = K(a)$. This modification essentially provides a plastic zone correction, which is set to have a reduced effect at higher loads when plasticity contributions are given by the second term in equation (2-38).

In addition, (EPRI) proposed an estimation method of limit load P_0 after studying flaw assessments for nuclear vessels. The limit load of CT specimen can be obtained by [33]

$$\begin{aligned} P_0 &= 1.455\eta(W - a)\sigma_0 && \text{plane strain} \\ P_0 &= 1.071\eta(W - a)\sigma_0 && \text{plane stress} \end{aligned} \quad (2-40)$$

where η is defined as

$$\eta = \sqrt{[(2a/c)^2 + 2(2a/c) + 2]} - [(2a/c) + 1] \quad (2-41)$$

where a is the crack length, c is the ligament length defined as $(W-a)$. For these limit load solutions are usually estimated for defects in non-work-hardening materials, adjustments

to allow for the work hardening capacity of real materials are replacing the yield strength by flow strength of the material, that is:

$$\sigma_y = \sigma_f = \frac{\sigma_s + \sigma_s}{2} \quad (2-42)$$

where σ_s is the yielding stress and σ_s is the ultimate strength.

2.1.5.4 Estimation of J in Terms of Strain at Reference Stress Approach

Large differences in calculated values of .J can arise from different fits of equation (2-24) to the stress-strain curve. It is suggested that such curve-fitting errors may be reduced by adopting reference stress techniques commonly used in creep analysis. Defining the reference stress by [34]:

$$\sigma_{ref} = \left(\frac{P}{P_0}\right) \sigma_y \quad (2-43)$$

therefore, the estimation of J using reference stress approach can be described by

$$J_{ref} = \frac{K^2(a_e)}{E'} + \mu \sigma_{ref} \left(\varepsilon_{ref} - \frac{\sigma_{ref}}{E} \right) \left(\frac{K^2(a)}{\sigma_{ref}} \right)^2 \quad (2-44)$$

where ε_{ref} is the total strain at the reference stress σ_{ref} , which can be obtained by Ramberg-Osgood equation. The value of μ depends on plane stress/strain condition where $\mu=1$ for plane stress and $\mu=1-\nu^2$ for plane strain respectively.

2.2 Definition of Creep

Plastic deformation is irreversible and it consists of time-dependent and time-independent components. In general, creep refers to the time-dependent component of plastic deformation. This means that creep is a slow and continuous plastic deformation of materials over extended periods under load. Although creep can take place at all temperatures above absolute zero Kelvin, classically creep has been associated with time-dependent plastic deformation at elevated temperatures, often higher than $0.4T_m$, where T_m is the absolute melting temperature, because diffusion can assist creep at elevated temperatures [8].

2.2.1 Creep Mechanisms

At high temperatures, the atoms of metals are active enough to move from one position to another within metal crystals. With the load applied to the material over a long time, the movements of the atoms result in creep of the material. This movement, of atoms, is caused by diffusion.

- Bulk diffusion: Interstitial and vacancy diffusion:

Diffusion in the bulk of a crystal can occur by two mechanisms. The first is interstitial diffusion. Atoms in all crystals have spaces, or gaps, between them, and small atoms dissolved in the crystal can diffuse by squeezing between atoms, jumping from one gap to another Figure 2.1 (a). Carbon, a small atom, diffuses through steel in this way.

The second mechanism is that of vacancy diffusion, occurs when an atom moves from its position to a vacancy, which may be the same size as the atom itself, as shown in Figure 2.1 (b). Most diffusion in crystals takes place by this mechanism.

- Fast diffusion Paths: Grain boundary and dislocation core diffusion:

Diffusion in the bulk crystals may sometimes be short lined by diffusion down grain boundaries or dislocation cores. The boundary acts as a planar channel, about two atoms wide, with a local diffusion rate which can be as much as 10^6 times greater than in the bulk Figure 2.1 (c). The dislocation core, too, can act as a high conductivity “wire” of cross-section about $(2b)^2$, where b is the atom size Figure 2.1 (d). At high stresses, dislocation is the dominant creep mechanism while at low stresses and high temperatures the diffusion creep is the dominant creep mechanism [35].

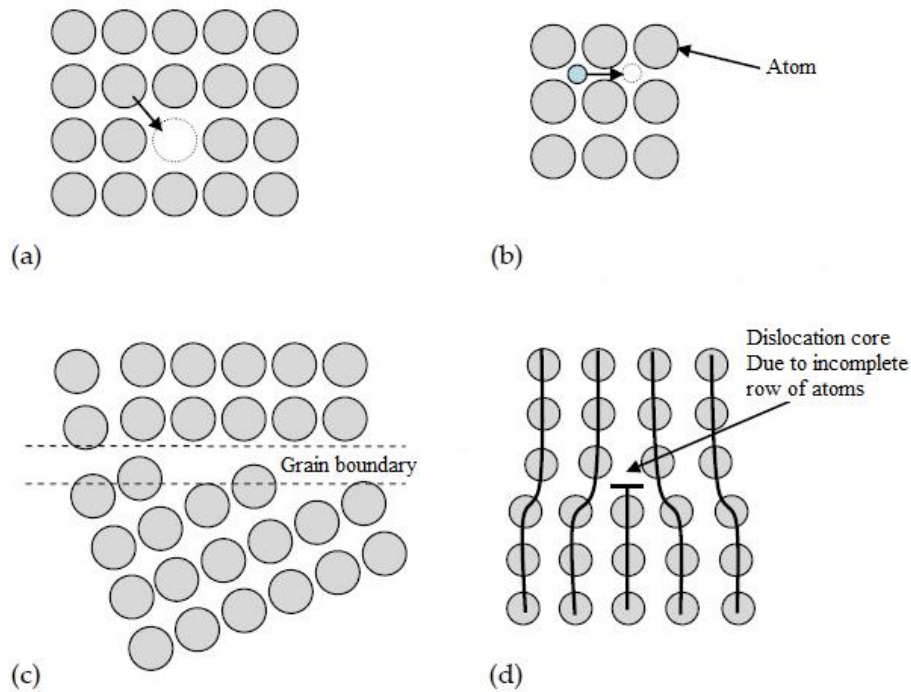


Figure 2-9 Creep mechanisms (a) Vacancy diffusion (b) Interstitial diffusion (c) Grain-boundary diffusion (d) Dislocation-core diffusion [35].

2.2.2 Creep Curves

The time-dependent deformation mechanism occurring at an elevated temperature that is generally non-reversible known as creep. Creep is most likely to occur in components that are subjected to high loads at elevated temperatures for extended periods. Creep may ultimately cause fracture or assist in developing a crack in components subjected to stresses at high temperatures. The phenomenon of creep is based on a time-dependent process whereby the material deforms irreversibly. Creep in polycrystalline materials occurs because of the motion of dislocations within grains, grain boundary sliding, and diffusion processes. A creep curve can essentially be divided into three main sections as shown in Figure 2-10. A particular material does not necessarily exhibit all the stages of creep for given testing conditions. In Figure 2-11 the representation of the rupture times versus the applied stress covers the response of the material throughout the three regimes. The primary region is a period of decreasing creep rate where work-

hardening processes dominate and cause dislocation motion to be repressed. The secondary or steady-state region of creep deformation is frequently the longest portion and corresponds with a period of constant creep rate where there is a balance between work-hardening and thermally activated recovery (softening) processes. The final stage is termed the tertiary region. This is a period of accelerating creep rate, which terminates in fracture. It can be caused by a number of factors which include an increase in stress in a constant load test, formation of a neck (which also results in an increase in stress locally), voiding and/or cracking and over aging (metallurgical instability in alloys) [36].

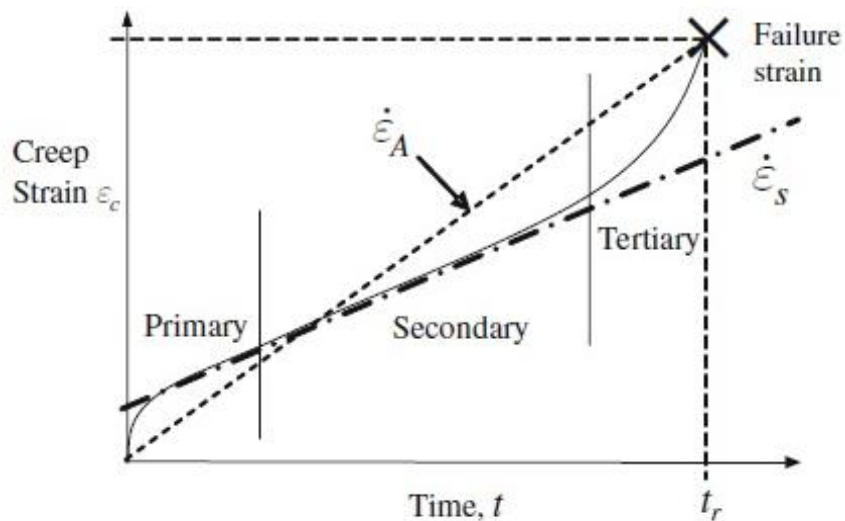


Figure 2-10 Definitions of creep strain rates representation in creep curve [36].

Creep tests can be performed either at constant load or at constant stress. For experimental convenience, most frequently the creep tests of engineering steels are achieved at constant tensile load and at constant temperature. The test results can be plotted as creep curves, which represent graphically the time dependence of strain measured over a reference or gauge length.

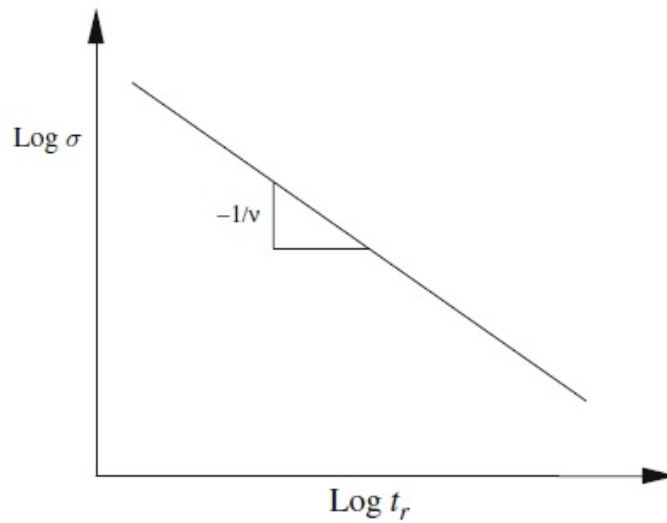


Figure 2-11 Representation of rupture times versus applied stress [36].

2.2.3 Power-Law Representation of Creep

The initial elastic and the primary creep strain cannot be neglected, they occur quickly, and they can be treated in much the way that elastic deflection is allowed in a structure, thereafter, the material enters steady state, or secondary creep, the relative length of the primary, secondary and tertiary stages in Figure 2.1 will depend on the material and testing conditions. The secondary creep is the most important creep region for most engineering materials and usually takes the longest portion in the life of creep. By plotting the log of the steady creep rate $\dot{\epsilon}_s$, against $\log \sigma$ at constant T, as shown in Figure 2-12, the relation written as:

$$\dot{\epsilon}_s = A\sigma^n \quad (2-45)$$

Where n is referred to as the steady-state creep exponent. The typical values of n for common metallic materials range from 3 to 13, A is Norton power-law constant under the secondary stage. The above equation is known as Norton's law. The reason for its popularity is its simplicity in application to stress analysis and its analogy to the Ramberg-

Osgood law. If plotting minimum creep strain rate $\dot{\epsilon}_s$, versus σ on log-log form, the values of the steady state power-law constants A and n can be extrapolated.

$$A = A' \exp(-Q_c/RT) \quad (2-46)$$

Where Q_c the activation energy for creep, R the gas constant and T the absolute temperature. The parameter A' includes microstructure parameters such as grain size. It is well known that the minimum or steady-state creep rate is inversely proportional to the time to rupture t_r as:

$$\dot{\epsilon}_{min} \text{ or } \dot{\epsilon}_s = C/(t_r)^m = A' \sigma^n \exp(-Q_c/RT) \quad (2-47)$$

Where C is a constant depending on total elongation during creep and m is a constant often nearly equal to one, Equation (2-47) is often referred to as the Monkman–Grant relationship, which has been experimentally confirmed not only for simple metals and alloys but also for a number of engineering creep resistant steels and alloys. Equation (2-47) suggests that the minimum or steady-state creep rate and the time to rupture vary in a similar manner to stress and temperature [35].

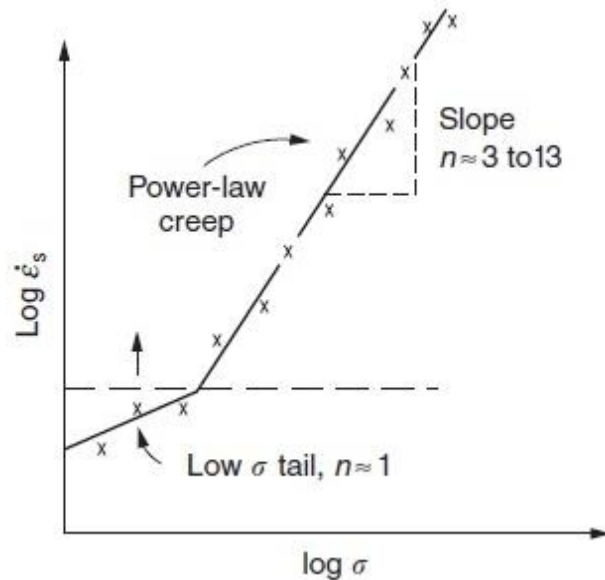


Figure 2-12 Variation of creep rate with stress [35].

2.2.4 Creep Constitutive Modelling

A constitutive equation is a relation between two or more physical quantities that are specific to the material and represents the response of that material to external influences. The requirement for a knowledge of creep constitutive behavior, $\epsilon(t, T, \sigma)$ is no longer just for scientific interest or metallurgical understanding, this is now routinely a requirement for computer-based finite element analysis (FEA) of engineering components loaded at elevated temperatures to describe the long-time creep behavior of a specified alloy type [8]. A wide range of creep model equations, which, are in use today to represent the high temperature-time dependent deformation behavior of engineering materials. Table 2-2 presents a number of classical representations of primary, secondary and tertiary creep deformation stages. A small number of the presented equations may be contained in creep constitutive models to represent the material behavior over all three creep deformation stages. This can be simply achieved by summing up the expressions representing primary, secondary and tertiary creep strains.

Table 2-2 Classical representations of primary, secondary and tertiary creep [8].

Model equation	Source reference
<i>Primary creep</i>	
Logarithmic: $\epsilon_f = a \log(1 + bt)$	Phillips (1905)
Power: $\epsilon_f = at^b$	Graham and Walles (1955)
Exponential: $\epsilon_f = a(1 - \exp(-bt))$	McVetty (1933)
Sinh: $\epsilon_f = a \sinh(bt^c)$	Conway and Mullikin (1962)
<i>Secondary creep</i>	
Power: $\dot{\epsilon}_{f,min} = d\sigma^n$	Norton (1929)
Exponential: $\dot{\epsilon}_{f,min} = d \exp(e\sigma)$	
Sinh: $\dot{\epsilon}_{f,min} = d \sinh(e\sigma)$	Nadai (1938)
<i>Tertiary creep</i>	
Power: $\epsilon_f = ft^q$	Graham and Walles (1955)
Exponential: $\epsilon_f = f(\exp(-gt)-1)$	McHenry (1943)
$\dot{\epsilon}_f = \frac{a\sigma^n}{(1-\omega)^q}$ where $\dot{\omega} = \frac{c\sigma^k}{(1-\omega)^r}$	Kachanov (1958) Rabotnov (1969)
Omega: $\dot{\epsilon}_f = \dot{\epsilon}_0 \exp(\Omega\epsilon)$	Prager (1995)

2.2.4.1 *Constitutive Equation Selection*

The creep deformation characteristics of all materials over their entire temperature application range cannot be represented by a single constitutive equation effectively. The effectiveness of a constitutive equation to model primary, secondary and/or tertiary creep deformation for specific applications can vary with material characteristics and source data distribution. In particular, not all model equations and fitting procedures are suitable for the prediction of alloy-mean long-time creep strength behavior [37].

The ability of a constitutive equation effectively to characterize the creep deformation behavior of a material depends on the following:

- **Model Fitting Approach:** model-fitting individual experimental creep curves with the selected constitutive equation (simultaneously or consecutively for individual deformation regimes) to establish the model parameters for specific conditions of T and σ , and determination of the temperature and stress dependence of the selected model parameters to define the material mean master equation for all $\varepsilon_f(T, \sigma, t)$.
- **Model Selection:** The selection of constitutive equation and model-fitting approach can depend on a number of factors including material characteristics in representing $\varepsilon(t)$ curve shape can depend on features such as the relative proportions of primary, secondary and tertiary creep as fractions of the strain and time at rupture. Data distribution which typically consists of a number of $\varepsilon(T, \sigma, t)$ curves (creep test records), each comprising a number of $\varepsilon(t)$ observations, and practical application depends on the purpose for which the material's creep strain description is required.

2.2.4.2 *Predicting Service Life*

There is no universally preferred constitutive equation for predicting service life. In practice, the selection often depends on which model best represents the high temperature deformation characteristics of the material and the preference of the analyst and/or the requirements of the available application tools.

Creep life assessment can also be determined by analyzing the stress-strain state of the structure in its entirety using detailed finite element solutions with demanding material property input data requirements or by using more simplified approaches involving some

form of reference stress, e.g. equivalent yield stress. The application of such reference stress approaches is usually limited to creep ductile materials for which both deformation and failure are controlled by the von-Mises effective stress.

2.2.5 Secondary and Average Creep Strain Rates

Creep strain rates are of the most effective features of creep curves. The minimum or secondary creep strain rate $\dot{\epsilon}_s$ and the average creep strain rate $\dot{\epsilon}_A$ are presented in Figure 2.5. Materials that exhibit low values of $\dot{\epsilon}_s$ or $\dot{\epsilon}_A$ are known as creep resistant materials when compared to those, which exhibit higher values $\dot{\epsilon}_s$ or $\dot{\epsilon}_A$, at the same stress and temperature. The minimum creep strain rate characterizes the behavior of materials in the secondary creep region. The average creep strain rate is associated with rupture data, i.e. at failure strain ϵ_f , and failure time t_f . Therefore, the average creep strain rate accounts for all the three stages of creep curves [38].

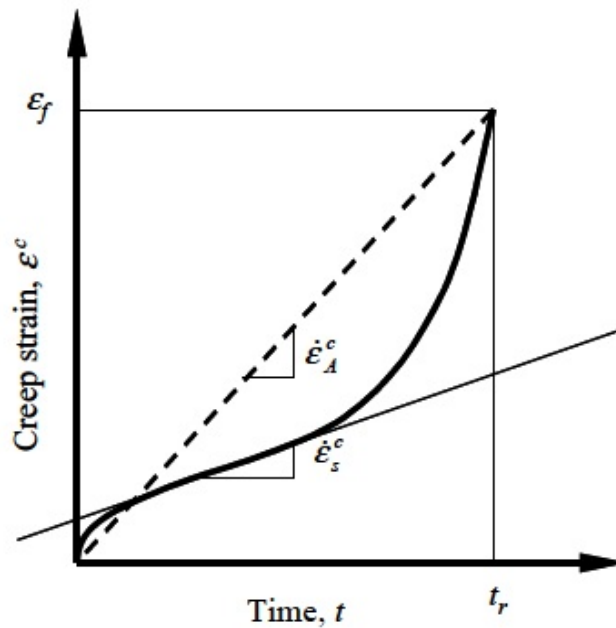


Figure 2-13 Schematic creep curve illustrating secondary and average creep rates [38].

This average creep rate $\dot{\epsilon}_A$ is defined by:

$$\dot{\epsilon}_A = \frac{\epsilon_f}{t_r} = \dot{\epsilon}_A \left(\frac{\sigma}{\sigma_0} \right)^{n_A} = A_A \sigma^{n_A} \quad (2-48)$$

Where ϵ_f is the uniaxial failure strain, t_r is the time to rupture and σ is the applied stress. The variables, σ_0 , A_A and n_A in equation (2-1) are generally taken as material constants and may depend on stress. The average creep strain rate for the P91 material was used to determine material constants, which are used to calculate fracture mechanics parameter C^* using FE methods, see Section 5.1.4.

2.2.6 Creep Strength

For plant operating at temperatures around 600°C creep is a critical factor and plant is designed to operate for a finite life (up to 250 000 hrs., i.e. nearly 30 years). With the move to higher temperatures and pressures required for more advanced supercritical plant, the materials generally used for operation in subcritical plant were unable to provide the performance required for the high temperature sections of the boiler. The ferritic steels then available were mainly 0.5Cr0.5Mo0.25V, 1Cr0.5Mo and 2.25Cr1Mo. These steels lacked sufficient creep strength and corrosion resistance for use at the higher temperatures required for supercritical operation. Although the austenitic steels offer good creep and corrosion properties, their thermal properties are relatively poor with a low thermal conductivity coupled with a high coefficient of expansion. During thermal cycling, high stresses can develop in thick-walled components, leading to thermal fatigue. It has been assessed that to avoid such unacceptable thermal stresses thick-walled components such as headers and pipework would require being heated to the operating temperature over an extended period, which would be unacceptable to plant operators meeting real-time electricity demands. Therefore, serious design and operating limitations are enforced on the plant using thick section austenitic steels. Hence, the main use of these steels is in thin section components such as superheater/reheater tubing and stub headers to take advantage of their improved creep and corrosion properties.

The solution adopted was the introduction of martensitic creep resistant steels containing either 9% or 12%Cr, as these show high thermal conductivity with relatively low thermal expansion. These steels are fully air hardening and develop a fully martensitic structure

even after slow air cooling from the solution treatment temperature and, in part, their improved creep strength is derived from this martensitic matrix. To control the high hardness and brittle behavior normally associated with martensitic materials low carbon levels were employed. Specified nitrogen levels were also introduced as this element increases both the hardenability and the creep strength. Currently, these creep resistant martensitic steels are the desired materials for the construction of components in supercritical boilers. In many cases, the parent material properties of the alloy may be ideal but it must be possible to produce the required product forms, normally tube and pipe, and to join and form them under both factory and site conditions [39].

2.2.7 Creep Resistant Martensitic Steels

The first of the creep resistant martensitic steels to be commonly used in power generation plant was the European 12Cr steel known as 'X20' (from the DIN designation X20CrMoV 12 1). The chemical composition for X20 presented in Table 1, which differs from the steels now used in that it has a higher carbon content. This steel exhibits very good creep strength and has been used in Europe in high temperature areas of subcritical boilers. However, concerns exist over the fabrication and welding of this material. Welding has to be performed using a high preheat temperature (up to 400°C) and, on thick section weldments, cracking can occur when the weld is cooled to room temperature. In addition, the hardness of weldments is very high in welding condition and stress corrosion cracking may develop in such welds if they experience damp conditions prior to post weld heat treatment. Because of these fabrication difficulties, there was a great need in the production of a material with equal or improved creep properties that led to the development of the 9Cr martensitic steels, which have now replaced X20 as the desired material. Development of 9Cr1Mo steel was as early as 1936 for use in the oil industry to provide improved corrosion resistance over 2.25Cr1Mo. The use of this steel in the form of tubes starting in 1970s, at the UK nuclear power facilities. Although the creep strength was adequate for these applications, it was lower to that of X20 and therefore efforts were made to improve it. An early attempt resulted in a 9Cr2Mo steel known as EM2 that had improved creep strength but suffered from in service

embrittlement and low creep ductility. This has led to the an improved 9Cr1Mo steel without the problems associated with EM2 which resulted to the alloy development of Grade 91 (P91), and had a lower carbon content than the original 9Cr1Mo steel coupled with small additions of vanadium and niobium to retain strengthening precipitates, hardenability and the creep strength [39].

Table 2-3 Chemical Compositions of 9% Cr and 12% Cr martensitic steels [39].

	X20 20CrMo V12	P91	E911	NF616	HCM12A	TB12M	NF12
C %	0.17-0.23	0.08-0.12	0.10-0.13	0.07-0.13	0.07-0.14	0.10-0.15	0.08
Si %	0.5 max.	0.20-0.50	0.10-0.30	0.5 max.	0.5 max.	0.5 max.	0.05
Mn %	1.00 max.	0.30-0.60	0.30-0.60	0.30-0.60		0.40-0.60	0.5
P %	0.03 max.	0.02 max.	0.02 max.	0.02 max.	0.02 max.	0.02 max.	—
S %	0.03 max.	0.01 max.	0.01 max.	0.01 max.	0.01 max.	0.01 max.	—
Cr %	10.0-12.5	8.00-9.50	8.50-9.50	8.50-9.50	10.0-12.5	11.0-11.3	11
Mo %	0.80-1.20	0.85-1.05	0.90-1.10	0.30-0.60	0.25-0.60	0.40-0.60	0.15
Ni %	0.30-0.80	0.40 max	0.40 max.	0.40 max.	0.50 max.	0.70-1.00	0.5
Nb %	—	0.06-0.10	0.060-0.10	0.04-0.10	0.040-0.10	0.04-0.09	0.07
V %	0.25-0.35	0.18-0.25	0.15-0.25	0.15-0.25	0.15-0.30	0.15-0.25	0.2
W %	—	—	0.90-1.10	1.50-2.00	1.50-2.50	1.60-1.90	2.6
Al %	—	0.04 max.	—	0.04 max.	0.04 max.	0.01 max.	—
N %	—	0.03-0.07	0.05-0.08	0.03-0.07	0.04-0.10	0.04-0.09	0.05
B %	—	—	—	0.001-0.006	0.005 max.	—	0.004
Co %	—	—	—	—	—	—	2.5

2.2.8 Mod - 9Cr1Mo Steel (P91)

P91 material is an ASTM grade of steel used to manufacture main steam pipes that are used in the fossil fuel and nuclear power plants. This material was first developed in the US in the early 1980s and was introduced to the industry in the early 1990s. P91 material is a modified form of P9 (9Cr 1Mo steel) material. The Mod – 9Cr1Mo steel is used in both boilers and in steam turbines for many components including pipes, headers, rotors, casings and chests with a maximum operating temperature of ~620°C [40]. These alloys have lower coefficients of thermal expansion and higher thermal conductivities than

austenitic steels and should, therefore, be more resistant to thermal cycling. In boilers, these steels are used for tubing in superheaters and reheaters, the high allowable stress, of P91 material, enabled engineers to design pipes with thinner walls. Figure 2-14 shows a cross-section of a pipe fabricated from different steels. The figure compares the pipe thicknesses of different steels required to operate with steam at 593.3°C and 320 bar (USC steam parameters) [10].

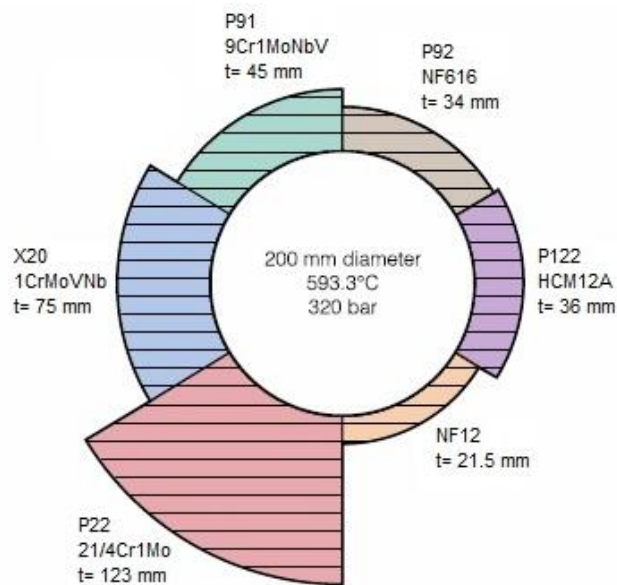


Figure 2-14 Comparison of nominal pipe thickness for different steels [10].

The P91 alloy composition was modified with addition of small amount of V, Nb, and N. This led to the considerably improved creep and tensile strength and excellent ductility and toughness. This grade has been called “ Mod-9Cr1Mo or 9Cr1MoV and was incorporated into the ASME specifications as SA-213-T91 for tubing, SA-387-Grade 91 for plates, SA-335-P91 and SA-369-FP91 for pipe and SA-182-F91 and SA-336-F91 for forgings. Figure 2-15 shows the microstructure of Mod. P91 Base metal material.

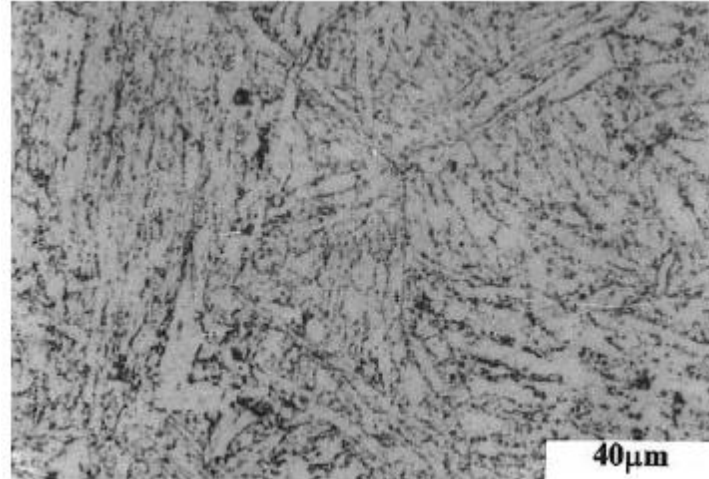


Figure 2-15 Microstructure of Mod. P91 BM [41].

2.3 Deformation and Fracture at High Temperature

High temperature deformation and fracture is truly an integrative subject. The many theories developed for high temperature deformation and fracture are mainly based on dislocation and diffusion, but every stage of their development resorts to the fundamental principles of solid state physics, physical metallurgy, elastic-plastic mechanics, fracture mechanics and damage mechanics, and so forth. High temperature deformation and fracture have long been one of the most active research topics in materials science and engineering. Since the 1970s, remarkable progress has been achieved in developing the relevant microscopic models and theories. For the time being, research and development activity has also been extensively carried out on new high temperatures materials such as intermetallic compounds, ceramics, polymers and composite materials, and a great amount of experimental data have been documented.

2.3.1 Deformations under Creep Conditions

Deformation and fracture of materials under elevated temperature creep conditions are time-dependent processes. At temperatures below some 30 percent of the absolute melting temperature, it is a reasonable and widely used idealization to consider the elastic-plastic behavior of metals as time-independent. The strain developed instantaneously in response to a load is large compared to the additional strain, which is accumulated within any practically time of interest. Many technical applications, however, require temperatures far beyond the time-independent regime, which ends at some 400 °C for ferritic steels, for example. Then the continuing plastic deformation (creep) under sustained load, which eventually leads to creep fracture, often becomes the determining factor for the design of a structure. However, the fracture mechanisms are usually closely related to the preceding deformation processes [15].

2.3.2 Elastic-Plastic Deformation

The total strain accumulated in a body can be expressed as the sum of time independent strain and time-dependent creep, $\varepsilon_c(t)$, components whereas the time-independent component can be divided into elastic ε_e and plastic ε_p parts:

$$\varepsilon_{total} = \varepsilon_e + \varepsilon_p + \varepsilon_c(t) \quad (2-49)$$

This expression is usually known as the “theory of total creep deformation” which in particular describes the behavior of the material in the steady-state creep region [42].

The elastic component of total strain under uniaxial conditions is represented by

$$\varepsilon_e = \sigma/E \quad (2-50)$$

where σ is the applied stress and E is the elastic (Young’s) modulus of the material. The plastic strain may be described using a power law equation as

$$\varepsilon_p = \alpha \varepsilon_{p0} \left(\frac{\sigma}{\sigma_{p0}} \right)^N = A_p \sigma^N \quad (2-51)$$

where N is the power law plasticity stress exponent, ε_{p0} and σ_{p0} are the normalizing strain and stress for plasticity, respectively, and α and A_p are constants which can be related by $A_p = \frac{\alpha \varepsilon_{p0}}{\sigma_{p0}^N}$

It may be assumed that under stresses less than yield strength, σ_y , the material behaves linearly while a power law equation relates stress and strain at stresses beyond yield. The linear and non-linear behavior of material under uniaxial stress can be written as

$$\frac{\varepsilon}{\varepsilon_y} = \frac{\sigma}{\sigma_y} \quad \text{for } \sigma < \sigma_y \quad (2-52)$$

$$\frac{\varepsilon}{\varepsilon_y} = \left(\frac{\sigma}{\sigma_y} \right)^N \quad \text{for } \sigma > \sigma_y \quad (2-53)$$

where $\varepsilon_y = \frac{\sigma_y}{E}$ is the yield strain. Note the yield stress in Equations (2-51) and (2-52) is often taken as 0.2% proof stress, $\sigma_{0.2}$, of the material.

2.3.3 Ramberg-Osgood Material Model

During plastic deformation, work hardening or strain hardening would occur due to dislocation generation and movement within the crystal structures of the materials. Ramberg-Osgood material model is commonly used to describe the stress-strain behavior of strain hardening materials. It provides a smooth continuous curve for the total strain in terms of stress, with no distinct yield point, and it can be defined by [43].

$$\varepsilon = \frac{\sigma}{E} + A_p \sigma^N \quad \text{uniaxial form} \quad (2-54)$$

$$\frac{\varepsilon}{\varepsilon_{p0}} = \frac{\sigma}{\sigma_{p0}} + \alpha \left(\frac{\sigma}{\sigma_{p0}} \right)^N \quad \text{non - dimensional form} \quad (2-55)$$

Typical stress-strain curve in Ramberg-Osgood relation is illustrated in Figure 2-16. The hardening behavior of the material relies on the material constants, α and N . The normalizing strain, ε_{p0} , can be considered as a yield offset. For most materials, the yield offset is equal to the accepted value of $\varepsilon_{p0} = 0.002$, the corresponding normalizing stress is then taken to be the 0.2% proof stress, written as $\sigma_{0.2}$. Due to the power-law form in Ramberg-Osgood model, plastic strain is always considered small for very low levels of stress ($\sigma < \sigma_{0.2}$). Under this circumstance, the non-linear (plastic) term in Equation (2-55) remains negligible, while the linear term dominates. On the other hand, when ($\sigma > \sigma_{0.2}$), progressively dominated plastic strain results in a magnified power-law distribution, under such condition, the linear component in Equation (2-55) becomes negligible.

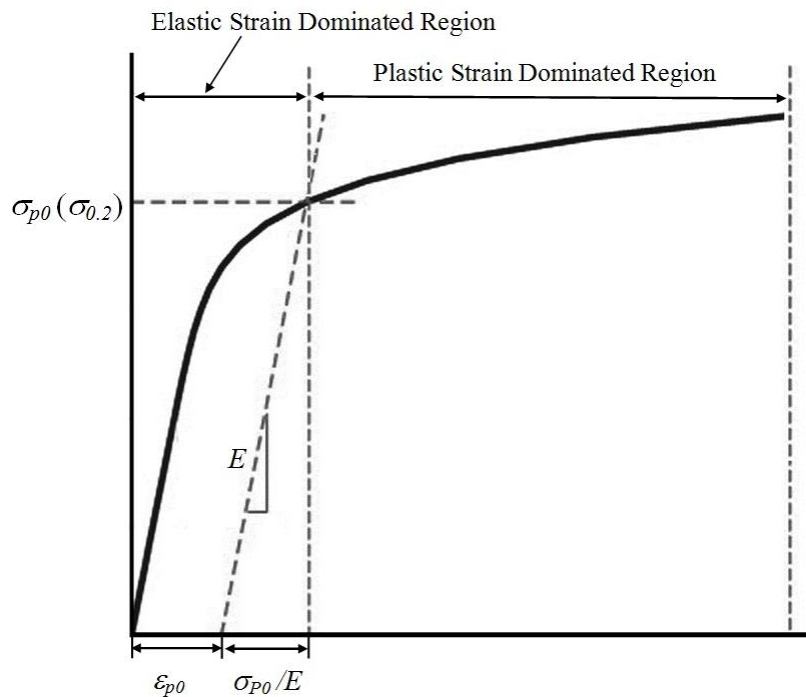


Figure 2-16 Typical stress-strain in Ramberg-Osgood material model

2.3.4 Multi-axial Deformation

The previous discussion on stress-strain behavior is based on uniaxial conditions. However, in practice, the body is majorly subjected to a multi-axial stress state, in this case, the effects of the stresses that are applied in different directions cannot be superimposed linearly. Two classical plasticity theories are commonly used to determine whether and when the yield occurred under multi-axial deformations. The interpretations of Tresca criterion is that a critical value of shear stress stored in engineering materials; while von Mises criterion suggests a yield occurs when distortional (shear strain) energy reaches a critical value. In fracture mechanics, von Mises criterion is generally applied to predict yielding of materials under any loading conditions from the results of uniaxial tensile tests. The equivalent stress, denoted as σ_{eq} , is in the function of principle stresses as

$$\sigma_{eq} = \sqrt{\frac{1}{2} [(\sigma_1 - \sigma_2)^2 + (\sigma_1 - \sigma_3)^2 + (\sigma_2 - \sigma_3)^2]} \quad (2-56)$$

where $\sigma_1, \sigma_2, \sigma_3$ are principle stress components. Note that under uniaxial condition, $\sigma_2 = \sigma_3 = 0$, von Mises stress is then equal to the principle stress, i.e. $\sigma_{eq} = \sigma_1$. The hydrostatic (or mean) stress, denoted as σ_h , is required consideration. It is defined as the average of the three normal stress components of any stress tensor as

$$\sigma_h = \frac{\sigma_1 + \sigma_2 + \sigma_3}{3} \quad (2-57)$$

2.3.5 Limit Load and Reference Stress Concepts

The concepts of limit load and reference stress have been widely applied in structural engineering design and components' integrity assessments. The limit (or plastic collapse) load describes a maximum sustainable load of the uncracked or cracked body made of elastic-perfect plastic materials ($N \rightarrow \infty$) and is often used to determine the carrying capacity of structures. Knowledge of limit load can aid designing mechanical properties

of components and structures since limit load provides information of the modes of failure associated with load-controlled effects [44]. The reference stress method has been employed for estimating structural integrity of components with and without defects in either below or within the creeping range of temperatures. The reference stress is defined by

$$\sigma_{ref} = \sigma_{0.2} \frac{P}{P_{LC}} \quad (2-58)$$

The normalized reference stress $\sigma_{ref} / \sigma_{0.2}$ denotes the level of plasticity in structural components. If the ratio is less than unity, components may store a limit level of plasticity; if the ratio is greater than unity, amount of plasticity in the components is expected. The limit load, P_{LC} in Equation (2-58) is the function of normalized crack size and specimen thickness. P_{LC} is related to the yield stress, σ_{eq} (or σ_{eq}) whilst σ_{eq} is independent of σ_{eq} . The value of σ_{eq} under plane strain condition is generally greater than that under plane stress condition [25].

2.4 Time-Dependent Fracture Mechanics

Extension of cracks under the application of fixed load conditions gives rise to time dependent fracture mechanics. More commonly referred to as creep crack growth, time dependent fracture mechanics utilizes analytical solutions to describe the transient behavior of cracks. Components that operate at high temperatures relative to the melting point of the material may fail by slow, stable extension of macroscopic crack in creeping material. Traditional approaches to design in the creep regime apply only when creep failure is controlled by a dominant crack in the structure.

2.4.1 Creep Crack Growth

Creep crack growth in metals is an important design consideration for several high temperature components. The Ct parameter, C^* -integral, and the stress intensity

parameter K , as crack tip parameters suitable for characterizing creep crack growth in metals.

Deformation at high temperatures can be divided into 4 regimes: instantaneous (elastic) strain, ϵ_0 , primary creep, secondary (steady state) creep, and tertiary creep. The elastic strain occurs immediately upon application of the load; the elastic stress-strain response of a material is not instantaneous but viewed as instantaneous in such creep problems, where the time scale is usually measured in hours. Primary creep dominates at short times after the load is applied where the strain rate decreases with time as the material strain hardens. In the secondary creep stage, the deformation reaches a steady state, where the strain hardening and softening are balanced. The creep rate is constant in the secondary stage. In the tertiary stage, the creep rate accelerates, as the material approaches ultimate failure. Microscopic failure mechanisms such as grain boundary cavitation nucleate in this final stage of creep.

During growth of microscopic crack at high temperatures, all four type of creep response can occur simultaneously in the most general case as it is realized in Figure 2-17. The material at the tip of the growing crack is in the tertiary stage of creep since the material is failing obviously locally. The material may be elastic remote from the crack tip, and in the primary and secondary stages of creep at moderate distances from the tip.

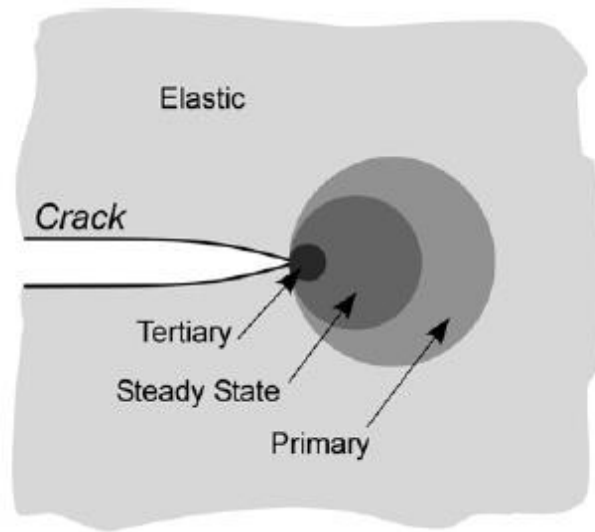


Figure 2-17 Creep response zones at a crack tip [25]

Most analytical treatments of creep crack growth assume limiting cases, where one or more of these regimes are not present or confined to a small portion of the component. If, for example, the component deformation is predominantly elastic, and the creep zone is confined to small region, near the crack tip, the crack growth can be characterized by the stress intensity factor, K . In the other extreme, when the component deforms globally in steady state extensive creep, elastic strains and tertiary creep can be disregarded [16].

There are two competing mechanisms involved in creep crack growth. The creep deformation is characterized by crack-tip blunting in the material ahead of the crack tip. This relaxes the crack-tip stress field and tends to retard crack growth. The other mechanism results in an accumulation of creep damage in the form of microcracks and voids that enhance crack growth as they coalesce. Whichever phenomenon dominates determines whether creep crack growth takes place. Steady-state crack growth will occur when equilibrium between these two effects is achieved.

Time-dependent crack growth can result from creep effects as well as environmental effects or from combination of both. An oxidizing environment can accelerate the creep crack growth rate by an order of magnitude or more. In many tests, no attempt was made to separate the effects. This has made the interpretation and comparison of data difficult.

Efforts have concentrated on trying to identify the loading parameter with which the crack growth rate correlates regarding the operating conditions of the material. The most commonly employed loading parameters are the elastic stress intensity factor, K , the energy rate integral, $C^*(t)$, and the reference stress σ_{ref} , depending on the loading conditions and the crack tip deformation regimes [45].

2.4.2 Crack-Tip Parameters

Three regimes of crack growth namely, small-scale, transient, and steady state can be distinguished for materials exhibiting elastic, power-law creep behavior, depending on the size of the crack-tip creep zone relative to the specimen dimensions, as presented in Figure 2-18. Creep crack growth usually begins under small-scale conditions and, as the creep proceeds, the steady-state creep conditions develop. In between, the specimen passes through the transition creep conditions. The transition time, t_1 , from small-scale creep to steady-state creep conditions depends on several factors, including specimen geometry and size, load level, loading rate, temperature, and the kinetics of the creep. During the small-scale and transition creep conditions, the size of the creep zone and the stress at the crack tip change continuously with time. Under large-scale creep conditions, the crack-tip stress no longer changes with time. Therefore, this regime is known as the steady-state regime. The nature (plasticity or creep) and size of the crack-tip deformation zone relative to the size of the specimen determine which of the parameters K , J , C^* , $C(t)$, and C_t might be applicable to a given situation. For creeping materials, description of the phenomenology surrounding C^* , C_t , and $C(t)$ is adequate. The parameters K and J , which do not account for time-dependent strain that occurs in the creep regime, are not applicable here [46].

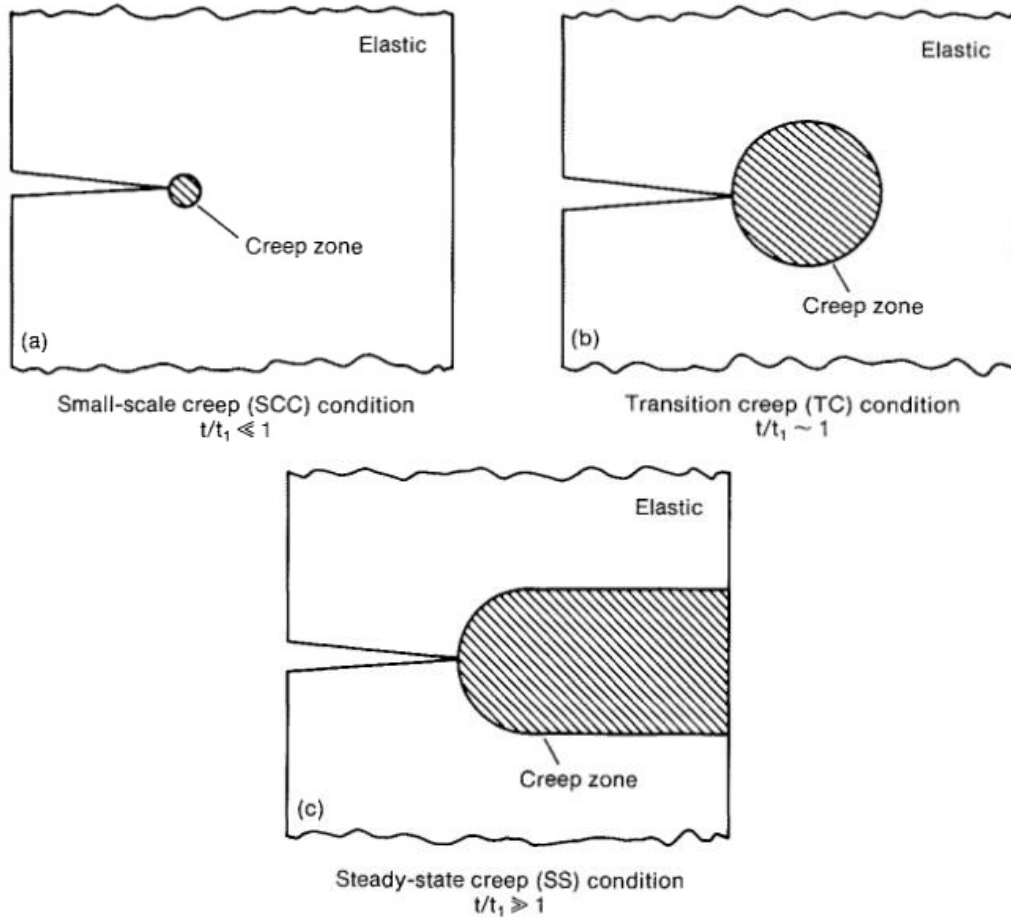


Figure 2-18 Schematic representation of levels of creep deformation [46]

2.4.3 The C^* Parameter

This parameter specifically addresses the steady state (large scale) creep crack growth regime. Under steady-state conditions, the path-independent integral C^* is defined as

$$C^* = \int_{\Gamma} \left(\dot{W}_s dy - T_i \frac{\partial \dot{u}_i}{\partial x} \partial s \right) \quad (2-59)$$

where \dot{W}_s is the strain energy density rate, defined as

$$\dot{W}_s = \int_0^{\dot{\epsilon}_{ij}} \sigma_{ij} d \dot{\epsilon}_{ij} \quad (2-60)$$

T_i is the traction vector along the path Γ that originates at a point along the lower crack surface, goes counterclockwise, and ends at a point on the upper crack surface. Thus, the contour encloses the crack tip. The terms σ_{ij} and $\dot{\epsilon}_{ij}$ are the stress and strain rate tensors, \dot{u}_i is the deflection rate vector along the direction of the traction, and ds is a length element along Γ . The C^* parameter is analogous to the J contour integral (shown in Equation (2-21) and (2-22), and Figure 2-7) with the difference that strain and strain energy density are replaced by strain rate and strain energy rate density, respectively. When secondary creep dominates, for a given crack length and loading conditions, C^* will be independent of time, and subject to the same restrictions with respect to path independence as J . Also if secondary creep follows a power law

$$\dot{\epsilon}_{ij} = A\sigma_{ij}^n \quad (2-61)$$

where A and n are material constants. It is possible then to define an HRR-type singularity for stresses and strain rates at the crack tip when $r/a \rightarrow 0$ [47]

$$\sigma_{ij} = \left(\frac{C^*}{AI_n r} \right)^{\frac{1}{n+1}} \tilde{\sigma}_{ij}(n, \theta) \quad (2-62)$$

$$\dot{\epsilon}_{ij} = \left(\frac{C^*}{AI_n r} \right)^{\frac{1}{n+1}} \tilde{\epsilon}_{ij}(n, \theta) \quad (2-63)$$

where a is the crack length, r is the distance from the crack tip, θ is the angle from the plane of the crack, and the constants I_n , $\tilde{\sigma}_{ij}$ and $\tilde{\epsilon}_{ij}$ are identical to the corresponding parameters in HRR relationship presented in Section 2.1.5.1, note that, here, n is creep exponent rather than strain hardening exponent. Just as the J integral characterizes the crack tip fields in an elastic or elastic-plastic material, the C^* integral uniquely defines crack tip conditions in a viscous material. Therefore, the time dependent crack growth

rate in a viscous material should only depend on the value of C^* . Experimental studies have shown that creep crack growth rates correlate very well with C^* , provided steady state creep is the dominant deformation mechanism in the specimen [48][49]. The crack growth rate follows the power law

$$\dot{a} = D_0 C^* \phi \quad (2-64)$$

where D_0 and ϕ are material constants, and $\phi = n / (n + 1)$ for many materials which predicted by grain boundary cavitation models. Experimental measurement of C^* is done in analogy to the J-integral. J is evaluated by referring to the energy release rate definition

$$J = -\frac{1}{B} \left(\frac{\partial}{\partial a} \int_0^{\Delta} F d\Delta \right)_{\Delta} \quad (2-65)$$

where F is the applied load and Δ is the load line displacement. Similarly, C^* can be defined in terms of a power release

$$C^* = -\frac{1}{B} \left(\frac{\partial}{\partial a} \int_0^{\dot{\Delta}} F d\dot{\Delta} \right)_{\dot{\Delta}} \quad (2-66)$$

The J integral can be related to the energy absorbed by a testing specimen, divided by the ligament area c , which is energy per unit ligament area

$$J = \frac{1}{Bc} \int_0^{\Delta} F d\Delta \quad (2-67)$$

Therefore, C^* is given by

$$C^* = \frac{1}{Bc} \int_0^{\dot{\Delta}} F d\dot{\Delta} \quad (2-68)$$

where F is a factor which depends on specimen geometry and creep stress index n and is related to the similar factor, η used in J-estimation methods by equation (2-41).

$$F = \frac{n}{n+1} \eta \quad (2-69)$$

In this case, Equation (2-68) reduces to [16]

$$C^* = \frac{n}{n+1} \frac{1}{Bc} F \dot{\Delta} \quad (2-70)$$

2.4.4 Creep Crack Growth Models

It was proposed by Nikbin, Smith, and Webster (NSW) [48], that, as presented in Figure 2-19, a creep process zone of size r_c exists ahead of the crack tip where creep damage accumulates, and that creep damage may be measured in terms of creep ductility exhaustion. It is considered that material first experiences creep damage when it enters the process zone, thus a gradient of creep damage exists between $0 \leq r \leq r_c$.

2.4.4.1 NSW Model

Material failure occurs at the crack tip when the creep ductility is exhausted there and hence the crack extends. In the NSW model the steady state creep crack growth rate, \dot{a} is predicted using

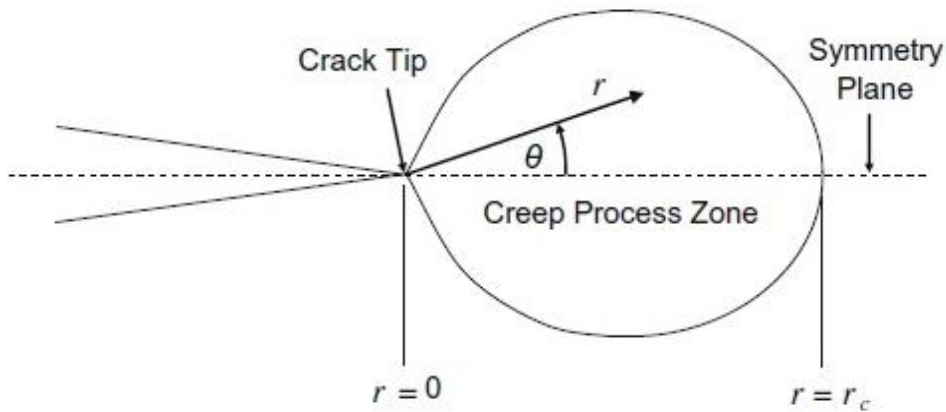


Figure 2-19 Definition of crack tip coordinates and creep process zone size, r_c [50]

$$\dot{a} = \frac{n+1}{\varepsilon_f^*} \left(\frac{C^*}{I_n} \right)^{n/(n+1)} (Ar_c)^{1/(n+1)} \quad (2-71)$$

The experimental predictions on a large number of materials showed that the creep crack growth rate is most sensitive to multiaxial creep ductility, and crack growth rates can be predicted approximately by [51]

$$\dot{a} = \frac{3C^{*0.85}}{\varepsilon_f^*} \quad (2-72)$$

where \dot{a} is in mm/h, ε_f^* is the appropriate failure strain as a fraction and C^* is in MPa m/h. In Equation (2-72) ε_f^* is the level of creep strain appropriate to the state of stress at the crack tip. For plane stress conditions ε_f^* can be taken as the uniaxial creep ductility ε_f and for plane strain conditions as $\varepsilon_f/30$. This range describes the effects of constraint on crack growth due to both material properties and size/geometric factors. Equations (2-64) and (2-72) are relevant to when steady state creep and creep damage conditions have been achieved at a crack tip.

2.4.4.2 Modified NSW Model

A modified version of the NSW model (designated NSW–MOD) has been proposed, which considers the dependence of creep strain on both the crack tip angle θ , and the creep stress exponent n , in addition to the stress state [52].

$$\dot{a}_{NSW-MOD} = (n + 1)(Ar_c)^{\frac{1}{n+1}} \left[\frac{C^*}{I_n} \right]^{\frac{n}{n+1}} \frac{\bar{h}_n}{\varepsilon_f} \quad (2-73)$$

and

$$\bar{h}_n = \frac{\tilde{\sigma}_{eq}^n(\theta, n)}{MSF(\theta, n)} \Bigg|_{max} \quad (2-74)$$

The form of Equation (2-73) is the same as that of Equation (2-72), but the dependence of $\tilde{\sigma}_{eq}$ and ε_f^* on angle θ and n is included.

At $\theta = 0^\circ$, which is the condition assumed in the NSW model, the difference in the value of $\tilde{\sigma}_{eq}(n, \theta)$ under plane stress and plane strain conditions can be up to a factor of 50-100 depending on the value of n . It is seen in Figure 2-20 that ε_f^* increases with angle both under plane stress and plane strain conditions. At $\theta = 0^\circ$, the difference of ε_f^* between plane stress and plane strain conditions is well above a factor of 100.

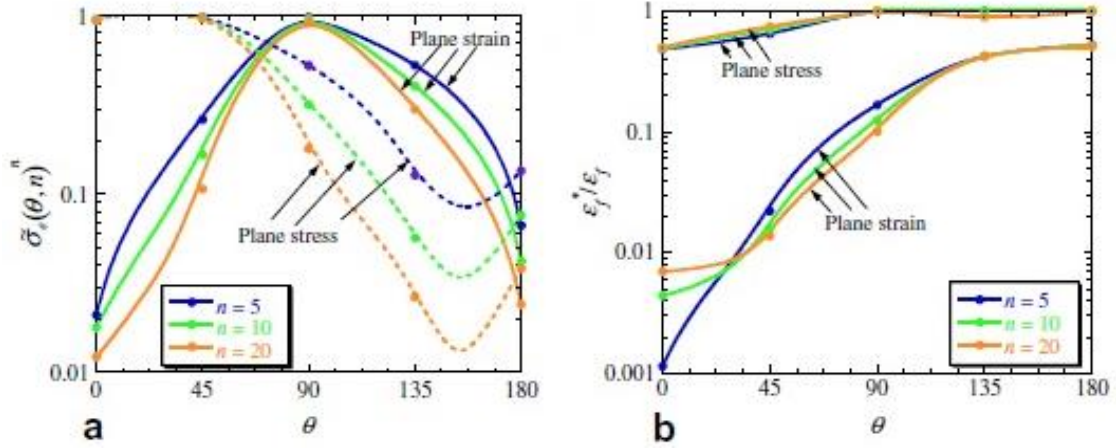


Figure 2-20 Dependence of (a) $\tilde{\sigma}_{eq}$ and (b) ϵ_f^* on angle θ and n [53]

2.4.5 Creep Crack Initiation

The initial stage of cracking exhibits a transient phenomenon due to the accumulation of damage at a crack tip prior to the onset of steady-state behavior. This can lead to an incubation period as presented in Figure 2-21 before measurable crack growth can be detected, if the minimum crack extension that can be resolved reliably is da then the incubation period is given by [51]

$$t_i = \int_0^{\Delta a} \frac{dr}{\dot{a}} \quad (2-75)$$

where dr is distance from the crack tip. Limits on t_i can be obtained by representing cracking rate by its initial value \dot{a}_0 and its steady state value \dot{a} . The initial cracking rate can be approximated to the steady state rate in Equation (2-64) by

$$\dot{a}_0 = \frac{\dot{a}}{n+1} \quad (2-76)$$

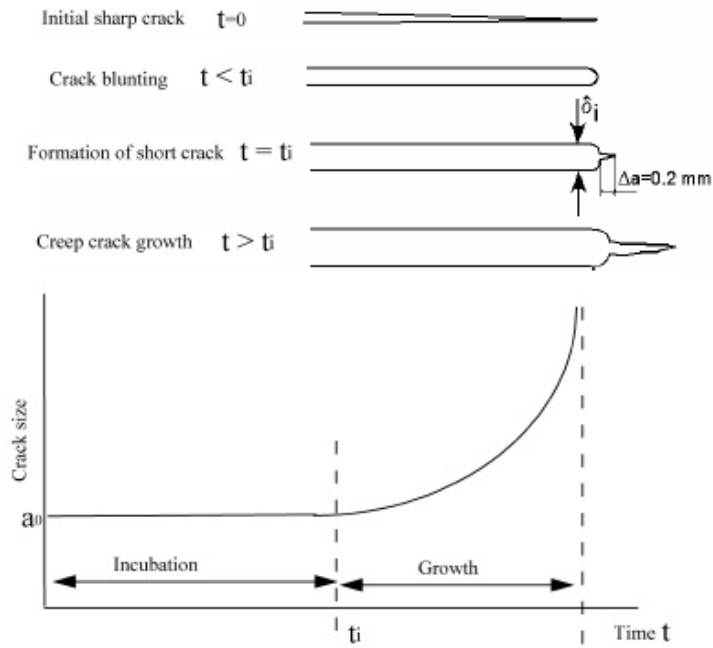


Figure 2-21 Development of crack blunting and crack initiation [51].

$$\dot{a}_0 = \frac{\dot{a}}{n + 1} \quad (2-77)$$

The process of crack tip blunting continues until the plasticity of the material at the crack tip exhausted and a critical crack tip opening displacement, δ_i , is reached as seen in Figure 2-7, this criterion is used to determine the creep crack initiation time, t_i . For ductile materials, when steady-state creep conditions are established, the creep crack initiation time can be estimated as [54]

$$t_i = \frac{1}{\varepsilon_0} \left(\frac{\sigma_0 \dot{\varepsilon}_0 \delta_i}{C^*} \right)^{\frac{n}{n+1}} \quad (2-78)$$

3 DAMAGE MECHANICS APPROACH OF WELDMENTS MODELING AT ALL CREEP STAGES

3.1 Introduction

Creep deformation is defined in three distinct stages: primary, secondary, and tertiary, creep is sensitive to stress and temperature. Diffusion flow, dislocation slip and climb, and grain boundary sliding are all basic mechanisms of creep illustrated in Figure 3-1. During the primary creep regime, dislocations slip and climb. Eventually, a saturation of dislocation density coupled with recovery mechanics in balance form the secondary creep regime. Finally, the tertiary creep regime is observed where grain boundaries slide, voids form, and coalescence, leading to rupture [55].

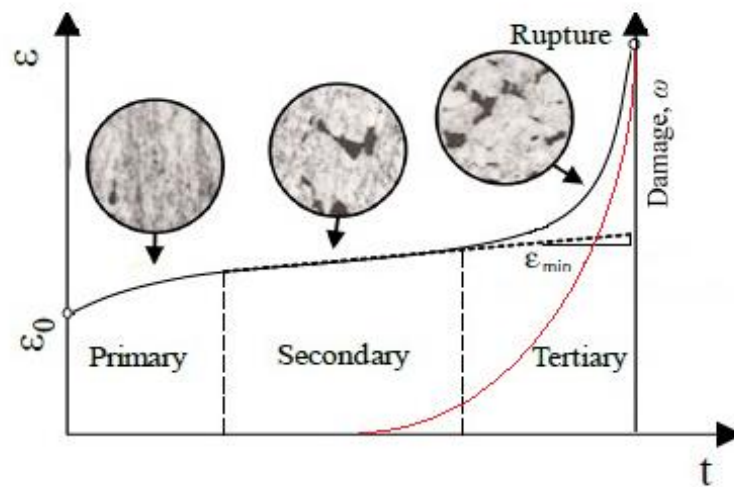


Figure 3-1 Creep deformation and damage evolution parameter [55].

Preceding efforts concentrated on modeling the minimum creep rate and predicting creep rupture through Norton's power law, considering all three-creep regimes, the required material constants can be analytically determined from experimental data. However, the Norton power law is not an appropriate representation of the creep behavior of creep resistant martensitic steels, as it does not model the tertiary creep regime.

3.2 Continuum Damage Mechanics

Fracture mechanics approaches were used to predict creep crack growth in standard specimens for steel weldments. However, it is difficult to utilize fracture mechanics for cases other than those used to predict the steady-state behavior of components. Therefore, damage mechanics approaches have been used to model all creep stages, i.e. primary, secondary and tertiary creep. Damage mechanics can, also, account for material deterioration, which will allow accurate predictions of failure times and location of creep structures. The damage mechanics approach accounts for the loss of the load carrying capacity during the creep process due to material deterioration. This loss, in the load carrying capacity, is due to the merging of the voids and microcracks that are formed on grain boundaries and lead to the material degradation, which occurs. The generalized damage mechanics approach is used to predict progressive deterioration and ultimate failure in components working under creep conditions. A life-time prediction of a specific load bearing component designed for creep, or a residual life-time estimation of a structure operating at elevated temperature requires a model which takes into account tertiary creep and damage evolution under multi-axial stress states. The damage rate and consequently the creep rate are determined by the stress level, the accumulated damage, and the temperature. These dependencies can be established based on experimental data from the uni-axial creep tests [56].

Local approach of fracture based on continuum damage mechanics (CDM) and finite element method (FEM) considered the best technique that CDM offers, the local approach of fracture enables us to track the local fields of stress, strain and fracture at a crack tip. A crack is usually identified by the completely damaged zone, where the damage state extended to its critical state. When this condition is satisfied the material in the region between the crack tip and the point of failure is assumed to rupture and the crack to advance to the failure point, this procedure is repeated until the crack reaches its critical length and failure takes place [57].

3.3 Creep Constitutive Models

Typical creep deformation can generally consist of three regimes, i.e. primary, secondary, and tertiary creep regimes. For the purpose of easy application, a model employed which considers only the average creep strain rate, $\dot{\epsilon}_{ave}^{cr}$, presented in Figure 3-2 in FE analyses of creep behavior. This simplest model can be written in the power-law form as [17][58]:

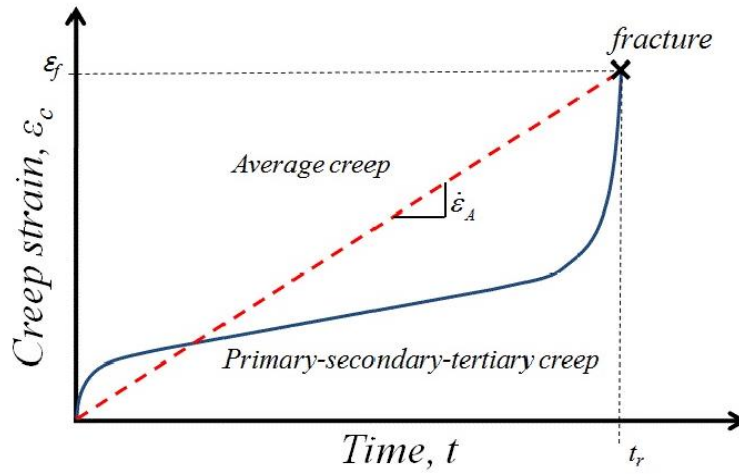


Figure 3-2 schematic illustration of a typical creep behavior [58].

$$\dot{\epsilon}_{ave}^c = A' \sigma_{eq}^{n'} \quad (3-1)$$

where A' and n' are the creep coefficient and exponent, respectively. σ_{eq} denotes the equivalent (von Mises) stress. In order to obtain an accurate description of entire creep curves, a strain-hardening creep law composed of three terms is used

$$\dot{\epsilon}_c = A_1 \sigma_{eq}^{n_1} \epsilon_c^{m_1} + A_2 \sigma_{eq}^{n_2} \epsilon_c^{m_2} + A_3 \sigma_{eq}^{n_3} \epsilon_c^{m_3} \quad (3-2)$$

where A_1 , n_1 , A_2 , n_2 , A_3 , and n_3 are material constants from creep data, and ϵ_c denotes the equivalent (von Mises) creep strain. It should be pointed out that Equation (3-4) is a

phenomenological material law. The influence of the damage variable, ω , is not included in the Equation (3-4) Although the strain-hardening creep curve equation seems to agree with the creep data well when creep softening is a consequence of plastic strain.

3.3.1 *The Kachanov and Rabotnov Model*

The phenomenological creep-damage equations were firstly proposed by L. Kachanov [59] and Rabotnov [60]. A new internal variable has been introduced to characterize the “continuity” or the “damage” of the material. The geometrical interpretation of the continuity variable starts from changes in the cross-section area of a uni-axial specimen. Specifying the initial cross-section area of a specimen by A_0 and the area of voids, cavities, micro-cracks, etc. by A_D , the Kasyanov’s continuity is defined as follows

$$\psi = \frac{A_0 - A_D}{A_0} \quad (3-3)$$

The value $\psi = 1$ indicates the fully undamaged state, the condition $\psi = 0$ corresponds to the fracture (completely damaged cross-section).

The continuous damage parameter, ω , has not necessarily a precise physical meaning such as the nucleation and growth of intergranular cavities. It is assumed that the damage parameter ω and the creep strain rate $\dot{\epsilon}$ depend not only on the stress and temperature but also on the value of ω itself. Thus in simple traction:

$$\begin{aligned} \dot{\epsilon} &= f(\sigma, T, \omega) \\ \dot{\omega} &= g(\sigma, T, \omega) \end{aligned} \quad (3-4)$$

The lifetime under creep, the deformation at fracture and the shape of the creep curves $\epsilon(t)$ are all obtained by integrating these equations between appropriate limits. Under high stress and temperature conditions, the tertiary creep regime is dominant; therefore, a damage model is necessary. A proposed interfacing the Continuum Damage Mechanics (CDM) framework with the proven Norton power law for secondary creep. In CDM, damage, ω , is assumed homogeneous and irreversible. The Kachanov- Rabotnov coupled creep-damage constitutive equations are as follows [61]:

 > Uniaxial stress:

$$\begin{aligned}\dot{\varepsilon}_{cr} &= \frac{d\varepsilon_{cr}}{dt} = A \left(\frac{\sigma_{eq}}{1-\omega} \right)^n \\ \dot{\omega} &= \frac{d\omega}{dt} = \frac{M\bar{\sigma}^\chi}{(1-\omega)^\phi}\end{aligned}\tag{3-5}$$

Where A and n are the Norton power law constants, σ_{eq} is equivalent, von Mises stress, and M, χ and ϕ are tertiary creep damage constants. The Norton power law constants A and n can be easily determined using the analytical approach, by setting Norton's power law for secondary creep equal to the minimum creep strain rate. For the tertiary creep damage constants M, χ , and ϕ there is no analytical method, therefore, numerical optimization and/or manual iteration is implemented.

> Multiaxial stress:

$$\dot{\varepsilon}_{ij} = \frac{d\varepsilon_{ij}}{dt} = \frac{3}{2} A \left(\frac{\sigma_{eq}}{1-\omega} \right)^n \frac{S_{ij}}{\sigma_{eq}} t^m\tag{3-6}$$

$$\dot{\omega} = \frac{d\omega}{dt} = B \frac{(\sigma_r)^\chi}{(1-\omega)^\phi} t^m\tag{3-7}$$

$$\sigma_r = \alpha\sigma_1 + (1-\alpha)\sigma_{eq}\tag{3-8}$$

Where ε_{ij} is the strain tensor, t is the time, S_{ij} is the deviatoric stress tensor, ω is the damage parameter, where $0 < \omega < 1$ and σ_{eq} , σ_1 and σ_r are the equivalent, maximum principal and rupture stresses, respectively. A, n, B, χ , ϕ , α and m are material constants and $0 < \alpha < 1$. The time to fracture, t_f , is found integrating the appropriate Equation (3-7) for ω with the boundary conditions $\omega = 0$ (no damage) at $t = 0$, $\omega = 1$ (fracture) at $t = t_f$. One obtains for uniaxial loading [62]:

$$t_f = \left[\frac{m+1}{B(1-\omega)\sigma^\chi} \right]^{\frac{1}{m+1}}\tag{3-9}$$

Similarly, the uniaxial creep strain versus time relationship can be obtained, i.e. from t_f , one can calculate the strain to failure:

$$\varepsilon_f^{cr} = \frac{A\sigma^{(n-\chi)}}{B(n-\phi-1)} \left(\left[1 - \frac{B(\phi+1)\sigma^\chi t^{m+1}}{m+1} \right]^{\frac{\phi-n+1}{\phi+1}} - 1 \right) \quad (3-10)$$

The material constants A, n, B, χ , ϕ , and m can be obtained from curve fitting to the experimental strain–time curves, very often $n < \chi$, so that the creep ductility is a decreasing function of the applied stress [63].

3.3.2 *The Liu and Murakami Model*

Due to examination of the suggested stress sensitivity of the conventional creep damage equations of Kachanov-Rabotnov, it was revealed that this stress sensitivity is one of the most essential causes of the damage localization and mesh-dependence in local approach of creep fracture analysis. Then in order to avoid this difficulty, alternative constitutive and evolution equations of creep and creep damage are proposed from the view point of micromechanics. Significant improvement in damage localization and the mesh dependence of the numerical results are established [64].

Equations (3-6) and (3-7) have been extensively applied to the conventional creep damage analysis of high temperature components, and were found to lead to significant damage localization and mesh dependence thus attributed mainly to the marked stress sensitivity at the final stage of damage. This stress sensitivity initiated by the term $(1-\omega)$ in the denominator, therefore to avoid this problem a modified form for the damage Equations have been introduced [65].

$$\dot{\varepsilon}_{ij} = \frac{d\varepsilon_{ij}}{dt} = \frac{3}{2} A \exp \left[\frac{2(n+1)}{\pi\sqrt{1+3/n}} \left(\frac{\sigma_1}{\sigma_{eq}} \right)^2 \omega^{3/2} \right] \sigma_{eq}^{n-1} S_{ij} \quad (3-11)$$

$$\dot{\omega} = \frac{d\omega}{dt} = B \frac{(1 + \phi)[1 - \exp(-q_2)](\sigma_r)^\chi}{q_2} \exp(q_2\omega) \quad (3-12)$$

Rupture stress σ_r was introduced in Equation (3-8), q_2 is a material constant, and σ_1 denotes the maximum principle stress. Integration of Equation (3-12), under uniaxial conditions, provides the damage, ω , for the Liu and Murakami model as:

$$\omega = \frac{1}{q_2} \ln[1 - (1 - e^{-q_2})] \frac{t}{t_f} \quad (3-13)$$

where the fracture time is given by

$$t_f = \frac{1}{M\sigma^\chi} = \frac{1}{B(1 + \phi)\sigma^\chi} \quad (3-14)$$

The material constants A, n, M, B, χ , q_2 and ϕ are obtained by curve fitting to the uniaxial creep curves [5].

3.3.3 The Cocks and Ashby Model

Both effects of the stress triaxiality, σ_1/σ_{eq} , and damage parameter ω on the creep rate have been included in Equation (3-11), practical results obtained using the previous model to simulate creep crack growth. However, the creep constitutive introduced by Liu and Murakami is not perfect either. The strain-based model based on the creep ductility exhaustion concept gives

$$\dot{\omega} = \frac{\dot{\epsilon}_c}{\epsilon_f^*} \rightarrow \omega_i = \omega_{i-1} + \dot{\omega}_i \Delta t \quad (3-15)$$

where $\dot{\epsilon}_c$ and ϵ_f^* denote the creep strain rate and the multiaxial creep failure strain, respectively. The damage parameter approaches unity when the local accumulated creep strain reaches the critical creep ductility. It is known that the creep ductility significantly depends on the stress state. One widely-used multi-axial creep ductility model based on the cavity growth theory by power-law creep was quantified by Cocks and Ashby [66].

$$\frac{\varepsilon_f^*}{\varepsilon_f} = \sinh \left[\frac{2}{3} \left(\frac{n-0.5}{n+0.5} \right) \right] / \sinh \left[2 \left(\frac{n-0.5}{n+0.5} \right) \frac{\sigma_h}{\sigma_{eq}} \right] \quad (3-16)$$

where n is the steady-state creep exponent, ε_f is the uniaxial creep failure strain, σ_h and σ_{eq} are the hydrostatic (mean normal stress) and the equivalent (von Mises) stress components respectively. The multiaxial ductility, therefore, depends on the stress triaxiality that is present at the crack tip.

3.3.4 The Wen and Tu Model

A multiaxial creep-damage model involving a new physically-based multiaxial creep ductility factor defined as $\varepsilon_f^*/\varepsilon_f$, using the local critical-strain criterion. the Cocks–Ashby cavity growth theory is modified and then a new multiaxial creep ductility factor is proposed [67].

$$\frac{\varepsilon_f^*}{\varepsilon_f} = \exp \left[\frac{2}{3} \left(\frac{n-0.5}{n+0.5} \right) \right] / \exp \left[2 \left(\frac{n-0.5}{n+0.5} \right) \frac{\sigma_h}{\sigma_{eq}} \right] \quad (3-17)$$

Using differential self-consistent method suggested by Riedel [15], the simplified evaluation of stress/strain-rate response of creep solids containing closely-spaced microcracks was given by

$$\dot{\varepsilon}_{ij}^c = \frac{3}{2} A e^{\rho} t^m \sigma_{eq}^{n-1} S_{ij} \quad (3-18)$$

where A , n , m are material constants. $\dot{\varepsilon}_{ij}^c$ and S_{ij} denote the creep strain tensor and deviatoric stress tensor, respectively. The term, t^m , is introduced to describe the primary creep behavior of Bailey type. ρ is the factor reflecting the density of cavitating surfaces defined by

$$\rho = \frac{n+1}{2\sqrt{1+3/n}} N d^3 \quad (3-19)$$

where d' is the diameter of cavitating surfaces shown in Figure 3-3. $N = 1/(\pi L^3/4)$ is the number of cavitating grain boundary facets per unit volume if we assume the cavitating facet is contained in a cylindrical cell of diameter and height, L .

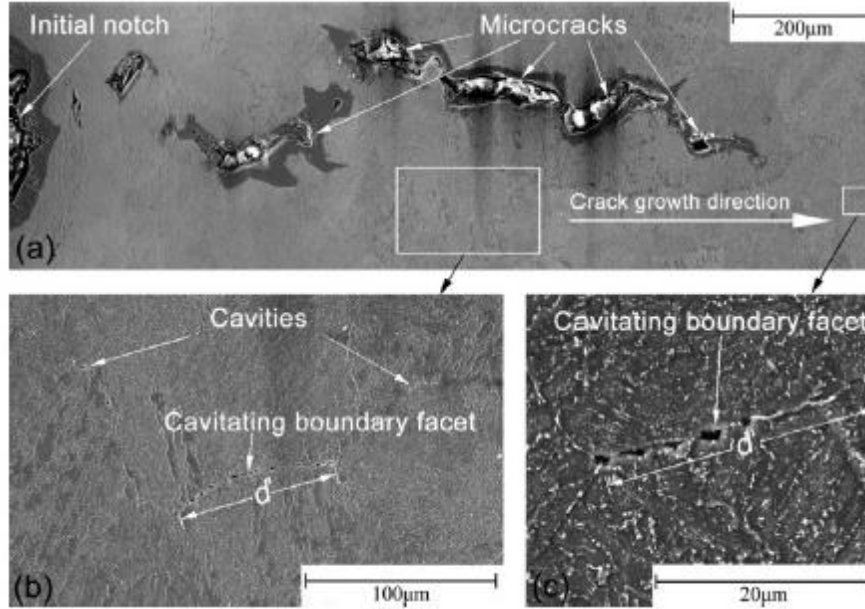


Figure 3-3 Morphology of crack growth with creep voids and microcracks in the area near the macroscopic crack in a C(T) specimen [67].

Noting that the damage can be considered as the effective area reduction in the cell i.e., $\omega = d'^2/L^2$, we can rewrite the creep constitutive equation as

$$\dot{\varepsilon}_{ij}^c = \frac{3}{2} A \sigma_{eq}^{n-1} S_{ij} \exp\left(\frac{2(n+1)}{\pi\sqrt{1+3/n}} \omega^{3/2}\right) t^m \quad (3-20)$$

Therefore, the creep-damage model, consisting of Equations (3-15), (3-17), and (3-20), has been built based on modified cavity growth and microcrack interaction theories.

3.4 The Effects of Stress Level and Stress State on the Creep Ductility

The creep ductility under uniaxial or multiaxial condition can be defined based on the elongation or reduction in area in specimen testing. The importance of uniaxial and

multiaxial creep ductility is that the component should have sufficient ductility to avoid premature/catastrophic/brittle fracture during operation at high temperature.

The relations between creep ductility (in terms of reduction in area) and stress (normalized by the 0.2% offset yield stress) for martensitic chromium steels, P91 and Gr.91 at 500–700 °C, Clearly, higher and lower shelves have been observed in relatively high and low stress levels, respectively. It also has been seen that there is a remarkable decline of creep ductility at normalized stresses near 0.3 with decrease in the stress level, without obvious temperature dependency, the creep ductility of P91 declines drastically only at 650 °C and that of Gr. 91 steel does not indicate significant drop, as shown in Figure 3-4.

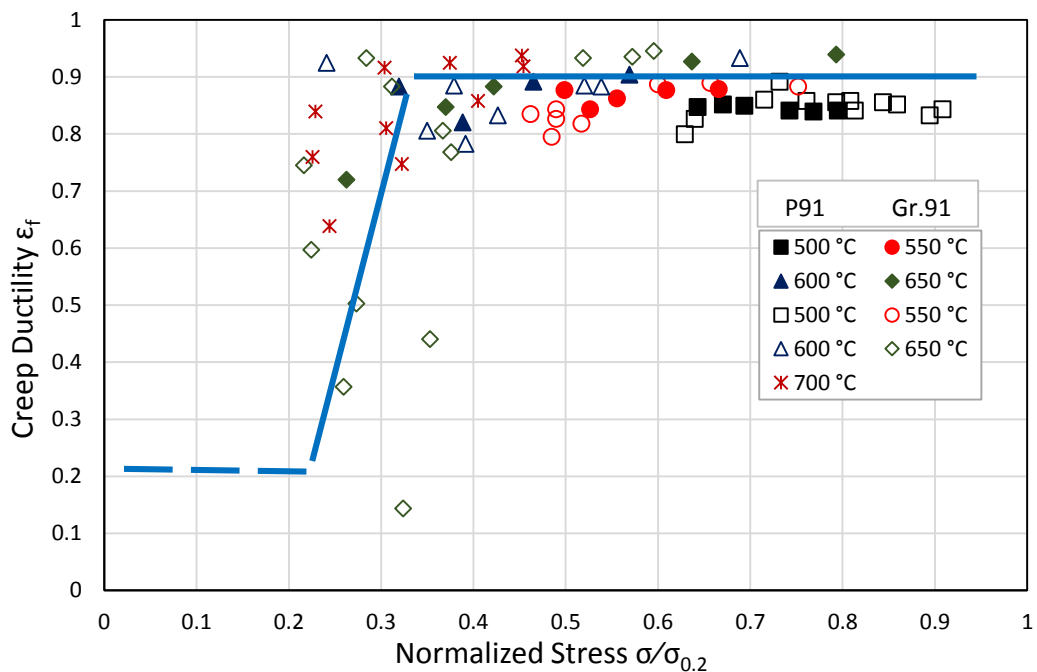


Figure 3-4 Variation of creep ductility (in terms of reduction in area) against normalized stress

Uniaxial creep tests have generated a large body of experimental data for the establishment of the basic dependence of creep ductility on some essential parameters,

such as stress/strain rate, temperature and rupture time. The multiaxial ductility factor and the stress triaxiality in Figure 3-5 show increase of the triaxiality variable, for both materials namely 9Cr-1Mo at 600 °C and Mod. 9Cr-1Mo at 650 °C. It is worthy to emphasize that the axially tensile tests on bars are only able to generate ductility data in a high stress triaxiality range ($\sigma_h/\sigma_e > 0.33$) and there is a lack of data points in the range from 0 to 0.33.

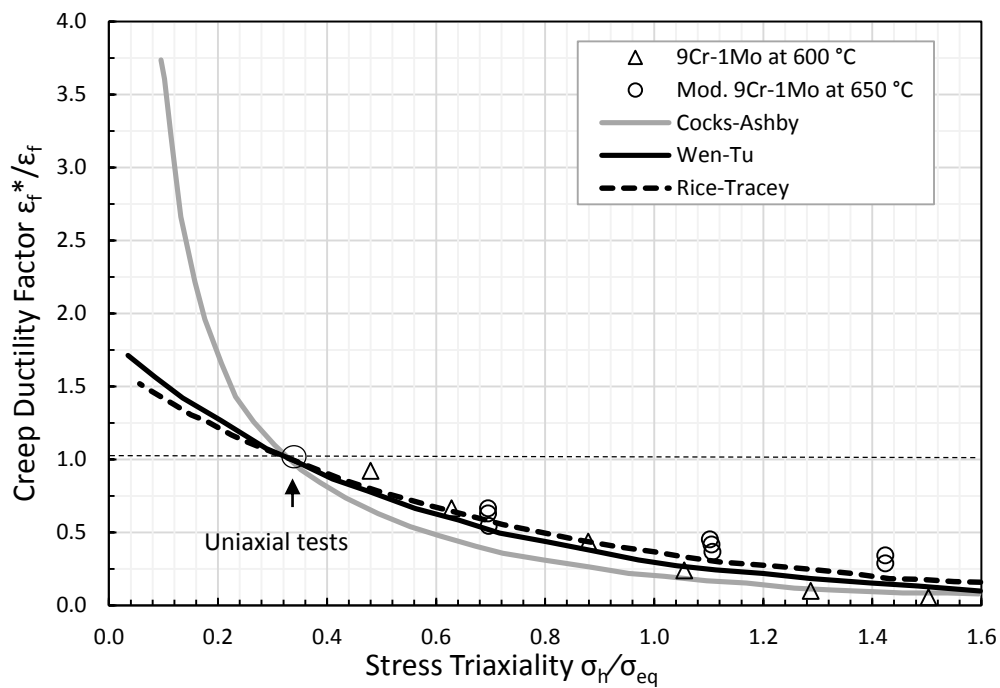


Figure 3-5 Effect of stress triaxiality on creep ductility for bar specimens at elevated temperature

3.5 Estimations of Material Constants for Damage Models

In order to predict the deformation of components which are undergoing creep, the material creep constants for the components must be known and precisely determined.

Material constants of high temperature materials change over time, especially when they are exposed to extremely high temperatures and/or stresses. Therefore, the creep properties of these materials used in the power plants. Accurate determination of material creep properties, together with appropriate material behavior models, can give a very close estimation of the components creep deformation and failure [68].

Most material constants mentioned in Section 3.3, can be obtained experimentally. The constants A and n in Norton's law are temperature dependent, together they control the secondary creep strain rate. They can be obtained by plotting the uniaxial minimum creep strain rates against the applied stresses (log-log scale). The constants B , χ and ϕ , control failure through controlling the acceleration of the tertiary creep strain rate, and they can be obtained from curve fitting to the experimental strain-time curves. The multiaxial stress state parameter α lies between 0 and 1, it determines the value of the rupture stress, by quantifying the contribution of the maximum principal stress and equivalent von Mises stress. The multiaxial stress state parameter α can be obtained by comparing the results of notched bar specimens test results and Finite Element notched bar analyses results. By modifying the α value in the FE analyses until its failure time corresponds to the experiment failure time, this α value can be taken as the correct α value for the material [69]. The material constants determined for the constitutive equations presented for models in the previous section are strictly only applicable for the stress and temperature range of the data used to obtain them and appropriate for the specific materials investigated [70]. Previous research and materials constants for damage models are reported in Table 3-1.

Table 3-1 Material constants for damage models (σ in MPa and time in hour)

Material	A	n	M	B	ϕ	χ	α	q_2
	P91 steel weldment at 650 °C [71]							

PM	1.092x10 ⁻²⁰	8.462	-4.754x10 ⁻⁴	3.537x10 ⁻¹⁷	7.346	6.789	0.313	3.2
WM	1.370x10 ⁻²⁰	7.650	-0.0361	1.600x10 ⁻²⁰	11.463	7.950	0.590	5.0
HAZ	1.300x10 ⁻²⁰	8.462	0	1.522x10 ⁻¹⁴	7.346	5.502	0.750	2.8
P92 steel weldment at 675 °C [72]								
PM	4.335x10 ⁻²⁰	7.659	0	3.377x10 ⁻¹⁷	8.3	6.459	0.383	3.0
WM	1.065x10 ⁻¹⁷	6.485	0	1.499x10 ⁻¹⁵	7.5	5.671	0.187	3.0
Inconel 718 weldment at 620 °C [73]								
PM	2.037x10 ⁻⁶¹	19.300	0	4.322x10 ⁻⁴⁷	12.0	14.728	0.1	
WM	5.260x10 ⁻⁵⁶	17.984	0	2.623x10 ⁻⁵⁰	4.0	16.367	0.2	
P91 steel weldment at 625 °C [74]								
PM	9.016x10 ⁻²⁷	10.268	0	1.258x10 ⁻²⁵	9.5	9.914	0.500	
WM	1.782x10 ⁻²⁸	10.836	0	9.519x10 ⁻²⁶	12.5	9.874	0.600	
HAZ	3.000x10 ⁻²⁶	10.268	0	1.150x10 ⁻¹⁶	9.5	5.700	0.500	
P91 steel at 650 °C and 316 stainless steel at 600 °C [75]								
P91	1.09x10 ⁻²⁰	8.462	0	2.95x10 ⁻¹⁶		6.789	0.313	3.20
SST 316	1.47x10 ⁻²⁹	10.147	0	2.73x10 ⁻³⁰		10.949	0.478	6.35

3.6 Implementation of Finite Element Method to Creep-Damage Research

The objective of creep modeling is to reflect basic features of creep in engineering structures including the development of inelastic deformations, relaxation and redistribution of stresses as well as the local reduction of material strength. A model should be able to account for material wear processes in order to predict long-term structural behavior, to estimate the in-service life-time of a component and to analyze critical zones of failure caused by creep. Structural analysis under creep conditions usually requires the following steps [56]:

1. Assumptions must be made with regard to the geometry of the structure, types of loading and heating as well as kinematical constraints.
2. A suitable structural mechanics model must be applied based on the assumptions concerning kinematics of deformations, types of internal forces (moments) and related balance equations.
3. A reliable constitutive model must be formulated to reflect time-dependent creep deformations and processes accompanying creep like hardening/recovery and damage.

4. A mathematical model of the structural behavior (initial-boundary value problem) must be formulated including the material independent equations, constitutive (evolution) equations as well as initial and boundary conditions.
5. Numerical solution procedures to solve non-linear initial-boundary value problems must be developed.
6. The verification of the applied models must be performed including the structural mechanics model, the constitutive model, the mathematical model as well as the numerical methods and algorithms.

In recent years, the finite element method (FEM) has become the widely accepted tool for structural analysis. The advantage of the FEM is the possibility to model and analyze engineering structures with complex geometries, various types of loadings and boundary conditions. Common tool finite element code ABAQUS [76], was developed to solve various problems in solid mechanics. In application to the creep analysis one should take into account that a general purpose constitutive equation which allows reflecting the whole set of creep and damaging processes in structural materials over a wide range of loading and temperature conditions is not available at present. Therefore, a specific constitutive model with selected internal state variables, special types of stress and temperature functions as well as material constants identified from available experimental data should be incorporated into the commercial finite element code by writing a user-defined material subroutine [77]. The ABAQUS finite element code is applied to the numerical analysis of creep in structures [78][18]. The standard features of the commercial FEM-based software includes only conventional creep models. Strain hardening, time hardening, and exponential models are proposed for the primary creep stage and exponential and Norton models are proposed for the secondary creep stage. Using standard creep models incorporated into FEM-based software it is impossible to model the tertiary creep stage accompanied by damage accumulation process and fracture see Figure 3-6 [Block Diagram]. In order to consider damage processes, the user-defined subroutines are developed and implemented. The subroutines serve to utilize constitutive and evolution equations with damage state variables, in addition, they allow the

postprocessing of damage, i.e. the creation of contour plots visualizing damage distributions.

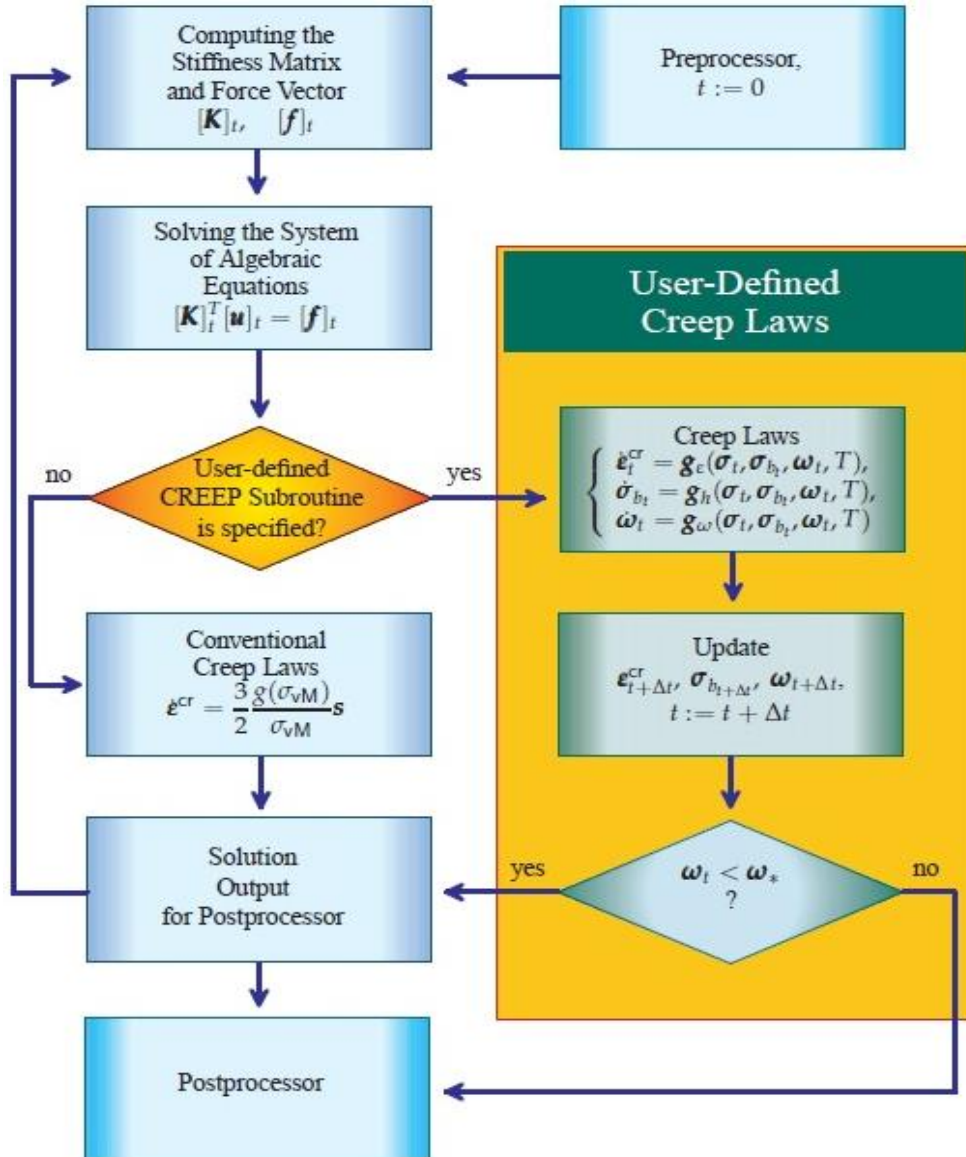


Figure 3-6 Creep analysis procedures in a commercial FEM Abaqus code with conventional creep laws and with user-defined creep-damage models [56].

4 EXPERIMENTAL INVESTIGATIONS OF CREEP BEHAVIOUR IN P91 WELDMENTS

This chapter outlines in detail the experimental procedures of creep flow and creep crack initiations and growth testing of P91 weldment material, analysis of results data reached. Uniaxial and notched bar specimens were tested to obtain the materials creep and creep rupture data for parent material (BM) and weld metal (WM). Creep data for HAZ material also obtained using tensile testing and cross-weld uniaxial. Compact tension (CT) specimens were utilized to study creep crack growth in P91 weldments. Creep and creep crack growth tests were conducted at 600°C for the P91 material. Load line displacements were recorded from testing the CT specimens and crack length monitored using the potential difference (PD) method. The load line displacement rates and the corresponding crack lengths were then used to calculate C^* , a fracture mechanics parameter used to correlate creep crack growth rates of cracks in cracked specimens of CT specimens. CT specimens were cut from the P91 BM and weldment. The initial cracks in the weldment CT specimens were located on the boundary between the BM and HAZ material, to simulate the Type IV region. Macrostructure analyses and hardness tests were carried out on some of the CT specimens to verify the correct locations of the initial cracks.

4.1 P91 Steel Weldment and Specimens

There are combinations of base, weld, and HAZ properties that need to be considered in a weldment specimen. Usually for base and weld, properties homogenous specimens cut from these regions can serve the purpose for deriving CCI and CCG properties of these regions. However, for HAZ properties which are sandwiched between the base and the weld material, the specimen has to be designed to align, as best as possible, the line of the HAZ on the crack path. Figure 4-1 (a) and (b) present the comparison for the CT specimen with weld and the standard specimen containing one material property. It is noted that regardless of where the crack path is positioned the

crack may grow through a preferred path of least resistance. Fatigue pre-cracking is recommended for introducing a starter crack if a flat and straight crack front can be continued which may reduce the time for initiation, where this may be difficult for weld materials with variations in grain size and hardness. However, an electro-discharge machined (EDM) slit can also be used as a starter crack provided the crack tip radius is 0.05 mm or less. The EDM method is particularly suitable for starter cracks in HAZ and fusion line tests [79].

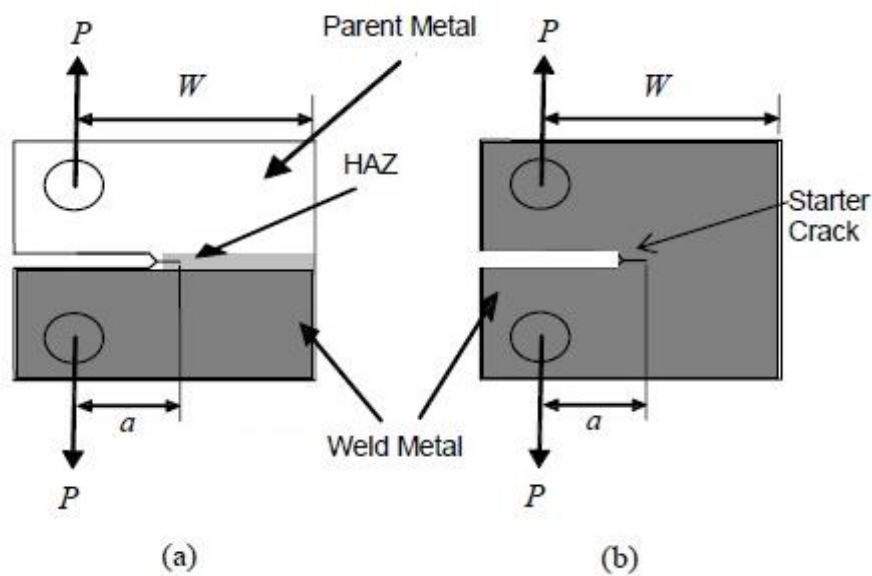


Figure 4-1 Schematic of CT specimens (a) starter crack position of HAZ
(b) starter crack position of weldment or base material regions [79].

In this study compact tension CT specimen has been used to realize the behavior of the creep crack growth in P91 material. Specimens of the tube wall and welded joints comprising three regions (weld metal, heat affected zone and base metal) were taken from the circumferential welded joint of the pipe. The chemical composition of the base metal and weld metal, welding parameters and details of the microstructural characterization are shown in Table 4-1. The compositions of elements for BM fall in the P91 material composition range.

Table 4-1 Chemical Composition of P91 Weldment [80].

Material	C	Mn	Si	P	S	Cr	Ni	Mo	V	AL	Nb	Ni + Cu
P91 BM	0.091	0.409	0.369	0.028	0.013	8.44	0.272	0.922	0.24	0.07	0	0.04
P91 WM	0.087	0.692	0.285	0.013	0.007	9.39	0.63	0.98	0.267	0	0.04	0.64

4.1.1 Similar Weldments

The experimental material is the ASTM P91 (Mod 9Cr 1Mo) steel is a newly developed high strength, high ductility martensitic steel, which attained from similar circumferential butt-welded pipes of P91 steel, which was produced by the shielded metal arc welding (SMAW) process using a suitable consumable, i.e. a 9CrMoNbV weld metal. Metallographic sample sections showed a good quality weld with refined microstructure and little evidence of coarse grains of the weld fusion line that is observed in industrial welds. The simulated HAZ materials were produced for mechanical and creep properties determination by thermal cycling in a Gleeble weld simulator machine, this simulated material had the microstructure and hardness of real HAZ weldment.

The pipes were re-heated prior to welding and Single V-type bevels was machined with one-side inclined (30°) bevel applied to ensure sufficient welding quality. The test materials were extracted welded pipes were of the dimensions 295 mm outer diameter and 58 mm wall thickness as presented in Figure 4-2.

The weldment pipes sections were then heat-treated at 760°C for two hours to relieve the welding induced residual stresses and to obtain the desired mechanical properties of weldments [80].

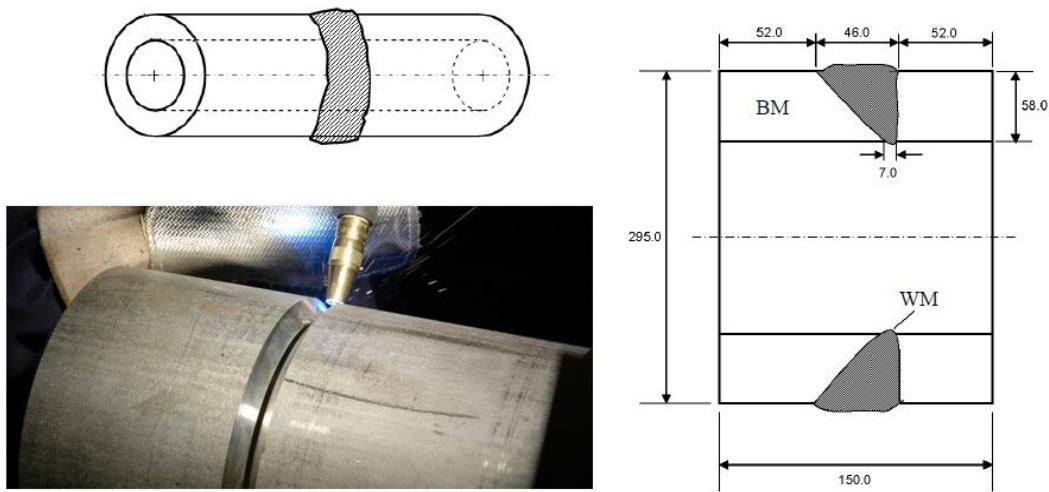


Figure 4-2 P91 Pipe circumferential weldment [80].

4.1.2 Mechanical and Creep properties

Standard tensile and uniaxial creep test specimens were machined from the welded material and from simulated HAZ materials Figure 4-3. Mechanical and uniaxial creep rupture test for P91 steel were carried out at 600 °C, which, were used to obtain creep and creep rupture data for the P91 material.

Weldment uniaxial specimens have been used to obtain creep and creep rupture data for the P91 HAZ material. The weldment uniaxial specimen has the same geometry and dimensions as the single material uniaxial specimens but it consists of BM, HAZ and WM, the results of the creep tests, carried out on the weldment uniaxial specimens, are in the form of strain-time records. The applied stresses and failure times are utilized to obtain the creep rupture data, for the HAZ material, while the applied stress and the minimum creep strain are applied to obtain the material constants A and n .

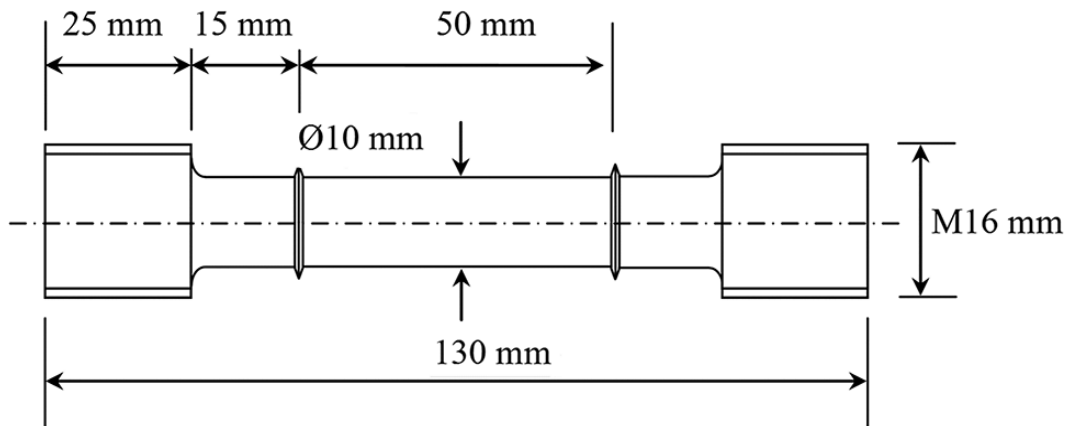


Figure 4-3 Uniaxial creep test specimen

The materials tensile and creep properties at test temperatures for P91 with BM and WM were determined as indicated in Table 4.2. Uniaxial creep testing data and values of high chromium alloy steel P91 and its weldment based on the previous research and creep data range well assorted by Dr. B. Petrovski [80].

Table 4-2 Material Data Determined in Tensile and Creep Tests

Material	$\sigma_{0.2}$ (MPa)	σ_m (MPa)	E (MPa)	D	m	A	n
				Equation (4-19)		Equation (2-45)	
P91 BM-600 °C	441	464	164	0.0018	27.73	1.57×10^{-45}	18.51
P91 WM-600 °C	362	385	125	0.0015	23.86	5.99×10^{-24}	8.55
P91 HAZ-600 °C Type IV	320	333	155	0.0016	17.38	7.16×10^{-35}	14.35
P91 HAZ-600 °C Center	293	317	139	0.0016	20.74	7.16×10^{-35}	14.09

The stress strain curves of material P91 and its weldment zones are shown in Figure 4.4, the yield strength data at test temperature of 600 °C show a decrease in WM and particularly HAZ, where the welds are undermatched in terms of strength values.

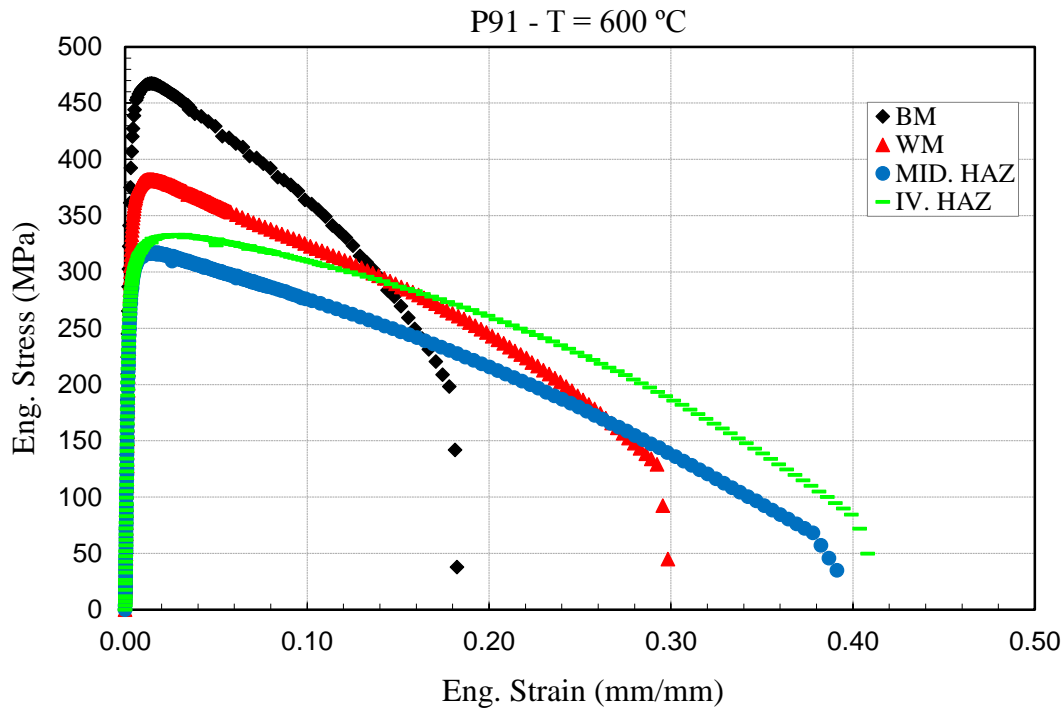


Figure 4-4 Stress-strain curves of P91 weldment tensile specimens at 600 °C

Creep rupture data for various temperatures are presented as stress versus rupture time as shown in Figure 4-5. Here straight lines were obtained for each temperature to indicate that the magnitude of the rupture strength decreases rapidly with increasing temperature, for P91 steel at 10^5 hours in a temperature range to which this material is mostly operated. Comparing Creep rupture data of parent and welded samples for various temperatures demonstrate the parent material specimens have better creep strength compared to welded ones. Here straight lines were obtained for each temperature. No change in the slope was prominent for any particular temperature implying that the creep damage mechanism remained the same. Nevertheless, the knowledge of such microstructural instabilities is important since they could lead to significant errors in extrapolation of the data to longer time [81].

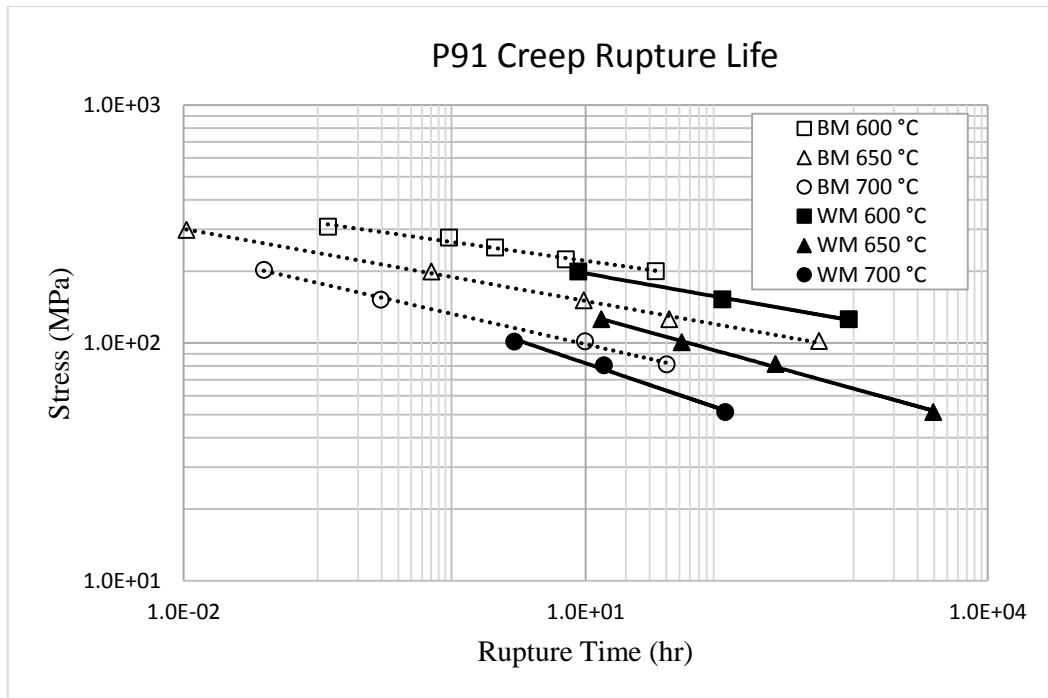


Figure 4-5 Stress and temperature dependence of creep rupture life [81].

4.1.2.1 P91 Weldments Uniaxial Creep Tests

Creep tests were carried out on uniaxial creep test specimens cut from P91 PM, WM and across the P91 weldment. These tests were carried out at a temperature of 600°C, and at stresses equivalent to the working stresses of actual P91 pipes ranging from 110 MPa to 180 MPa. One of the reasons of testing at temperatures and/or stresses higher than their working temperatures and/or stresses is to reduce the testing time, and corresponding times to failure between 350 hours and 6600 hours as presented in Figure 4-6. Creep test results for BM, WM and HAZ under various sustained loadings indicate as for the creep behavior of the three weldment zones (BM, WM, and HAZ), that creep strain was highest in weld metal and lowest for base metal. It can be seen that all of the curves exhibit relatively small primary creep and comparatively long secondary and tertiary regions, also the WM exhibits low ductility when compared to the BM and that the rupture life of the P91 BM creep specimens is about nine times higher than that of the WM and HAZ creep specimens.

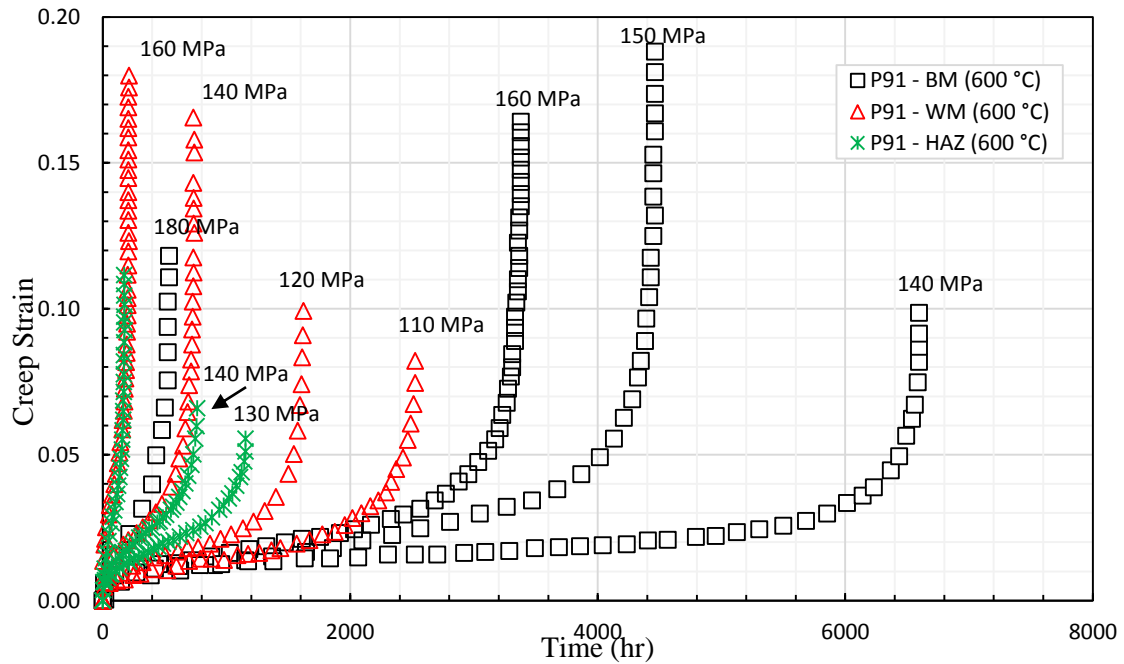


Figure 4-6 Creep test data for P91 weldment at 600 °C

4.1.2.2 Creep Test Data for Different Temperatures

The P91 steel has been also tested at somewhat higher temperatures to find the upper limit of its applicability. Results for strain vs. time, at three different temperatures, 600 °C, 625 °C and 650 °C, are given in Figure 4-7. They clearly indicate detrimental effect of temperature, limiting P91 usage to 600 °C, the only advantage of using higher testing temperature than service temperature is to decrease experimental time.

To avoid frequent inspections or monitoring creep damage required for components operating in the significant creep regime it is recommended to design for service below the No Creep temperature (T_{NC}) or the time-dependent Negligible Creep temperature (T_{NEC}). The T_{NEC} curve describes the time and temperature limits below which accumulated creep strain and damage are insignificant at a specified reference or design stress as presented in Figure 4-8 [82].

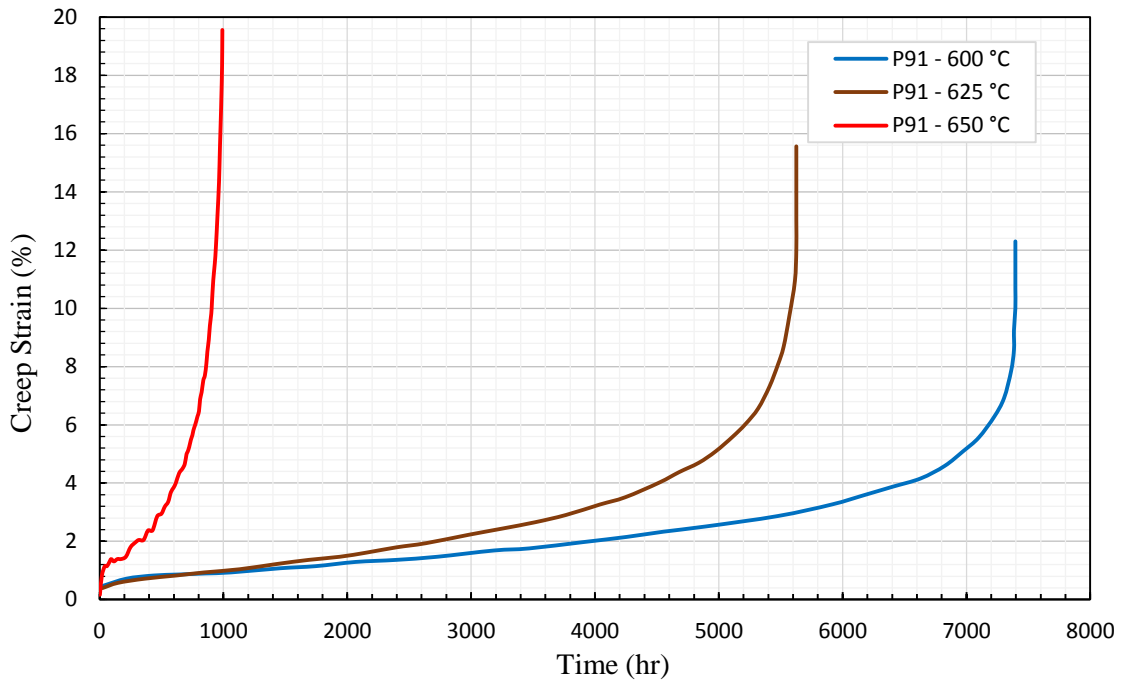


Figure 4-7 Creep strain vs. time of P91 parent material for different temperatures

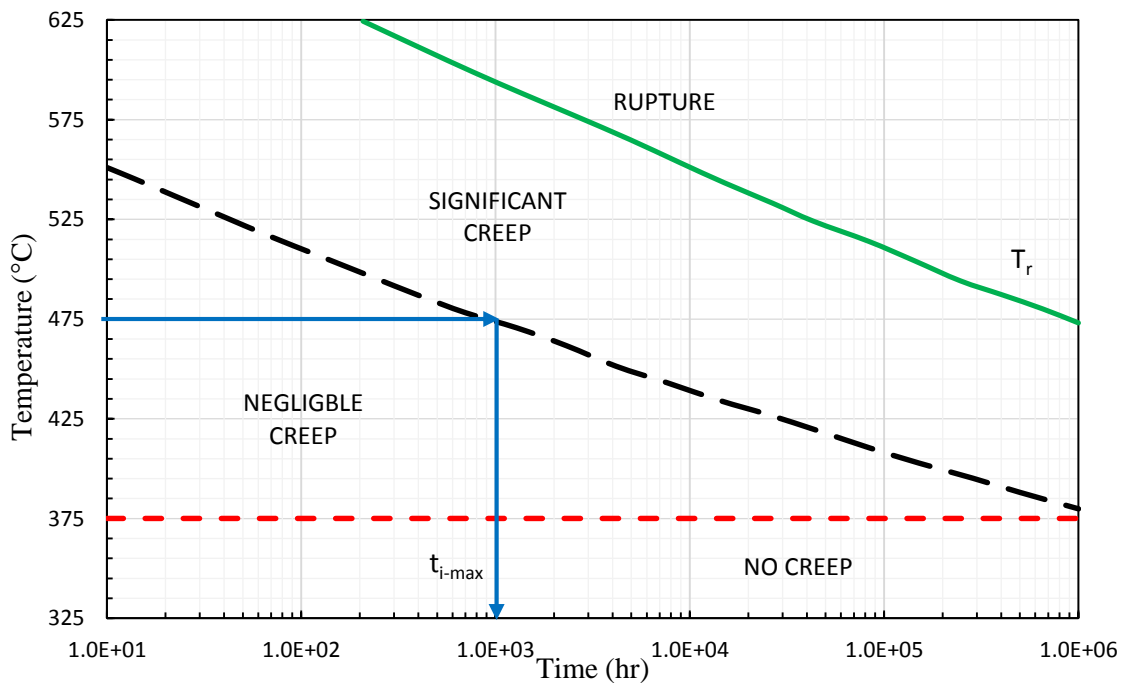


Figure 4-8 Time-temperature regions at specified reference stress [82]

4.1.3 CT Specimens

weldments contain microstructural variations and even micro-voids. Therefore, the orientation of the crack in the specimen should be chosen to be normal to the defect orientation and weaken zone, which might exist in the component being assessed. In addition the tensile and creep material properties in the direction of the orientation chosen as well as various weldment zones should be available as they will be needed for the analysis of the CCI and CCG data. The required specimen orientation, together with the volume and dimensions of available material can significantly influence the choice of specimen geometry, therefore, CT specimens were used to study creep crack growth in P91 weldments. These specimens were cut from the P91 base metal (BM) and weld metal (WM). Figure 4-9 (a) shows the geometry and dimensions of a CT specimen. These CT specimens conform to the ASTM standard [83]. The CT specimen's width, W , is a characteristic dimension of CT specimens and, in general, it should be as large as practically possible. The length is determined based on the testing facility and the availability of tested materials. W is 25 mm for all of the CT specimens tested in this study. The crack length, a is 12.5 mm, for these specimens is the distance between the loading point and the crack tip. B is 12.5 mm, the specimen's thickness and if the specimen is side grooved, then the net section thickness is B_N , in this case B_N is 10 mm as shown in Figure 4-9 (a), i.e. the depth of the groove on each side of the specimen was 10% of the specimen's original thickness (B). The side grooves are recommended by ASME E1457-15 [3], which, specifies the groove depth to be 10% of the specimen's original thickness to ensure that a straight crack front is produced, Electric Discharge Machining (EDM), also known as wire erosion machining, was used to cut the initial cracks. The wire diameter, 0.25 mm, was the smallest size available. This method enabled the initial crack length and position to be accurately defined prior to the test beginning.

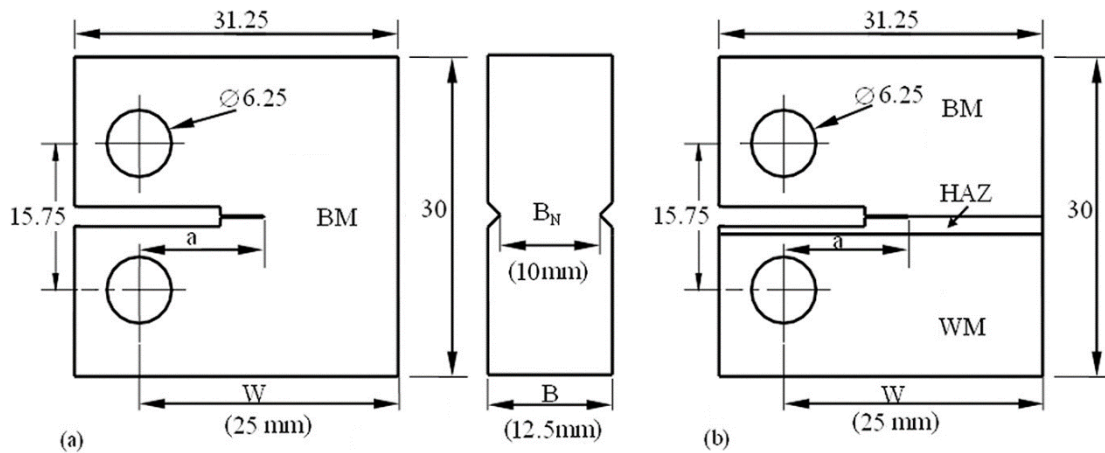


Figure 4-9 Specifications and dimensions of CT specimens (a) Base metal specimen and side groove (b) Cross weld specimen consist of BM, WM and HAZ

P91 BM and WM CT specimens were cut from a P91 weldment. The P91 BM CT specimens were cut from the BM side of the P91 weldment, while the WM specimens were cut across the weld. Therefore, the WM CT specimens consist of BM, HAZ material, and WM. The weldment CT specimens were cut so that the initial cracks were located, as far as practically possible, on the PM/HAZ boundary, i.e. in the Type IV region. In order to accurately position the initial cracks, the cross-weld CT specimens were, firstly, polished and etched to show the PM/HAZ boundary then wire erosion machining was used to cut the initial cracks, Figure 4-9 (b) shows the geometry and dimensions of the cross-weld CT specimens. All of the P91 cross-weld CT specimens were fully side grooved. Figure 4-10 (b) shows a schematic drawing of the P91 weldment and the sampling position for the cross-weld CT specimens of a welded pipe.

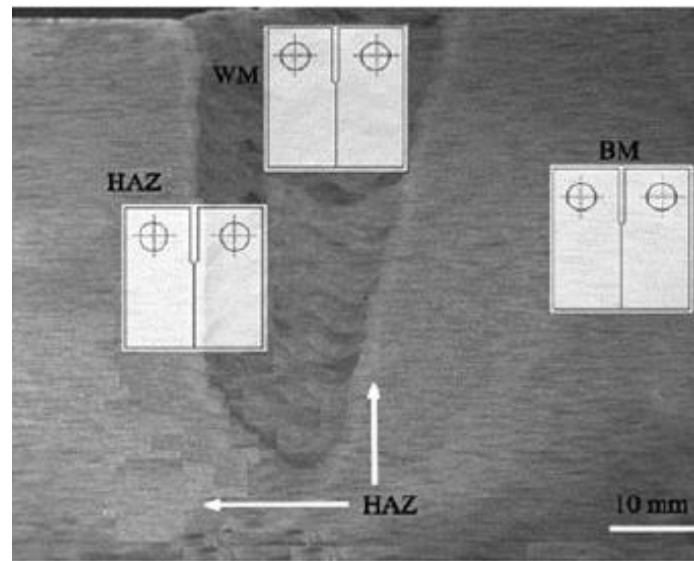


Figure 4-10 Compact tension specimens extracting from P91 steel welded joint. WM, BM and HAZ [5].

Experimental determination and analysis of Creep Crack Initiation (CCI) and Creep Crack Growth (CCG) rate data of weldments including Base Metal (BM), Heat Affected Zone (HAZ) and Weld Metals (WM). CCI is defined as the extension of a pre-existing defect by a small amount of growth, typically 0.2 mm or 0.5 mm [79].

4.2 Creep Crack Growth Behavior of P91 Weldments

Failures due to creep can be classified either as resulting from widespread creep damage or resulting from localized creep damage. The components of first case are typically subjected to uniform temperatures and stress during service, such as thin-wall pipes. Their life can be estimated from creep rupture data, engineers have used that approach for several decades. However, high temperature components of second case are subjected to stress and temperature gradients and do not fail by creep rupture. It is more likely that at the end of the predicted creep rupture life, a crack develops at a high stress location, which propagates and ultimately causes failure. Failure can also result from pre-existing defects on the material, in which case the entire lifetime of the component is consumed with crack propagation. Creep rupture data can only take so much into consideration, and it is

therefore important to develop the capability to predict crack propagation life at elevated temperatures in the presence of creep deformation [84].

The creep data focus on the microstructural variation and especially to the effect of stress level on the creep deformation. The yield strength of WM and particularly in the HAZ (center) is lower than that of the BM, therefore, the welds are undermatched in terms of yield strength. The creep data directs attention to the microstructural variation and especially the effect of stress level on the creep deformation. However, the creep resistance of material rather than the yield strength determine the crack growth behavior under creep conditions, as presented in Figure 4-11. Constant load creep tests were performed for P91 at 600 °C, with various stress levels ranging from 145 to 160 MPa, 110 to 145 MPa and 100 to 145 MPa for BM, WM and HAZ, respectively and presented in Table 4-3:

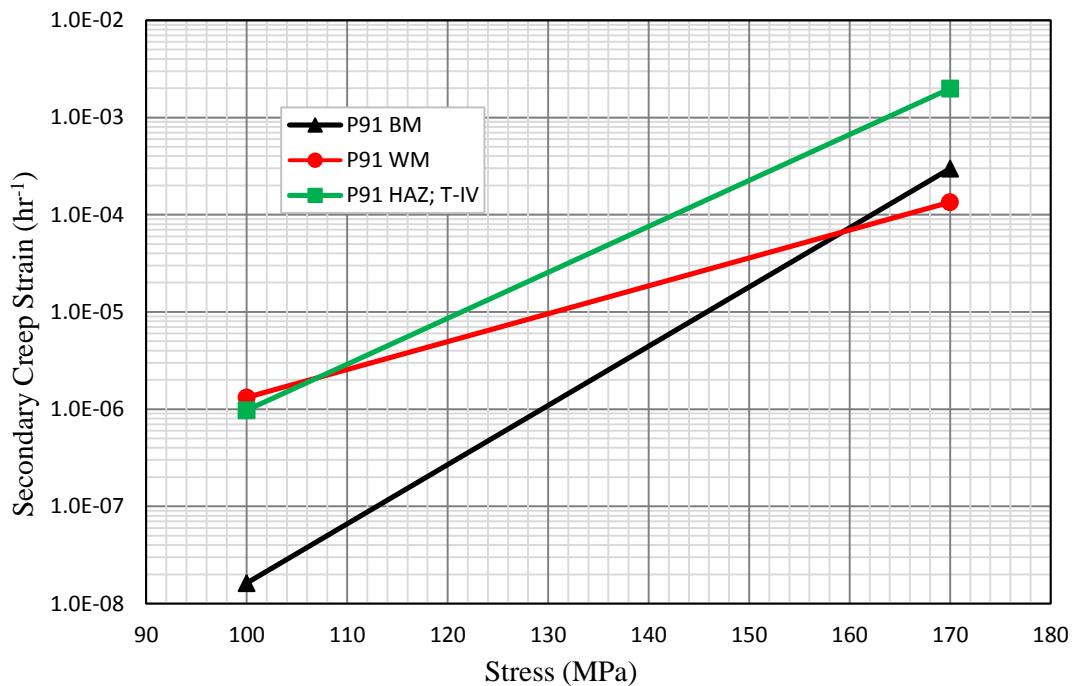


Figure 4-11 Steady state Creep rates as a function of stress for P91 weldment at 600 °C

Table 4-3 Steady-state creep rate as a function of stress of P91 weldments at 600 °C

STRESS (MPa)	BM	WM	HAZ; T-IV	WM/BM	IV/BM
100	1.622E-08	1.321E-06	9.773E-07	81.396	60.239
110	9.467E-08	3.029E-06	3.836E-06	31.999	40.524
120	4.738E-07	6.465E-06	1.337E-05	13.645	28.218
130	2.084E-06	1.298E-05	4.216E-05	6.229	20.228
140	8.215E-06	2.476E-05	1.221E-04	3.014	14.862
150	2.945E-05	4.516E-05	3.285E-04	1.533	11.154
160	9.725E-05	7.925E-05	8.294E-04	0.815	8.528
170	2.986E-04	1.344E-04	1.979E-03	0.450	6.628

In Figure 4-12, the minimum creep strain rates are plotted against the applied stress of P91 weldment zones, by inspection of curves the BM and WM exhibit better creep resistance than HAZ which also under go higher minimum creep rates with increasing applied stresses. The minimum creep rates are proportional to applied stress up to about 150 MPa for BM and WM. From test data, constants for power-law creep can be fitted, as shown in Figure 4-12 for all three weldment zones, as given by the following Equation (4-1)

Base metal	$\dot{\epsilon}_{2c} = 1.568 \times 10^{-45} \sigma^{18.507}$	
Weld metal	$\dot{\epsilon}_{2c} = 9.73 \times 10^{-24} \sigma^{8.553}$	(4-1)
Heat-affected zone	$\dot{\epsilon}_{2c} = 1.968 \times 10^{-35} \sigma^{14.348}$	

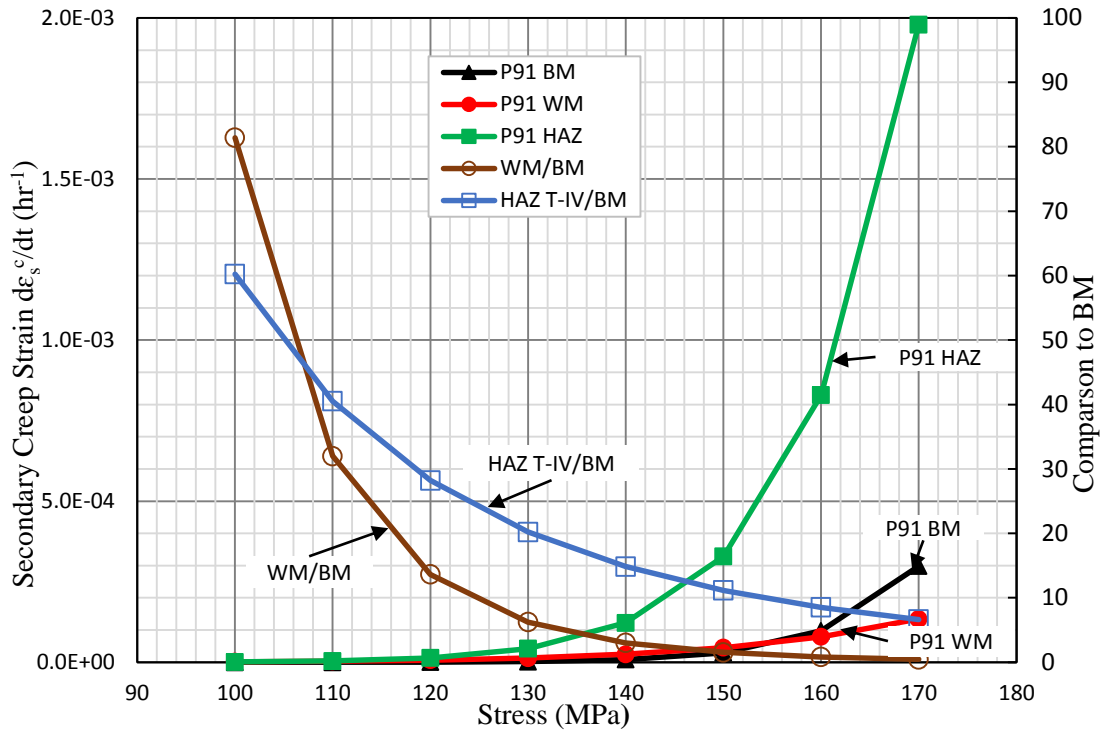


Figure 4-12 Comparison of creep rate of weldments versus stress

4.2.1 The DCPD method of Crack Length Measuring

The Direct Current Potential Drop (DCPD) method utilizes the fact that the electrical resistance of a CT specimen change with crack growth. By applying a constant current over the specimen and measuring the resulting voltage over the crack, the crack length can be related to the voltage and the difference in crack length with difference in voltage. A constant DC supply, a voltmeter, current input wires and voltage pick-up wires summarize the equipment utilized in a DCPD system, presented in Figure 4-13 a basic schematic drawing of a DCPD system [85]. The placements of the DC supply wires and the voltage pick-up wires were determined using ASTM standard recommendations [3].

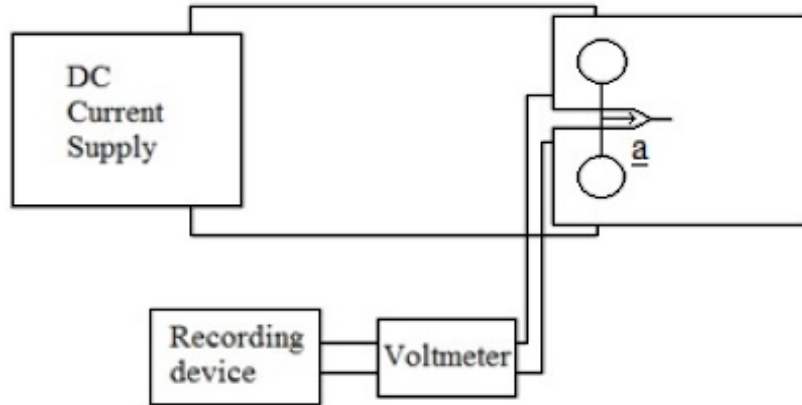


Figure 4-13 DCPD system including a CT specimen

High temperature fracture mechanics tests on the weldments of P91 steel at 600 °C including the weldment zones of BM, WM and HAZ, various specimens were used to insure consistency in CCI and CCG data, all tests are carried out under constant load. Details of the conducted tests are given in Table 4-4 of P91steel weldments, for constant loading and at T= 600 °C.

Table 4-4 Details of the test conditions for the BM, WM and HAZ of P91steel at 600 °C

Sl. No.	Specimen	Duration (hr)	Load (N)	K (MPa.m ^{0.5})	C* (N/mm/hr)	a ₀ (mm)	a _r (mm)	Δa (mm)
1	CT25-BM	1542.9	3300	19.52	0.014	13.243	14.771	1.828
2	CT25-BM	766.8	3800	22.56	0.056	13.211	14.373	1.528
3	CT25-BM	742.7	3600	21.70	0.198	13.231	14.200	1.162
4	CT25-WM	410.6	3800	19.33	0.055	11.880	13.618	1.738
5	CT25-WM	365.2	3800	19.33	0.085	11.920	14.682	2.762
6	CT25-WM	367.6	3800	19.10	0.095	11.993	14.434	2.441
7	CT25-WM	1463.2	3100	16.31	0.011	12.210	16.178	3.968
8	CT25-WM	1153.1	3100	16.57	0.011	12.426	16.666	4.240
9	CT25-WM	2141.2	3300	13.04	0.007	11.927	17.422	5.495
10	CT25-HAZ	1792.6	3100	16.35	0.008	12.210	14.880	2.670
11	CT25-HAZ	750.1	3600	19.05	0.013	12.223	12.470	0.247
12	CT25-HAZ	2860.9	3100	15.79	0.003	11.870	13.069	1.199
13	CT25-HAZ	4852.5	2600	13.68	0.004	10.692	16.067	4.075

The temperature, load, potential drop (PD), load line displacement (V_{LLD}) and crack tip opening displacement (δ_{CTOD}) data are monitored and recorded instantaneously starting

from pre-load to full load for the subsequent analysis of the data for crack size and crack tip parameters C^* and K determination. The data acquired from CT specimens of P91 BM, WM and HAZ tested for 4850 hours at 600 °C is shown in Table 4-5. The tests are terminated as soon as both the potential drop and the displacement measurements show acceleration in crack growth rates and displacement rates, indicating that final failure of the specimen is pending.

Table 4-5 The data attained from CT specimens of P91 weldment tests

Material	Specimen	W (mm)	B (mm)	B _n (mm)	a ₀ (mm)	a _c (mm)	
P91-WM	W003	25.000	12.530	10.050	11.993	14.434	
E (MPa)	σ _y (MPa)	P(N)	U ₀ (mV)	T (°C)	v	Y ₀ (mm)	
125000	362	3081.00	1028.60	600.000	0.330	3.0	
D		m	A	n	Equation 4-1	Equation 4-2	
0.0015		23.86	5.990E-24	8.55			
Time (h)	U _t (mV)	F (N)	V _{LLD} (mm)	δ _{CDOM} (mm)	a (mm)	a _{cor} (mm)	Δa (mm)
0.0	1028.6	3078.1	0.000	0.002	11.993	11.993	0.000
191.3	1030.4	2981.9	0.044	0.015	12.011	12.018	0.025
233.1	1032.2	2981.9	0.053	0.019	12.029	12.043	0.050
266.8	1034.1	3126.2	0.059	0.021	12.047	12.068	0.075
297.2	1035.9	3030.0	0.065	0.023	12.065	12.093	0.100
326.0	1037.8	3078.1	0.070	0.025	12.084	12.118	0.125
353.7	1039.6	3030.0	0.074	0.027	12.102	12.143	0.150
381.4	1041.5	3078.1	0.079	0.028	12.120	12.168	0.175
409.1	1043.3	3078.1	0.084	0.030	12.138	12.193	0.200
437.9	1045.1	3078.1	0.088	0.031	12.156	12.218	0.225
468.0	1047.0	2933.8	0.093	0.033	12.174	12.243	0.250
499.2	1048.8	3078.1	0.098	0.034	12.192	12.268	0.275
532.6	1050.7	3078.1	0.104	0.036	12.211	12.293	0.300
566.5	1052.5	3078.1	0.110	0.038	12.229	12.318	0.325
601.5	1054.4	3030.0	0.116	0.041	12.247	12.343	0.350

An accurate measurement of the initial a_0 and final a_f crack size were made when the specimen were broken open outside the furnace after testing. The final measured crack length may be used to calibrate the crack lengths obtained from potential data using Johnson’s formula given for CT geometry [86]

$$a = \frac{2W}{\pi} \cos^{-1} \left[\frac{\cosh(\pi Y_0/2W)}{\cosh[(U_t/U_0) \cosh^{-1}(\cosh(\pi Y_0/2W)/\cos(\pi a_0/2W))]} \right] \quad (4-2)$$

Where a_0 is initial crack size with reference to voltage U_0 , Y_0 equal the half distance between the output voltage leads and U_t is the actual value of the potential.

4.2.1.1 Test Procedures

The high temperature experimental set-up designed for high temperature crack growth studies is presented in Figure 4-14. All creep tests performed on standard dead weight, lever creep test rigs and work in a similar manner even if the individual design varies. The system facilitates testing under constant load, the test setup comprises of an insulated furnace of a split type opening to allow for specimen installation and to keep the temperature stable during the test. The specimen is placed inside the furnace and preloaded with the empty lever arm, yielding a load of approximately 100 N, thermocouples are tied to the gauge length and the specimen is heated to test temperature. The thermocouples, known as type S (Pt/PtRd wires) are made from certified metals and new metal is used for the thermal junction for each new test. After a soaking time of at least 2 h during which the temperature gradient is adjusted and minimized, the previously calibrated weights are loaded onto the lever arm and the test started. The maximum tolerances allowed are ± 1 °C for temperature stability and the load is applied within 2 minutes.



Figure 4-14 High temperature experimental set-up

4.2.1.2 Load Line Displacement

Load line displacement curves, obtained from the P91 weldment CT specimens, are shown in Figure 4-15. BM specimen was initially loaded by 3300 N applied for about 1500 hours, a sudden increase in displacement near 1000 hours. WM specimen was loaded by 3080 N applied for about 2100 hours, a small gradual increase in displacement until rupture. HAZ specimen was loaded by 3600 N applied for about 5000 hours, a small gradual increase in displacement until rupture, which followed the pattern of WM behavior for more time duration to show the characteristic of material structure of HAZ.

Test durations of the plotted CT specimens vary between 60 to 5000 hours. A longer crack growth Δa , with shorter load line displacement V_{LLD} , observed in WM specimens. A comparison between BM and HAZ specimens tests reveal that a longer Δa , can be obtained for a shorter V_{LLD} in creep-weaker weldment zone tests.

These data were used to calculate the displacement rates, specimens of P91 weldments were tested until well into tertiary regime (i.e. creep crack growth acceleration region). This resulted in very large displacements in BM specimens at which point they include significant plastic deformation near the end of the test. Tests for WM and HAZ specimens, were stopped near the beginning of tertiary region in order to ensure that the resulting displacements, and the corresponding crack growth, are predominantly due to creep ones.

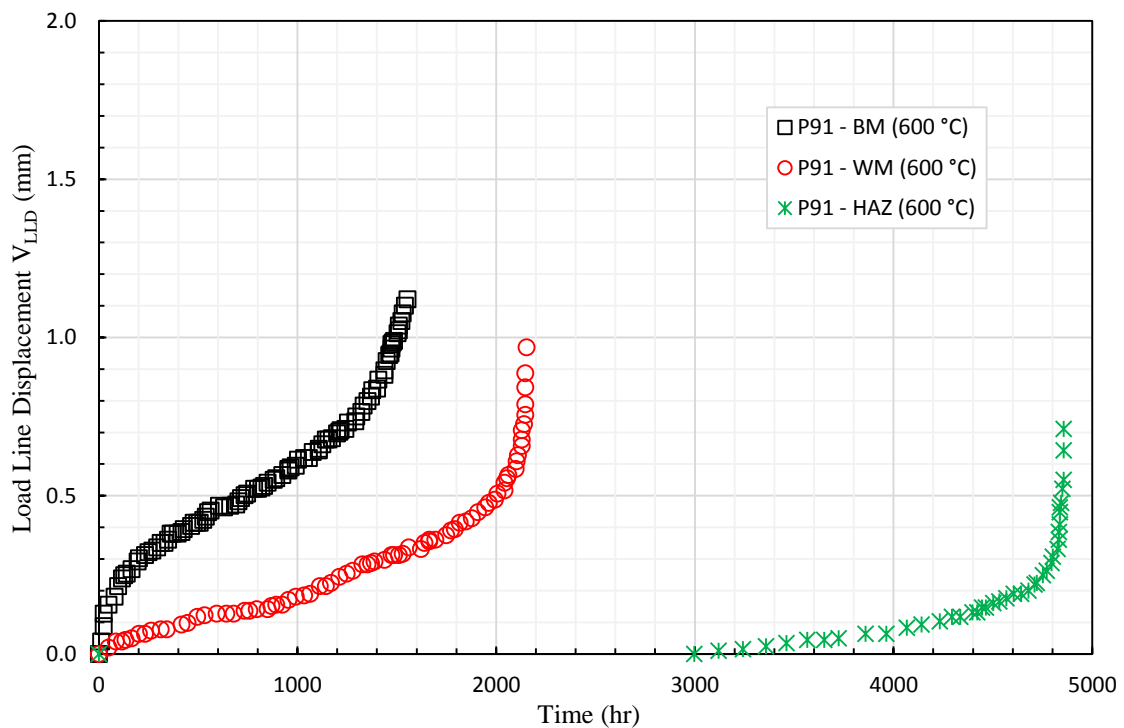


Figure 4-15 Load Line Displacement of P91 weldment at 600 °C

4.2.1.3 Crack Length

On completion of the creep crack growth tests, CT specimens were subjected to fatigue loading to break the remaining ligament and measure final creep crack extension and to measure the crack surfaces. Once the initial and final crack size a_0 , a_f respectively are available, a correction to all data between size a_0 and a_f must be done by linear interpolation using:

$$a_{cor} = \left[(a - a_0) \left(\frac{a_f - a_{max}}{a_{max} - a_0} \right) \right] + a_0 \quad (4-3)$$

Where a_{max} is the maximum value determined by Equation (4-2), a_0 is the initial crack length (a_0 is 12.5 mm in all of the CT specimens used in our creep tests), Δa is the overall increment of crack length as measured by following relation

$$\Delta a = (a - a_0) \left(1 + \frac{a_f - a_{max}}{a_{max} - a_0} \right) \quad (4-4)$$

Creep crack growth curves for the P91 weldments CT specimens tested at 600°C are presented in Figure 4-16. Data included in these curves were used to calculate the creep crack growth rates and the C^* values, and for validating the finite elements damage predictions. Comparing the creep crack growth for P91 steel weldment it can be seen that larger Δa can be obtained in creep weak weldment regions relative to base metal and the gradual increase in the crack length with time while it is faster in weld metal and heat affected zone [87].

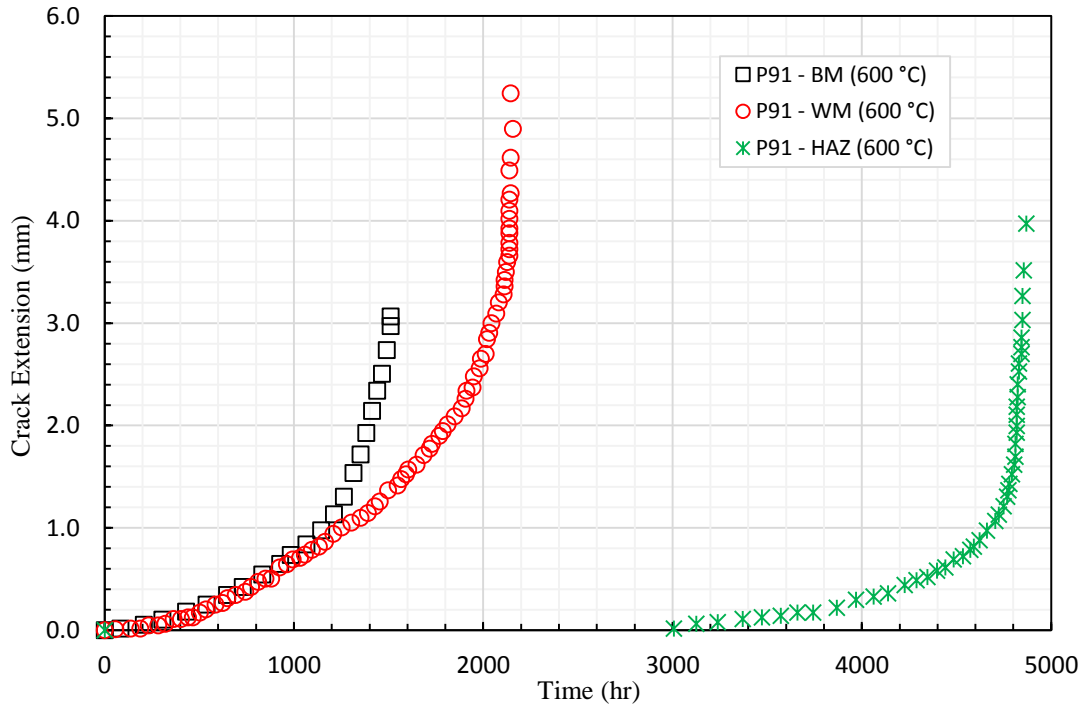


Figure 4-16 Crack extension comparison of P91 weldment at 600 °C [87]

4.2.2 Validity of Test Results

The validation of the test results are based on extensive evaluation of the data, the experimental data are analyzed and correlated with pre-determined crack tip parameters. Validity criteria are specified in ASTM E1457-15 [3], for the use of C^* as a correlating parameter for CCG data determined by testing C(T) specimens.

- The data are valid for further evaluation if

$$0.85 \leq \frac{\Delta a_{pf}}{a_f - a_o} \leq 1.15 \quad (4-5)$$

If the Equation (4-5) was not satisfied, the difference between the predicted and calculated crack growth was noted and data processed further. Due to crack front irregularities and crack grooving, the crack length values determined on fracture surfaces may vary from the calculated ones using DCPD. It mainly depends on the way the crack length measurement was made on the fracture surface.

- Only data points that exceed the transition time, t_T , were considered. The transition time, for plane strain conditions is estimated as follows:

$$t_T = \frac{K^2(1 - \nu^2)}{E(n - 1)C^*} \quad (4-6)$$

where ν is the Poisson's ratio, E is the modulus of elasticity, n is the creep exponent in Norton's creep law, C^* and K are the C^* -parameter and stress intensity factor, respectively, and K is given by :

$$K = \frac{P}{(BB_N)^{1/2}W^{1/2}} \frac{2 + a/W}{(1 - a/W)^{3/2}} f(a/w) \quad (4-7)$$

and

$$f(a/w) = 0.866 + 4.64(a/W) - 13.32(a/W)^2 + 14.72(a/W)^3 - 5.6(a/W)^4 \quad (4-8)$$

where P is the applied load, a is the instant crack length, W is the specimens width, B is the CT specimen full thickness, i.e. without side grooves, B_N is the CT specimen net thickness, i.e. with side grooves.

- Data points prior the first 0.2mm crack growth has been excluded. Time for this 0.2mm increase in crack length is known as the crack initiation time.
- Ductility condition for creep process is met by $\dot{V}_c/\dot{V}_t > 0.5$, where \dot{V}_c is the creep component of the load line displacement rate and \dot{V}_t is the total load line displacement rate. For all of the creep tests conducted for our study, it was found that values range from 0.832 to 0.989 at all durations for P91 weldments experiments at 600 °C.

These criteria were applied to all of the creep crack growth tests conducted on the P91 specimens. The Secant method has been used to obtain the creep crack growth rates and the corresponding load line displacement rates, by calculating the slope of a straight line connecting every two consecutive points was taken as the rate at an average point, which lies in between these two points.

$$\left(\frac{da}{dt}\right)_{\bar{a}} = \frac{a_{i+1} - a_i}{t_{i+1} - t_i} \quad (4-9)$$

$$\left(\frac{dV}{dt}\right)_{\bar{a}} = \frac{V_{i+1} - V_i}{t_{i+1} - t_i} \quad (4-10)$$

And

$$\bar{a} = \frac{a_{i+1} - a_i}{2} \quad (4-11)$$

The crack growth rate, da/dt , as a function of crack extension Δa of weldment CT specimens, tested at 600 °C, shows two stages of crack growth, as presented in Figure 4-17. Lower crack growth rate following the crack growth initiation extends to $\Delta a = 1.5$ mm, crack growth in stage I. Higher crack growth rate is observed in stage II where the CCG rate is plotted because the creep crack tends to grow towards the softer zone. In addition, the region adjacent to the HAZ/BM interface have low values of mechanical and creep strength [5].

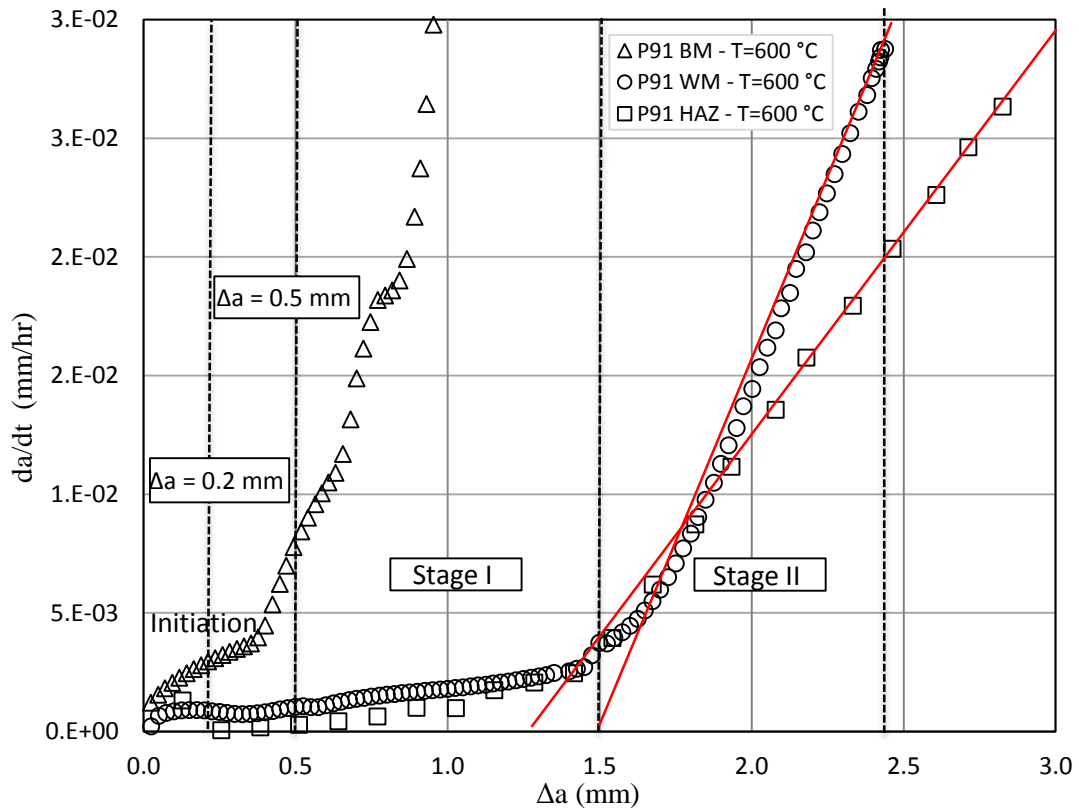


Figure 4-17 Crack growth rate versus crack extension of P91 weldment [5]

A typical representation of the creep crack propagation path for the CT specimen can be realized in Figure 4-18. It can be clearly seen that the creep crack grows towards the boundary between the HAZ and BM. The creep and CCG in P91 welds indicate that failure in CT specimens occurs in the fine-grained HAZ region close to the BM, even if the initial cracks were located in the middle of the HAZ region, they deviated and grew into the type IV region [88]. The test results data are correlated to assess the CCG behavior of P91 weld material.

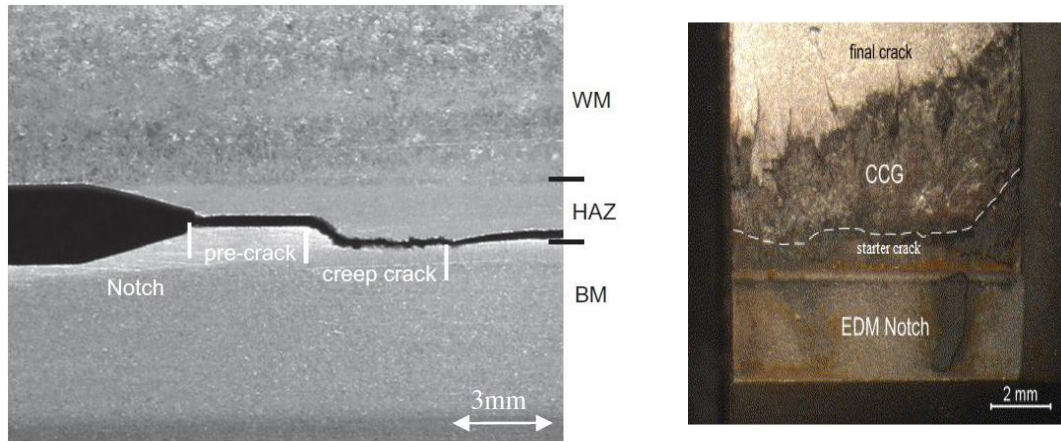


Figure 4-18 Creep crack growth in a welded joint [5]

4.3 Creep Crack Initiation in P91 Weldment

The experimental determination of creep crack initiation on specimens of P91 steel and weldments are investigated, in an attempt to define creep crack initiation using fracture mechanics test data. CCI is defined by a technical creep crack initiation length $\Delta a_i = a_i - a_0$, or for CT specimens $a_i = 0.004W$.

4.3.1 Initial Creep Crack Growth Rates

Models to estimate CCI times can be based on the time for a slowly growing crack to propagate a certain distance (typically 0.2 mm or 0.5 mm). On initial loading, transient conditions exist, during which the damage distribution ahead of the crack tip builds up to a steady state. Prior to steady-state conditions being achieved, the crack growth rate is often less than the steady-state value and it may be shown that the initial creep crack growth rate \dot{a}_0 , may be in the order of $1/(n + 1)$ times slower than the steady state CCG rate [89].

Thus, from the NSW model Equation (2-72) the initial creep crack growth rate may be approximated as

$$\dot{a}_{NSW} \approx \frac{\dot{a}_{NSW}}{n+1} = \frac{3C^{*0.85}}{(n+1)\varepsilon_f^*} \quad (4-12)$$

Similarly, if the modified NSW model Equation (2-73) is used,

$$\dot{a}_{NSW-MOD} \approx \frac{\dot{a}_{NSW-MOD}}{n+1} = (Ar_c)^{\frac{1}{n+1}} \left[\frac{C^*}{I_n} \right]^{\frac{n}{n+1}} \frac{\bar{h}_n}{\varepsilon_f} \quad (4-13)$$

4.3.2 Creep Crack Initiation Time Predictions

If the minimum crack extension that can be measured reliably is Δa and assuming that CCG rate is constant during the increment of crack growth Δa , then, the initiation time, t_i , may be estimated as [90]

$$t_i = \frac{\Delta a}{\dot{a}} \quad (4-14)$$

where \dot{a} in Equation (4-14) refers to a general CCG rate. By substituting an appropriate value of the initial crack growth rate \dot{a}_0 , Equations (4-17) and (4-18) into Equation (4-19), an upper bound estimate of the initiation time may be obtained. A lower bound initiation time prediction is obtained from the steady state crack growth rate Equations (2-72) and (2-73). The NSW model thus indicates that

$$\frac{\Delta a \varepsilon_f^*}{3C^{*0.85}} \leq t_i \leq \frac{\Delta a (n+1) \varepsilon_f^*}{3C^{*0.85}} \quad (4-15)$$

and similarly from the NSW-MOD model

$$\frac{\Delta a}{(n+1)(Ar_c)^{\frac{1}{n+1}} \left[\frac{C^*}{I_n} \right]^{\frac{n}{n+1}} \frac{\varepsilon_f}{\bar{h}_n}} \leq t_i \leq \frac{\Delta a}{(Ar_c)^{\frac{1}{n+1}} \left[\frac{C^*}{I_n} \right]^{\frac{n}{n+1}} \frac{\bar{h}_n}{\varepsilon_f}} \quad (4-16)$$

Equations (4-15) and (4-16) also depend on the assumption of plane stress or plane strain. The shortest (lower bound, most conservative) initiation time prediction is obtained from using the steady state NSW or NSW-MOD model under plane strain conditions. An upper

bound initiation time prediction is obtained by using the initial crack growth rate NSW or NSW-MOD model under plane stress conditions.

The C^* correlation with crack initiation times for $\Delta a=0.2$ and $\Delta a=0.5$ mm crack extension are presented in Figure 4-19 and Figure 4-20, respectively. P91 WM has the lowest crack initiation resistance. However, the P91 HAZ has the highest crack initiation resistance with longer initiation time. For the crack initiation defined at $\Delta a=0.2$ mm Figure 4-19, the decrease of crack initiation resistance with increasing crack initiation time t_i is the lowest for P91 BM. Note that the crack initiation data at $\Delta a=0.2$ mm crack extension has higher scatter than that at $\Delta a=0.5$ mm crack extension as evidently seen in Figure 4-20.

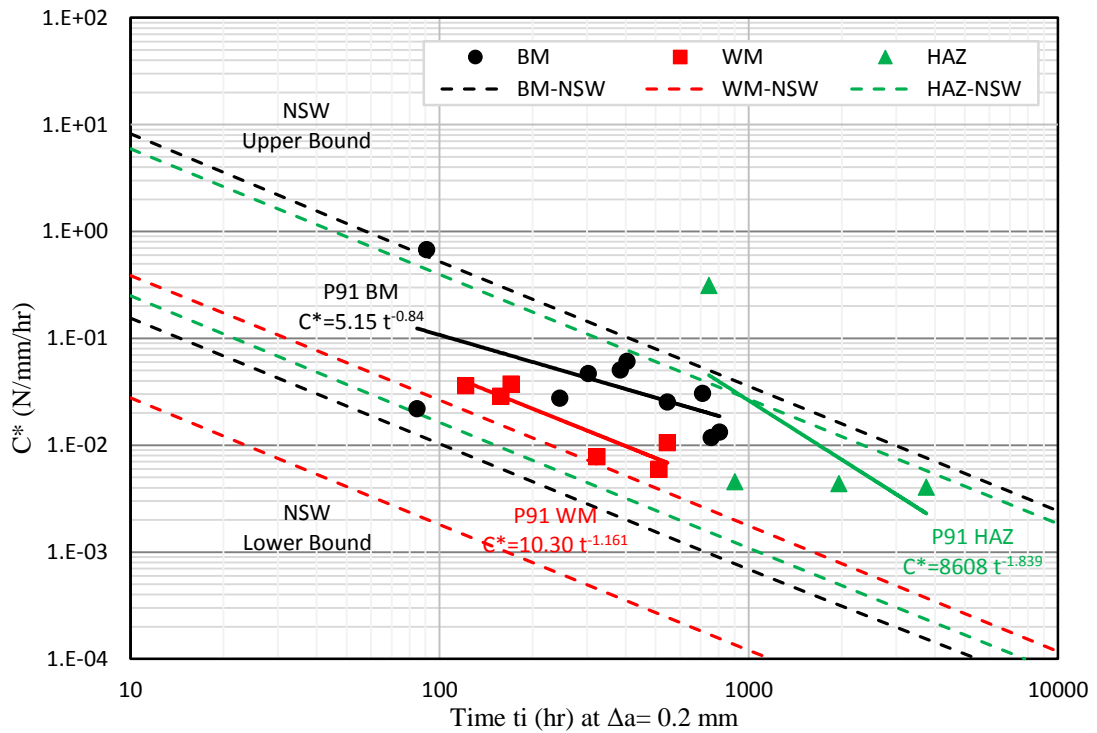


Figure 4-19 Creep crack initiation resistance of P91 weldment with NSW bounds at $\Delta a = 0.2$ mm

The upper and lower bound NSW model prediction lines determined using Equation (4-15) are plotted for different weldment zones of P91. The experimental P91 WM data lie closer to the upper bound prediction lines for both crack initiation at $\Delta a=0.2$ mm and $\Delta a=0.5$ mm crack extension as in Figure 4-19 and Figure 4-20 respectively. Therefore, the NSW model predicts conservative crack initiation time for P91 WM. The experimental data, which lie above the upper bound NSW prediction line, is directing attention to the need for more experimental data to verify NSW model predictions.

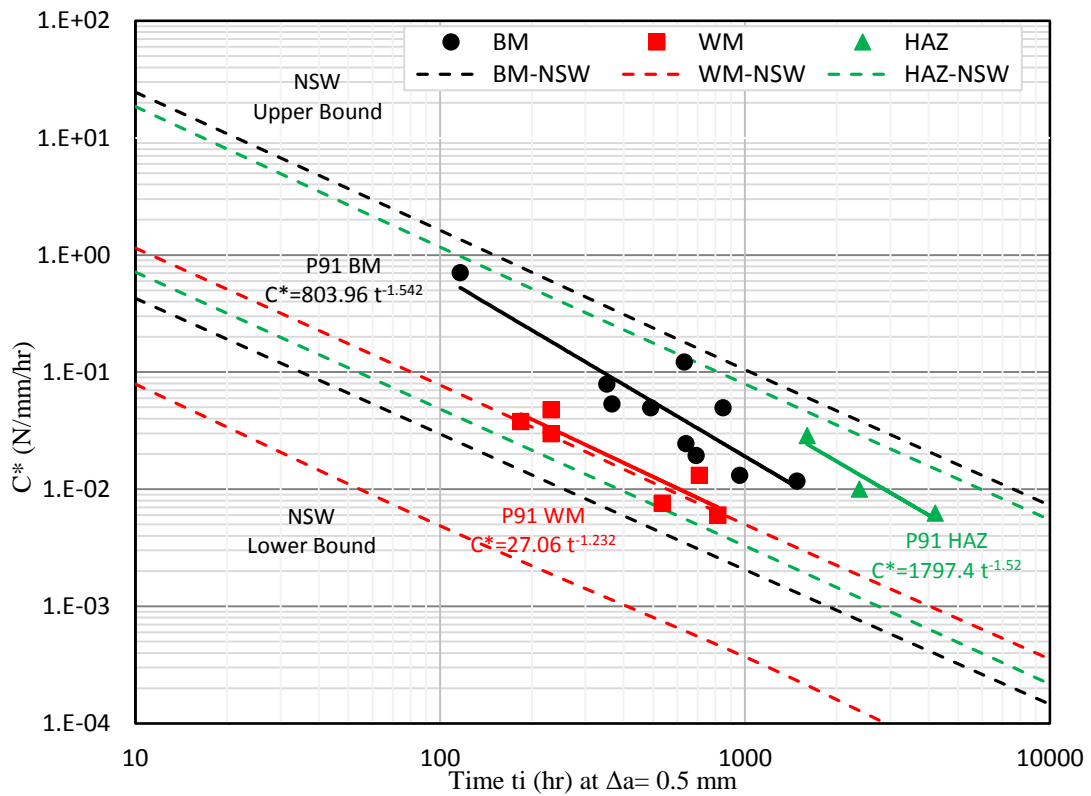


Figure 4-20 Creep crack initiation resistance of P91 weldment with NSW bounds at $\Delta a = 0.5$ mm

4.3.3 The Behavior of Creep Crack Initiation

The behavior of components under creep loading conditions is described by load line displacement versus time diagrams. On application of steady (constant) load to a pre-cracked component the load point displacement increases with time, the data analyzed to determine crack growth rate vs. crack tip parameter K or C^* that gives an initial “tail” with a decreasing growth rate prior to steady-state growth rate.

The data for creep crack initiation (CCI) are taken at crack extensions of $\Delta a=0.2$ mm and $\Delta a=0.5$ mm based on engineering definitions and recommendations of CCI [54]. The CCI times are correlated with the crack tip parameters, stress intensity factor, K , and C^* in order to determine the crack initiation resistance of P91 steel weldments. An indication of CCI resistance of different weldment zones of P91 steel are presented in Figure 4-21 to Figure 4-22. The CCI data are correlated with the loading parameters K and C^* , at crack extensions $\Delta a=0.2$ and 0.5 mm.

Comparison of correlations of CCI resistance of weldment zones of P91 steel in terms of K or C^* reveals that the corresponding BM zone of P91 steel at 600 °C has a higher CCI resistance than WM zone and HAZ zone respectively at both at crack extensions $\Delta a=0.2$ and 0.5 mm. However, the correlation of CCI resistance with C^* shows that the CCI resistance of HAZ zone of P91 steel at 600 °C has a higher CCI than BM and WM, and CCI resistance of P91 BM drops much quicker than the HAZ, although it is slower than WM and HAZ for C^* comparison at early crack initiation times.

The reason for higher CCI resistance obtained at $\Delta a=0.5$ mm than at $\Delta a=0.2$ mm is that the load is increased to grow crack in crack resistant material. Hence, the crack tip parameter has higher values at larger crack extension of 0.5 mm. Therefore, the choice of engineering definition of CCI changes the amount of resistance as well and the determined CCI resistance should not be treated as absolute but an engineering relevant value [91].

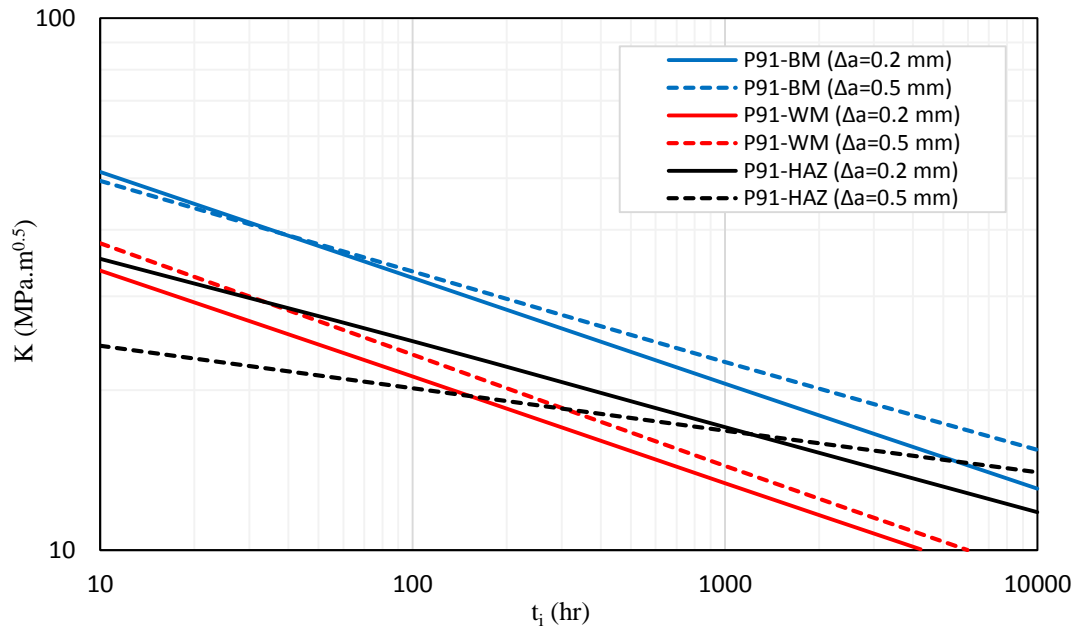


Figure 4-21 Comparison of CCI resistance behavior in terms of K of P91 steel weldment [91]

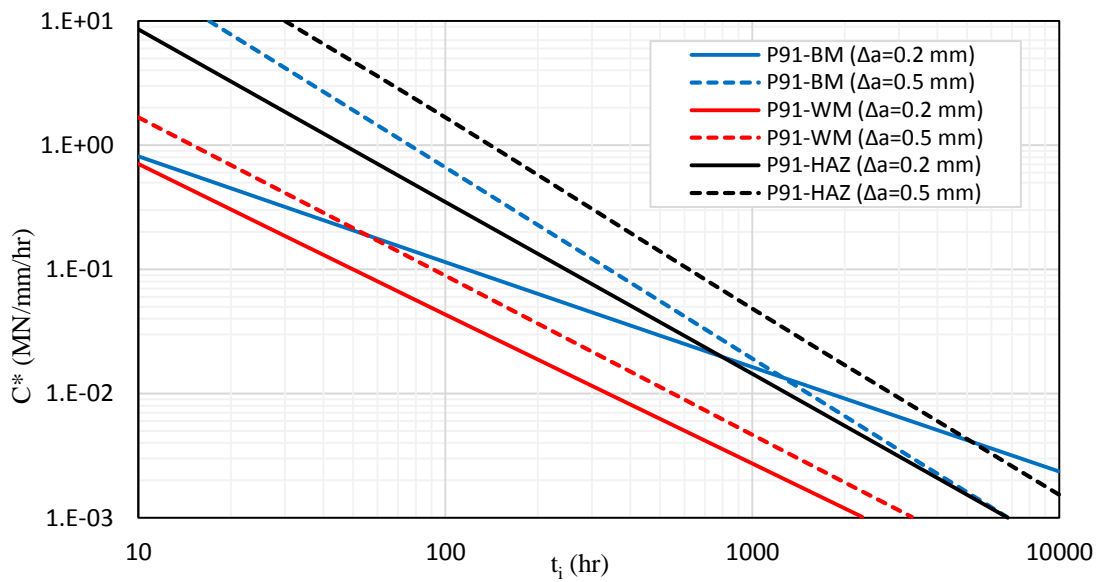


Figure 4-22 Comparison of CCI resistance behavior in terms of C* of P91 steel weldment [91]

Crack initiation times at crack extension of $\Delta a=0.2$ mm and 0.5 mm determined for different weldment zones are correlated with stress intensity factor, K and C^* in Figure 4-23 and Figure 4-24, respectively. The WM has the lowest, and BM the highest crack initiation resistance for crack initiation times defined at $\Delta a=0.2$ mm and 0.5 mm. The rate of reduction in crack initiation resistance is the lowest in the HAZ with crack initiation time, t_i at $\Delta a=0.5$ mm. The type IV fracture mode in the HAZ leads to lower fracture resistance and shorter CCI times [92].

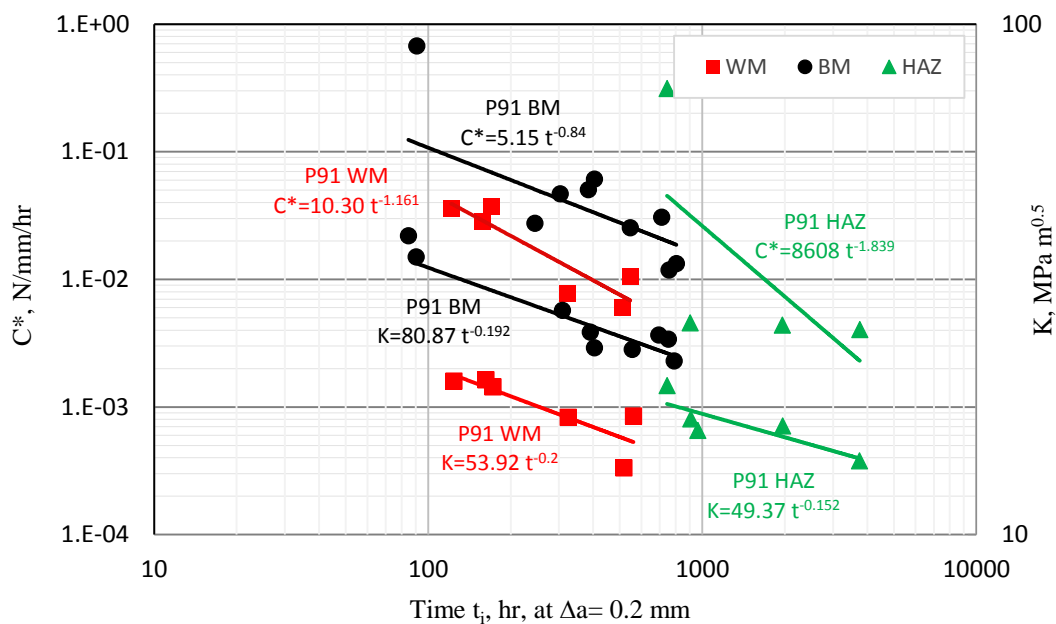


Figure 4-23 Crack initiation resistance of P91 weldment zones at 600 °C in terms of K and C^* correlated with the time to crack initiation at $\Delta a = 0.2$ mm [92].

The C^* correlation with crack initiation times for $\Delta a=0.2$ and $\Delta a=0.5$ mm crack extension, similar to K correlations, WM has the lowest crack initiation resistance. However, on the contrary, to microstructural fracture resistance correlations with K, the HAZ has the highest crack initiation resistance with longer initiation time. For the crack initiation defined at $\Delta a=0.2$ mm in Figure 4-23, the decrease of crack initiation resistance with increasing crack initiation time t_i , is the lowest for P91 BM. Note that the crack initiation

data at $\Delta a=0.2$ mm crack extension has higher scatter than that at $\Delta a=0.5$ mm crack extension as seen in Figure 4-24.

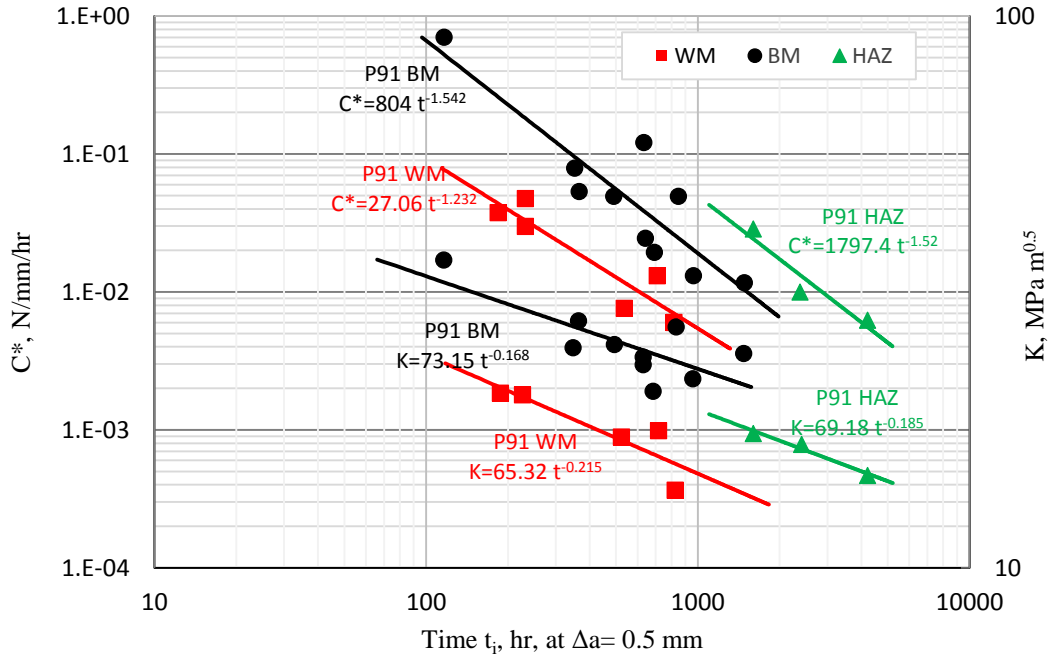


Figure 4-24 Crack initiation resistance of P91 weldment zones at 600 °C in terms of K and C* correlated with the time to crack initiation at $\Delta a = 0.5$ mm [92].

4.4 Experimental Determination of C* Integral

For CT specimens, C* values were calculated using experimental load line displacement rates and creep crack growth data, and then used to correlates the creep crack growth rates. The C* is calculated from the load line displacement rate (also known as crack mouth opening displacement rate) of the recorded data, whereas the magnitude of the C*(t) integral was determined at each point from [80]:

$$C^*(t) = \frac{P\dot{V}_c}{B_N(W-a)} \left(\frac{n}{n+1} \right) \left(\frac{2 + 0.522(W-a)}{W} \right) \quad (4-17)$$

where \dot{V}_c is the creep component of the load line displacement rate and is given as follows

$$\dot{V}_c = \dot{V} - \frac{aB_N}{P} \left[\frac{2K^2}{E} + (m+1)J_p \right] \quad (4-18)$$

where K represents the stress intensity factor given by Equation (4-7), J_p corresponding to the fully plastic component of the J-integral and m is the stress exponent in the Ramberg–Osgood stress versus strain relationship:

$$\varepsilon_p = D_1 \left(\frac{\sigma}{\sigma_y} \right)^m \quad (4-19)$$

where ε_p is the plastic strain, σ_y the yield strength, D a constant, and E is the elastic modulus. The J_p is predicted from

$$J_p = \frac{Dh_1(a/W, m)}{(\sigma_y(W-a))^m} \left(\frac{P}{1.455B_N\alpha} \right)^{m+1} \quad (4-20)$$

where

$$\alpha = (\varphi^2 + 2\varphi + 2)^{1/2} - (\varphi + 1) \quad (4-21)$$

and

$$\varphi = \frac{2a}{(W-a)} \quad (4-22)$$

Finally, h_1 is a function of (a/W) and m , as given in Table X2.1 of ASTM E1457-15 [3]

The traditional way of presenting C^* results is to give the creep crack propagation rate (da/dt) as a function of C^* . This allows for evaluation of the experimentally obtained cracking rates against the calculated C^* -value. When performing remaining life estimates for real components in service, the C^* -value for the component is calculated and the predicted cracking rate is taken from the diagram. The rate is then converted to time until rupture by integrating over the material thickness. The estimate depends on whether plane strain or plane stress conditions dominate at the crack tip. If the material is creep ductile and constraint effects are relatively small, the crack tip stress state can be approximated with plane stress conditions. On the other hand, if the material is creep brittle and the constraint effects are large, a plane strain condition results. In the laboratory specimen, the constraint effects can be changed by altering the specimen size and by introducing side grooves.

It has been shown that for testing and material conditions where secondary creep is dominant, the relationship between da/dt and C^* can be expressed as [93]:

$$\dot{a} = \frac{C^{*0.85}}{\varepsilon_f} \quad \text{plane stress} \quad (4-23)$$

$$\dot{a} = \frac{150C^{*0.85}}{\varepsilon_f} \quad \text{plane strain} \quad (4-24)$$

High temperature crack growth data are determined on specimens from P91 steel weldments at 600 °C. The data are evaluated and CCG rate is correlated with crack tip parameters K and C^* [8]. The crack growth correlations for P91 BM, P91 HAZ and P91 WM are given in Figure 4-25 and Figure 4-26.

The detailed analyses of test data include CCG rate correlated with the crack tip parameter C^* , using the complete dataset and the data after the CCI ($\Delta a > 0.2$ mm and 0.5 mm). The data from early crack extension up to crack growth initiation ($\Delta a > 0.5$ mm) are correlated

with K for transition creep crack growth assessment. The NSW model plane stress and plane strain predictions from Equation (2-72) are overlaid on the CCG correlation charts. The correlations of steady-state crack growth rate with K and C^* can be represented by straight lines of different slopes on log/log plots and expressed by power laws of the form:

$$\dot{a} = A' K^{m'} \quad (4-25)$$

$$\dot{a} = D_o C^{*\phi} \quad (4-26)$$

where A' , m' , D_o and ϕ are material constants. A steady state relationship between crack growth rate and the parameters in Equations (4-25) and (4-26) physically imply a progressively accelerating creep crack growth rate [16], for cracked bodies, at a specific C^* value, using Equation (4-26) the corresponding creep crack growth rate can be calculated, and hence the failure time for a component can be predicted. Material constants A' , m' , D_o and ϕ are given in Table 4-6 and used for the NSW prediction upper and lower bounds. Generally, Figure 4-25 and Figure 4-26 show a high scatter in K correlation of CCG rate whereas much improved correlation with C^* in the valid steady state range is seen.

Table 4-6 Material constants collected from CCG tests of P91 weldments at 600 °C

Material	A'	m'	D_o	ϕ
P91 BM	9.14E-15	8.236	0.0313	0.618
P91 WM	3.02E-19	12.7	0.1143	1.0087
P91 HAZ	1.09E-13	8.36	0.295	1.3523

Crack growth rate versus K for different weldment zones of P91 steel at 600 °C is shown in Figure 4-25, together with the exponential correlations obtained by fitting the data. One can see that BM has significantly higher CCG resistance than both WM and HAZ [94]. Figure 4-25 shows that the creep crack growth rates for the HAZ material is about twelve times higher than that for the BM material and about nine times higher for the HAZ material than the BM material, at the same K values.

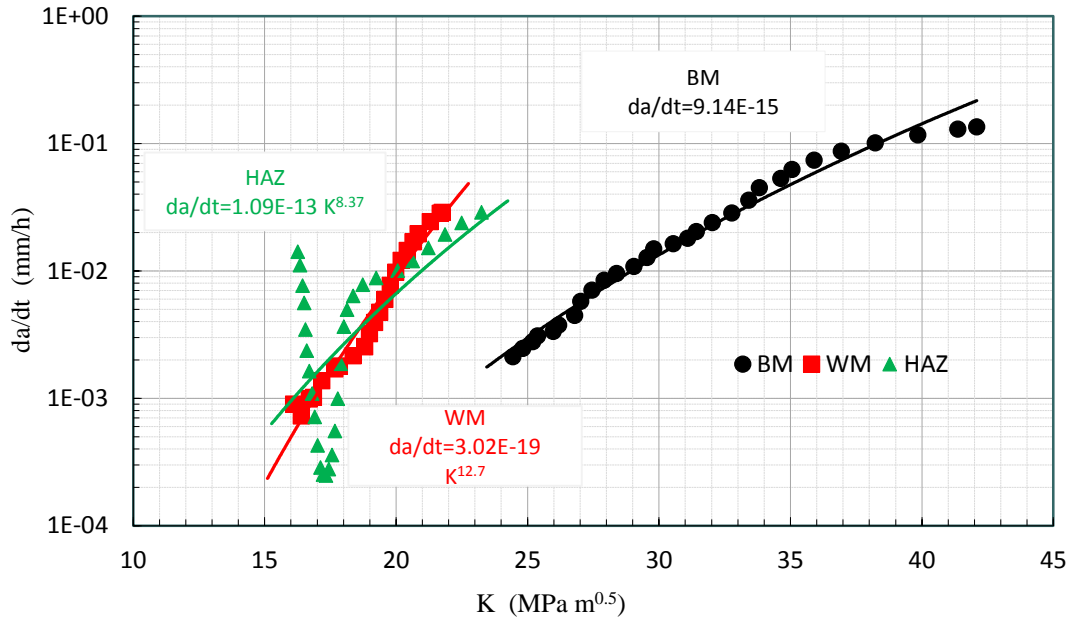


Figure 4-25 Correlation of creep crack growth rate with K for different weldment zones of P91 steel at 600 °C

Crack growth rate versus C^* for different weldment zones of P91 steel at 600 °C is shown in Figure 4-26, together with the exponential correlations obtained by fitting the data. Scatter can be seen to exist in the data, especially at the upper values of C^* for the HAZ values [80], Creep crack growth rates are correlated with the C^* values using Equation (4-26), by curve fitting technique based on the least squares method the values of materials constants D_0 and ϕ are obtained for P91 weldment as presented in Table 4-6. Creep crack growth in HAZ CT specimens is higher than that in BM CT specimens, that is because, in HAZ specimens, initial cracks were positioned in Type IV region, which is the weakest region in a weld. Figure 4-26 shows that the creep crack growth rates for the WM material is about four times higher than that for the BM material and about nine times higher for the HAZ material than the BM material.

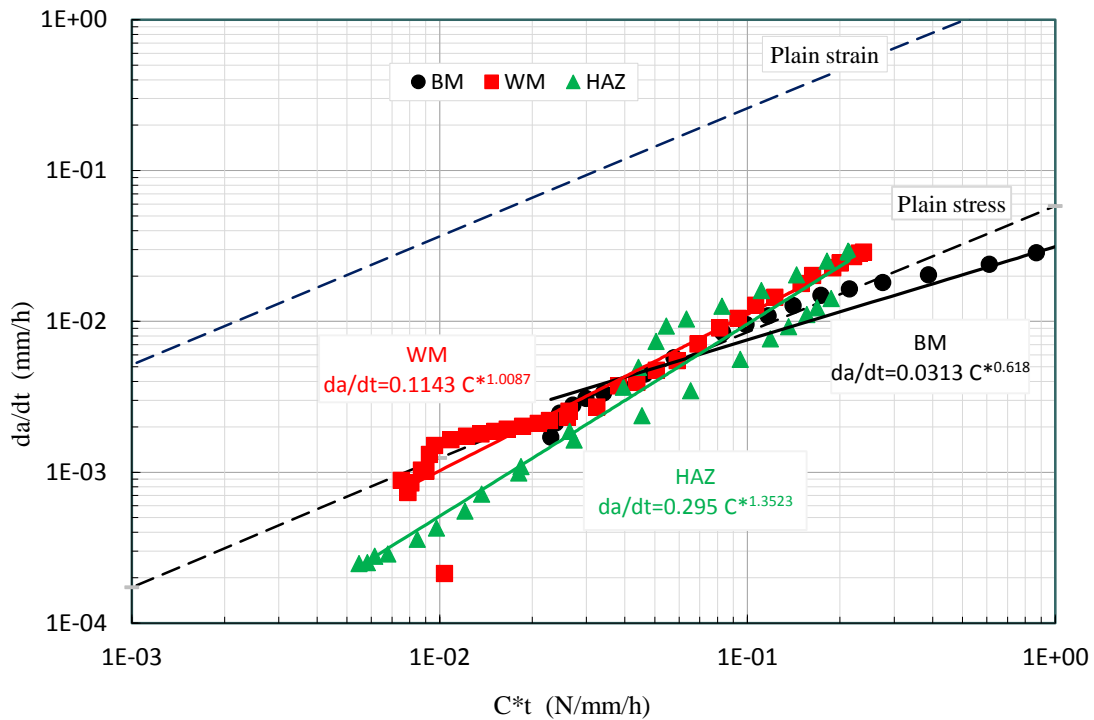


Figure 4-26 Correlation of creep crack growth rate with C^* for different weldment zones of P91 steel at 600 °C

4.4.1 Time Dependent Failure Assessment Diagram (TDFAD) Approach

Failure Assessment Diagram (FAD) method has been developed to assess defect-containing components. The FAD method has been extended to the creep regime, named as TDFAD. This diagram generally gives the prediction whether or not the structure with defined defect will sustain given load. A central feature of the TDFAD approach is the definition of appropriate creep crack initiation toughness, K_{mat}^c . When used in conjunction with the failure assessment diagram, it ensures that crack growth in the assessment period is less than a value Δa . Creep crack initiation toughness values may be estimated indirectly from conventional creep crack incubation and growth data or evaluated directly from experimental load versus displacement information [95]:

$$K_{mat}^c = \left[K^2 + \frac{n}{n+1} \frac{EP\Delta_c}{(W-a)} \eta \right]^{1/2} \quad (4-27)$$

Where η is the geometric factor used for determining C^* given as $[2+0.522(1-a_0/W)]$, K is the stress intensity factor of the specimen, and Δ_c is the experimental load line displacement due to creep at the time for which the crack extension is equal to Δa .

The failure assessment diagram is then defined by the quantities K_r and L_r , which describes fracture and plastic failure mode respectively. These parameters are defined as:

$$K_r = \left(\frac{E\varepsilon_{ref}}{L_r\sigma_{0.2}^c} + \frac{L_r^3\sigma_{0.2}^c}{2E\varepsilon_{ref}} \right)^{-1/2} \quad L_r \leq L_r^{max} \quad (4-28)$$

$$K_r = 0 \quad L_r > L_r^{max} \quad (4-29)$$

$$L_r^{max} = \frac{\sigma_r}{\sigma_{0.2}^c} \quad (4-30)$$

where E is Young's modulus, ε_{ref} is the total strain from the stress-strain curve for given temperature and time and for given value of the reference stress. The variable σ_r is the creep rupture stress obtained from the creep rupture data. Reference stress is obtained from equation:

$$\sigma_{ref} = L_r\sigma_{0.2}^c \quad (4-31)$$

where $\sigma_{0.2}^c$ is the 0.2% yield stress from the stress-strain curve for given temperature and time [96].

The TDFAD curves are constructed and plotted for different weldment zones of P91 steel using the related creep and crack growth properties, as shown in Figure 4-27. The failure predictions for specimen are shown on the TDFADs for engineering definitions of CCI at crack extensions of $\Delta a=0.2$ and 0.5 mm. The curves are constructed for different service times of interest varying from $t=0$ hr to 10^5 hr.

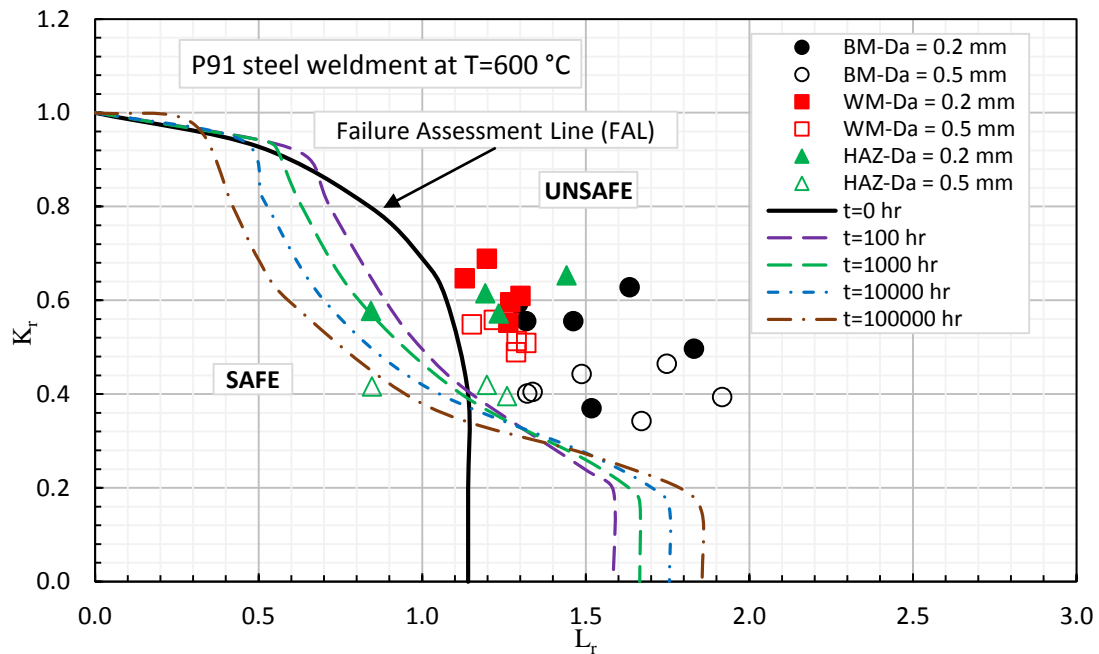


Figure 4-27 TDFAD of P91 weldment at 600 °C for crack growth $\Delta a = 0.2$ mm and 0.5 mm

It is observed that all experimental data from CT specimen lie in the unsafe failure region of the TDFAD for different weldment zones. However, the only point of P91 HAZ specimen lies in the safe region of the TDFAD. The crack initiation determined in this specimen may not have reached the critical value of crack extension.

4.4.2 Application of Two Criteria Diagram (2CD)

The 2CD has been developed to assess creep crack initiation in ferritic steels. Crack tip and ligament damage parameters, R_K and R_σ , respectively, are used in 2CD approach, which are similar to the TDFAD parameters K_r and L_r . For the description of crack initiation using 2CD approach there are three parameters, namely; the stress intensity factor K_I , the path independent integral C^* and the nominal stress in the far field/ligament, σ_n . Among these parameters, K_I is chosen to be used in 2CD, which is designated as K_{lid} , which is the fictitious elastic K that describe the crack tip stress state. K_{lid} parameter is being used to characterize crack tip geometry since K_I solutions are available for a wide range of geometries [97].

The component loading parameters are normalized by time and temperature dependent data, which indicates material resistance.

$$R_\sigma = \frac{\sigma_{n0}}{R_{mt}} \quad (4-32)$$

$$R_k = \frac{K_{lid0}}{R_{li}} \quad (4-33)$$

where R_σ is the far field stress ratio and R_K is the crack tip stress intensity ratio. R_{mt} is the creep rupture strength obtained from tensile specimens. K_{lid0} is the fictitious elastic value at time zero at the crack tip of the component. R_{li} is the creep crack initiation value of the material, which is a material property.

The experimental data from P91 weldment zones of BM, WM, and HAZ are used for 2CD as presented in Figure 4-28. All data fall in the mixed mode damage zone as also confirmed metallographically on tested and fractured CT (W=25 mm, B=12.5 mm) type specimens. Note that the parameter K_{Ii} characterizing the creep crack initiation of the material need to be determined from high constrained specimens with high K_{Iid}/σ_{npl} . For the specimens on which higher loads were applied higher nominal stress, σ_{no} , hence R_{σ} is increased leading to CCI with higher ligament damage.

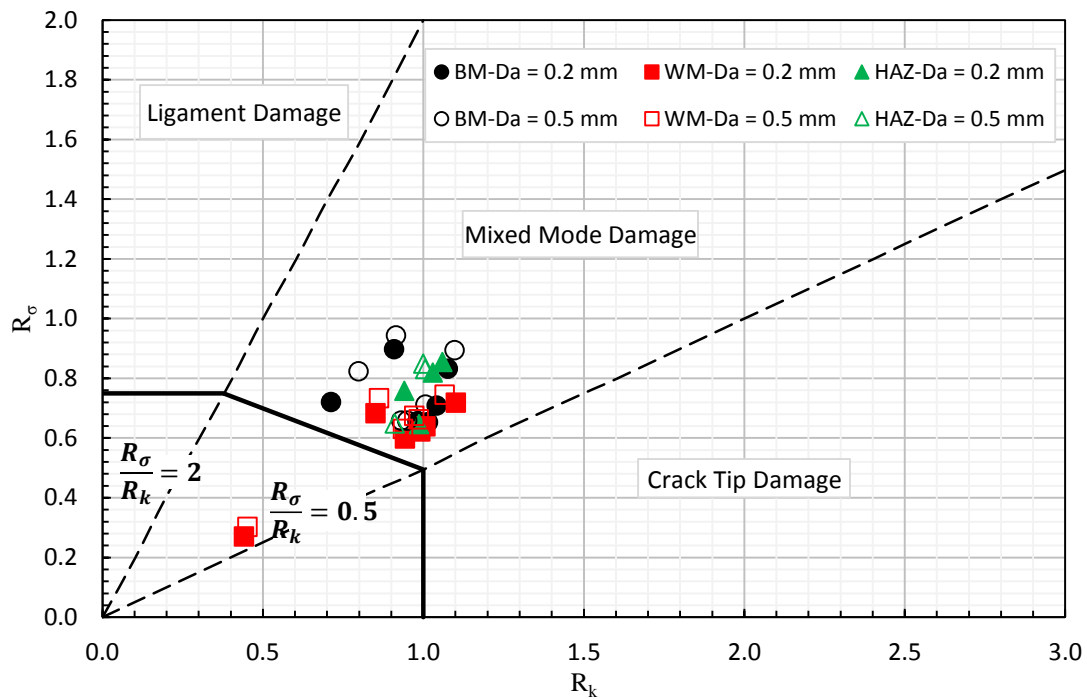


Figure 4-28 2CD of P91 weldment at 600 °C for crack growth $\Delta a = 0.2$ mm and 0.5mm

5 MODELLING OF CREEP CRACK GROWTH AND DAMAGE BEHAVIOUR OF P91 STEEL WELDMENT

The modelling of creep damage behavior of P91 steel weldment is concerned with the use of modern mathematical constitutive models to predict material deformation and failure in engineering structures. The constitutive models used in accordance with the observed microstructural mechanisms of creep deformation and creep failure, which are described in Section 2.2. The constitutive models are based on the notion of a damage state variable (ω), which introduced in chapter 3, through the different creep damage models. The damage state variable is in some sense a measure of the amount of internal voiding present within the material that increases monotonically with time. Damage is included in the constitutive model to provide a coupling with strain rates, as damage evolves then material softens and strain rates increase, during tertiary creep until the material ultimately fails. The amount of damage present within a material may be quantified in terms of the volume or area of voids on a material plane. Measurements of damage detected by optical means, giving an area measurement or by material density changes, giving a volume measurement. Some researchers relate the damage state to the ratio of the damaged area to the original un-damaged area of a material element [98].

5.1 Finite Element Model

Creep crack growth tests were performed at 600 °C on the geometry shown in Figure 5-1 as per ASTM E1457-15 (2015) standard [3]. Side grooves reduced the section thickness B to the net section thickness B_N in order to achieve a straighter crack front. Crack propagation was monitored through the potential drop (PD) measurement system [99], and the test temperature of 600 °C was controlled to allow a fluctuation of no more than ± 1 °C. Test conditions are fully described in Table 4-4.

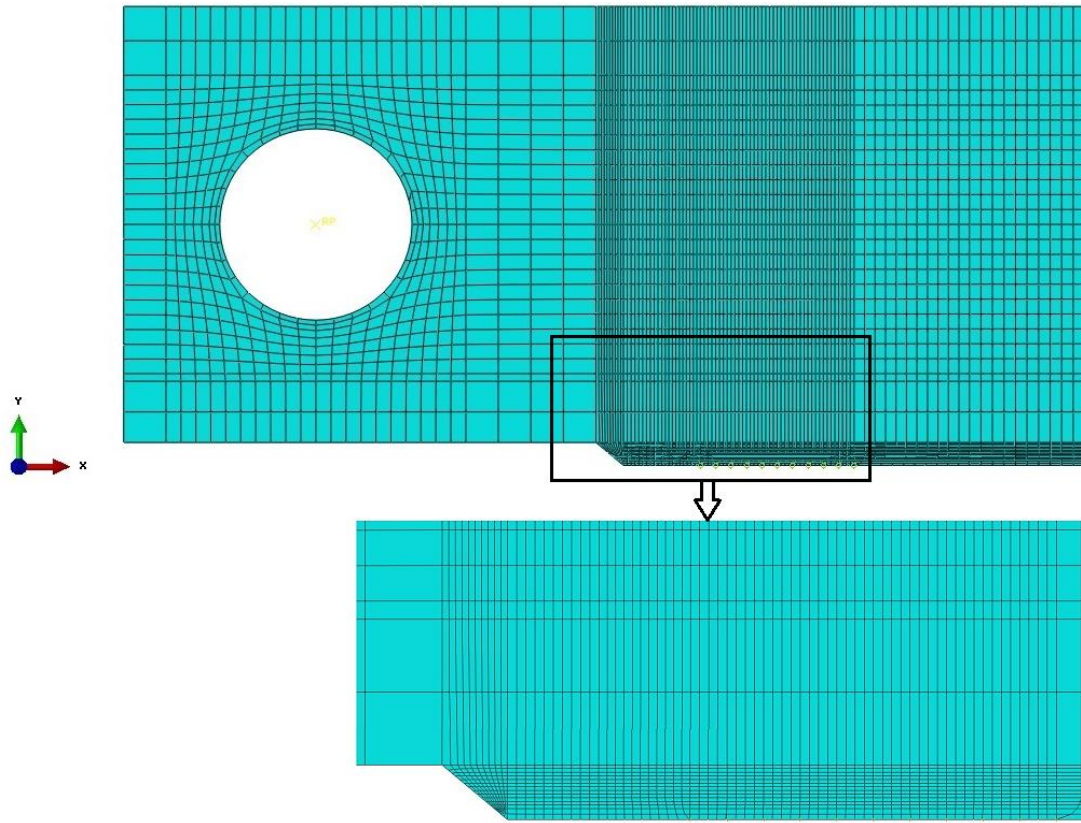


Figure 5-2 CT specimen FE modelling for CCG simulations

Previous work has demonstrated that plane strain analyses are consistent with full three-dimensional (3D) analyses. Three material cases have been considered using material properties of BM, WM and HAZ for P91 steel at 600 °C, as described in Table 5-1, under both plane stress and plane strain conditions. These applied loads are corresponding to the initial stress intensity factors in the CCG tests performed on the P91 weldment material. Simulations have therefore been run, using the constant loading conditions, and reduced integration to reduce computing time.

Table 5-1 Details of CT specimens modelled and loading conditions

Sl. No.	Specimen	Duration (hr)	Load (N)	K (MPa.m ^{0.5})	C* (N/mm/hr)	a ₀ (mm)	Δa (mm)	ε _f
1	CT25-BM	766.8	3800	22.56	0.056	13.211	1.528	0.130
2	CT25-WM	2141.2	3300	13.04	0.007	11.927	5.495	0.020
3	CT25-HAZ	4852.5	2600	13.68	0.004	10.692	4.075	0.130

5.1.1 The Load Line Displacement (LLD) FE Prediction

The LLD and crack extension predicted by 2D FE simulations under plane stress and plane strain conditions using the stress dependent ductility criteria have been compared to the existing experimental data for weldment material where the data were available from the tests performed at a similar initial stress intensity factor. Note that the designed mesh employed in this work is made to study the CCG behavior of the weldment. Thus to exclude the initiation effects in direct comparisons between the FE predictions and the experimental data, the CCG time, LLD and crack extensions beyond 0.5 mm crack growth are presented in Figure 5-4.

The dimensions of a standard CT specimen presented in Figure 4-1 were used to model the specimen in the general finite element software of Abaqus. This means that the W of the specimen was equal to 25 mm. A model of the whole CT specimen is shown in Figure 5-3. The crack ratio (a/W) was 0.5. The crack-tip region had a much finer mesh than the other regions, such that C(t) could be calculated using the standard domain integral function provided in Abaqus. The minimum mesh size at the crack-tip region was 10 μm and the ratio of this value to W was 25x10⁻⁴. In the model, 1327 elements were used with 4204 nodes. Loading was directly applied to the loading point of the rigid pin, as seen in Figure 5-3. Therefore, the loading was applied to the specimen by the rigid pin, as in actual tests. The element type CPE8R was used, which is an eight node, plane strain, and reduced integration element. All of the applied loads were fixed at 3000 N. The material properties of the P91 materials for BM, WM and HAZ were considered through the use of the partition options for different materials implementations.

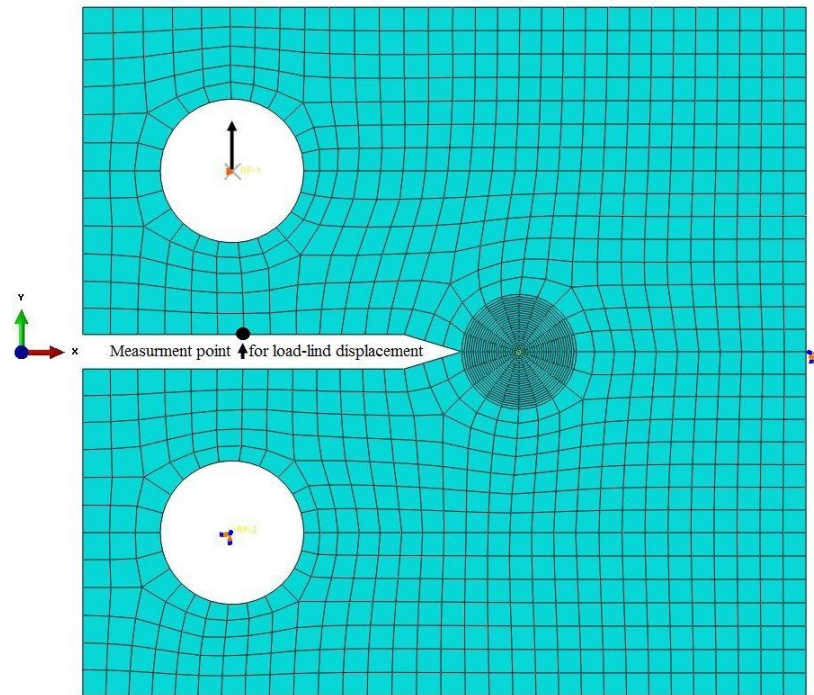


Figure 5-3 Finite element simulation results and comparison with the experimental CCG data

The simulated load-line displacement gives a good correlation with the corresponding experimental results at $K_0 = 22.56 \text{ MPa m}^{0.5}$, $K_0 = 13.04 \text{ MPa m}^{0.5}$ and $K_0 = 13.68 \text{ MPa m}^{0.5}$ for BM, WM and HAZ respectively. This might be an indication that the uniaxial creep behavior is accurately represented at low stresses while at higher stresses additional uniaxial creep tests are required. In fact, in Figure 5-4, the main difference with the experimental data is in the tertiary part of the curve, which strongly depends on creep behavior and controlling of test termination before fracture, while in the first and second part of the curve that depends on crack propagation, the load-line displacement slope is consistent with the simulated values. It can be seen that the FE results are always lower than the experimental results in its magnitude. However, the FE and experimental results have nearly the same gradients in the steady-state region.

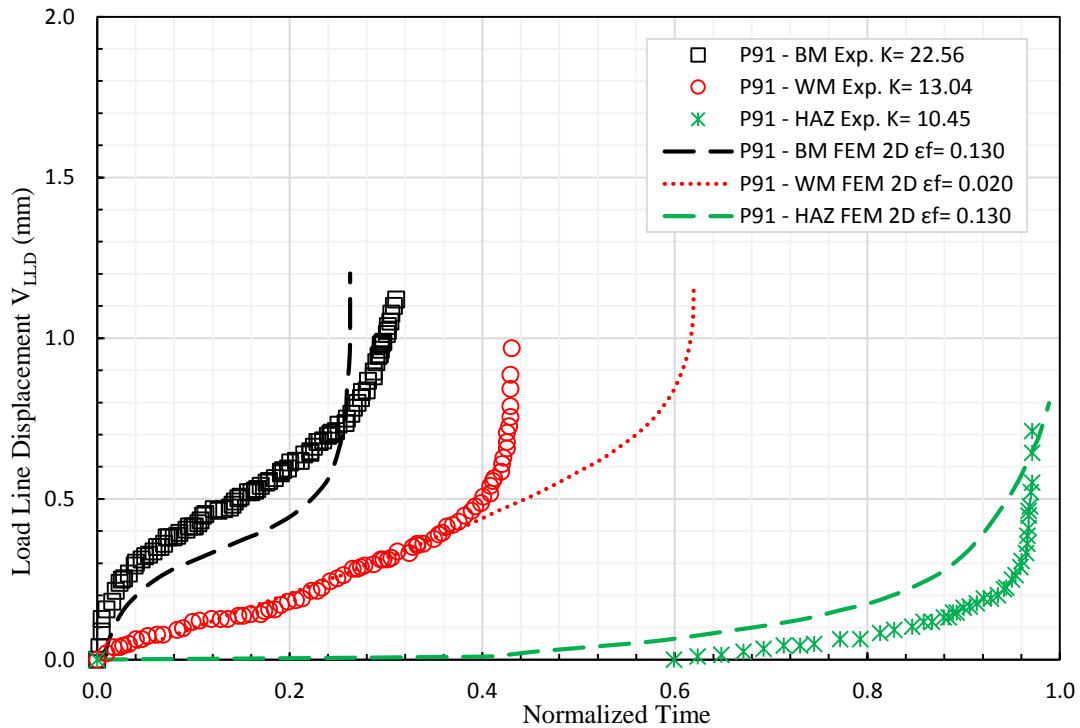


Figure 5-4 Finite element simulation results and comparison with the experimental CCG data

5.1.2 The Fracture Parameter (C^*) FE Prediction

The FEM has been widely used to calculate C^* using CT specimens. Firstly, it was used to obtain FE steady state load line displacement rates, for CT specimens, which were then used to calculate C^* [102]. Latest versions of FE modeling codes namely ABAQUS has built-in functions to calculate the contour integral $C(t)$. In creep analysis $C(t)$ approaches a constant value when the analysis reaches steady-state creep. This constant value of $C(t)$ is C^* parameter. Whether using FE load line displacement rates or the built-in contour integral function $C(t)$, to obtain C^* , FE analyses have been carried out using stationary crack CT specimens [103].

FE determined C^* values, based on steady-state values of $C(t)$, for P91 CT specimens at 600°C , are presented. Stationary crack analyses were performed initially, and these were used to predict growing crack behavior. Using collapsed elements (singular elements) to accurately model the crack tip singularity, and hence to obtain accurate contour integral

values, the collapsed elements are placed at the crack tip, which are recommended for crack analysis to reduce the mesh sensitivity at the crack tip as shown in Figure 5-5 the CT model meshes using 2D (4 nodes) collapsed elements. However, it was necessary to use quadrilateral elements to ease the modeling of growing cracks by 2D (8 nodes) quadrilateral elements seen in Figure 5-6. One-half complete thickness of the specimen was modelled because of symmetry; the crack plane is the plane of symmetry on which the boundary conditions were applied. In both models, the plane of symmetry was constrained in the Y-direction while the load point was constrained in the X-direction; to prevent rigid body motion in the X-directions. Plane strain linear elements were used for the collapsed element model and plane strain quadratic elements were used for the quadrilateral elements model. The geometry and dimensions of the CT model are the same as those used for the experimental CT specimens, shown in Figure 5-1, the FE analyses for P91 weldment zones BM, WM and HAZ for the same loading conditions provided in Table 5-1.

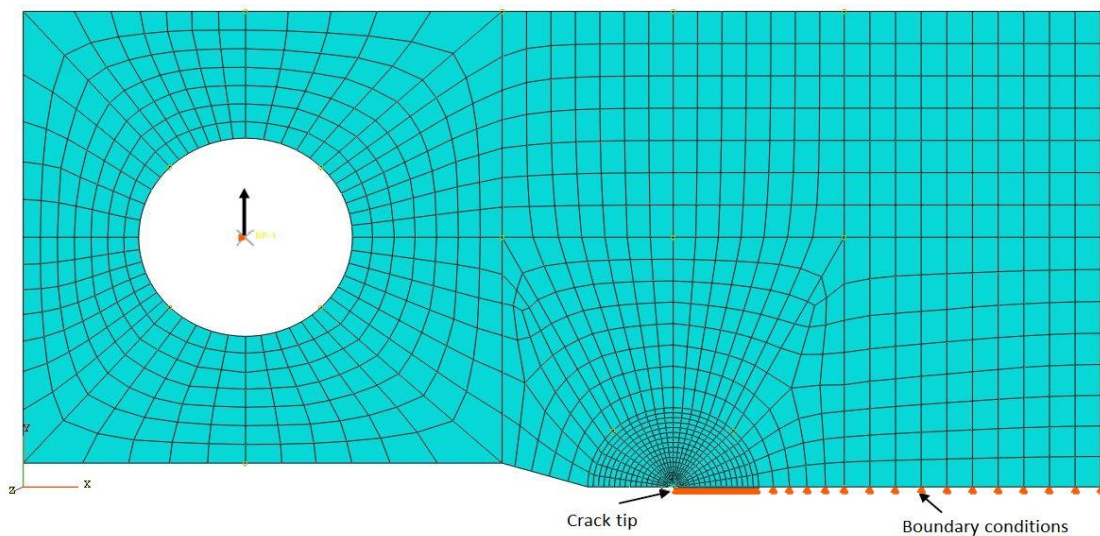


Figure 5-5 FE CT model using collapsed elements ahead of the crack tip

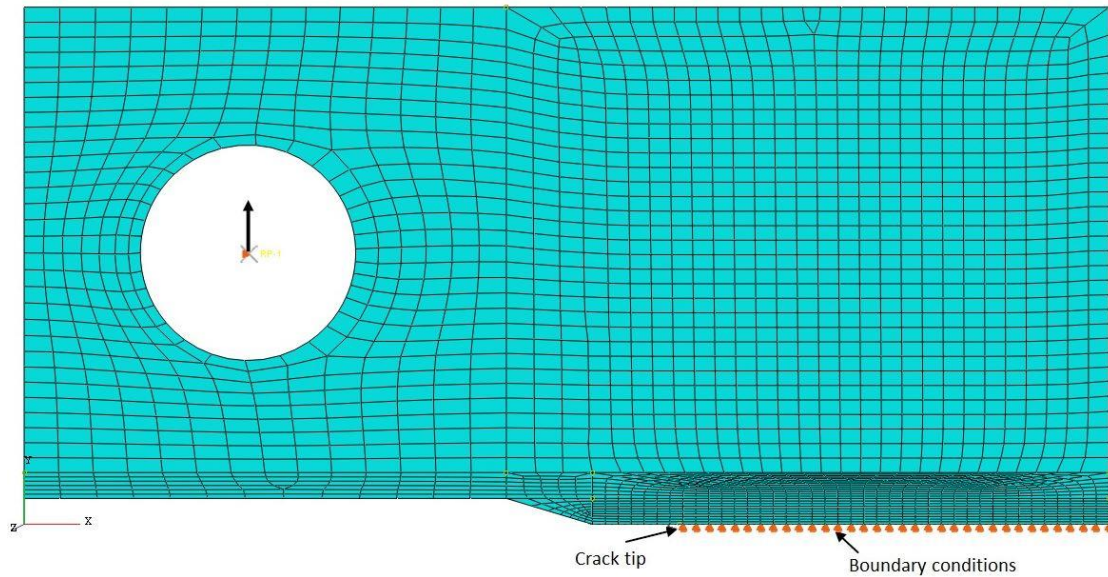


Figure 5-6 FE CT model using quadrilateral 8-node elements ahead of crack tip

In comparison, the FE contour integrals achieved with the use of both models that are collapsed 4-nodes elements model and quadrilateral 8-nodes elements model as presented in Figure 5-7, when the initial crack was 12.5 mm. It can be seen that the contour integral $C(t)$ decreases as time increases until it reaches an approximately constant value. This constant value is C^* . In addition, it can be seen that the contour integral obtained for both models are practically the same. These results reinforce the use of quadrilateral elements in the analyses in which crack propagation is included.

FE C^* analyses were conducted for P91 weldment CT specimens at twelve different initial crack lengths. C^* values were taken as the steady state value of the contour integral $C(t)$. It is assumed that steady state is reached when the changes in the analysis time increments produce negligible changes in the $C(t)$ values. The resulting value of $C(t)$ is taken to be C^* and the corresponding time is taken to be the transient time, that is the time at which the creep zone is well spread in the CT specimen. These values are given in Table 5-2, also indicated in Figure 5-8 for P91 weldment with a crack length of 12.5 mm. The FE predictions show higher values for HAZ at initial crack growth.

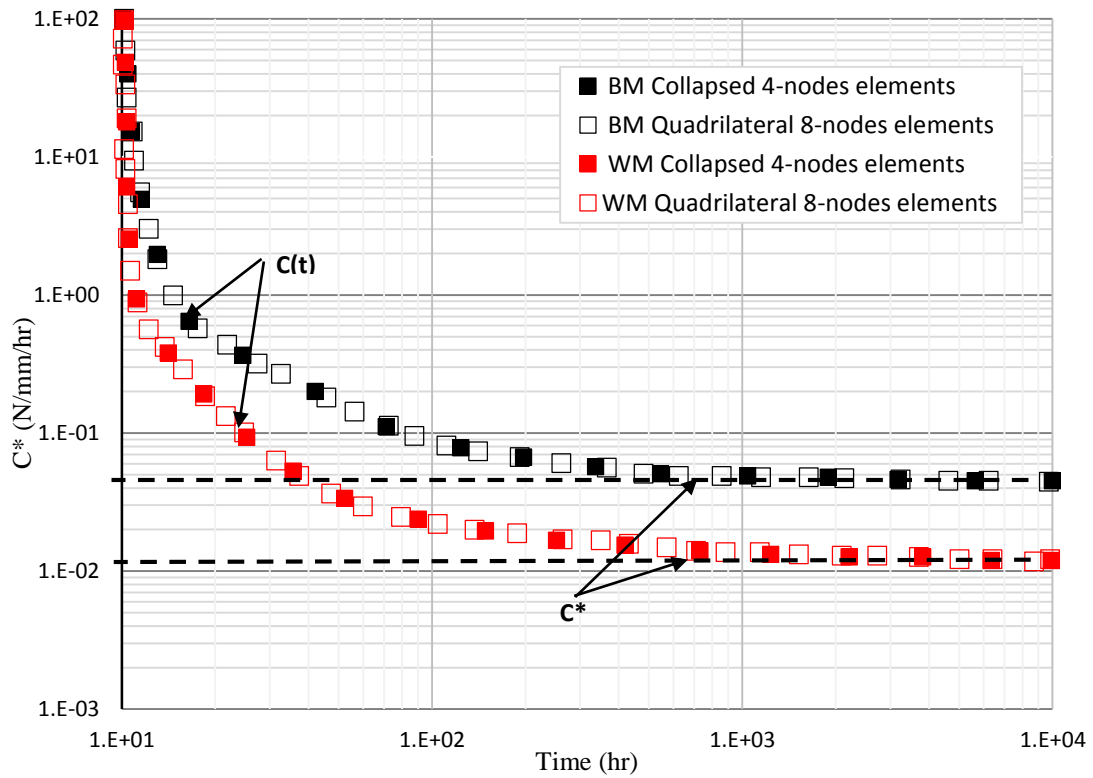


Figure 5-7 FE C(t) integral by quadrilateral 4-node and collapsed elements for P91 weldment

Table 5-2 FE models C* values and transient times for P91 weldment

Crack Length (mm)	BM - 600 °C		WM - 600 °C		HAZ - 600 °C	
	C* (N/mm/hr)	FE t _T (hr)	C* (N/mm/hr)	FE t _T (hr)	C* (N/mm/hr)	FE t _T (hr)
12.5	0.03167	9.915	0.00873	23.686	0.05314	2.058
13.0	0.19339	6.808	0.01365	17.177	0.06981	1.781
13.5	0.35511	3.700	0.04173	6.442	0.25505	0.557
14.0	0.51683	2.993	0.29852	2.419	0.41552	0.371
14.5	0.67855	2.485	0.55531	2.168	0.95319	0.192
15.0	0.84027	2.078	0.81209	1.917	1.35177	0.150
15.5	1.00199	1.971	1.06888	1.666	2.47838	0.099
16.0	1.16371	1.863	1.32567	1.414	4.41063	0.067
16.5	1.32543	1.731	1.58246	1.163	6.34288	0.035
17.0	1.48715	1.328	1.83925	0.912	8.27513	0.022
17.5	1.64887	0.824	2.09604	0.660	10.20738	0.016
18.0	1.81059	0.320	2.35283	0.409	12.13964	0.009

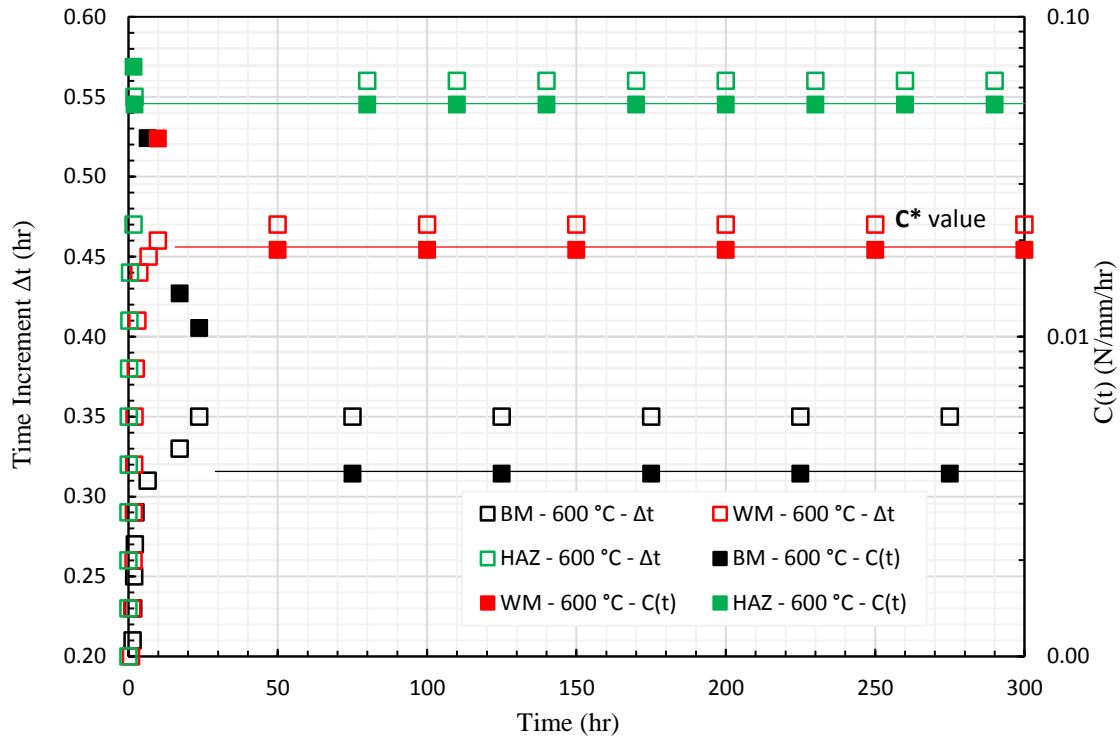


Figure 5-8 Variations of time increment Δt and contour integral $C(t)$ for P91 weldment

5.1.3 FE Modelling of CT Specimen Growing Crack

The 2D CT growing crack model of plane strain quadrilateral elements that found to give values of C^* closer to the corresponding experimentally obtained values, and because of symmetry, only half the specimen was modelled. Element thicknesses were taken to be 12.50 mm, this being the actual CT specimen net thickness as presented in Figure 5-9. To grow the crack, the first 5 mm ahead of the crack tip was divided into 40 segments Δa , each being 0.125 mm in length, because the largest creep crack growth extension obtained experimentally is about 5 mm for the WM at 600 °C see Figure 4-16. Boundary conditions were applied to these segments to constrain them in the Y-direction. These boundary conditions were then released, during the analysis, one after another allowing the crack to grow by 0.125 mm each time. This technique is known as the node release technique, for growing cracks. This extension of the crack was modelled in a stepwise manner. Two steps are needed to grow the crack by one increment Δa . The first step is to release the

boundary condition; the time taken for this step is very small (about 0.01h). In the following step, creep takes place and a C^* value was obtained.

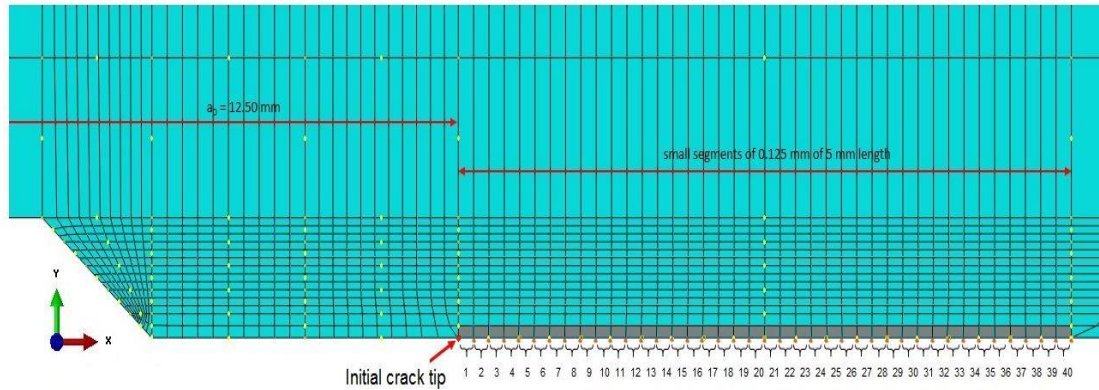


Figure 5-9 Fine meshed crack segments ahead of crack tip

Enabling the step times given in Table 5-2 and the growing crack model, an FE analysis was carried out to calculate C^* values. The boundary conditions applied to the elements ahead of the crack tip were released one after another, in order to grow the crack. Figure 5-10 shows the deformed shape of the CT model and the released boundary conditions.

Figure 5-11 compares the values of C^* obtained from the growing crack model with those of the experimental results. It can be seen that the growing crack model gave practically the same C^* values as experimental results at the same crack lengths. This indicates that the C^* values determined by the growing crack model can be used to characterize the behavior of the P91 weldment materials.

The FE growing crack modelling of CT specimens using Abaqus provides FE load line displacements curves presented previously in Figure 5-4, these displacement curves can then be used to calculate displacement rates which can be used to calculate the corresponding C^* values [104]. This approach was used and resulted in good correlation between experimental and FE load line displacement rates, and hence C^* values in modelling P91 weldments CT specimens at 600 °C [87].

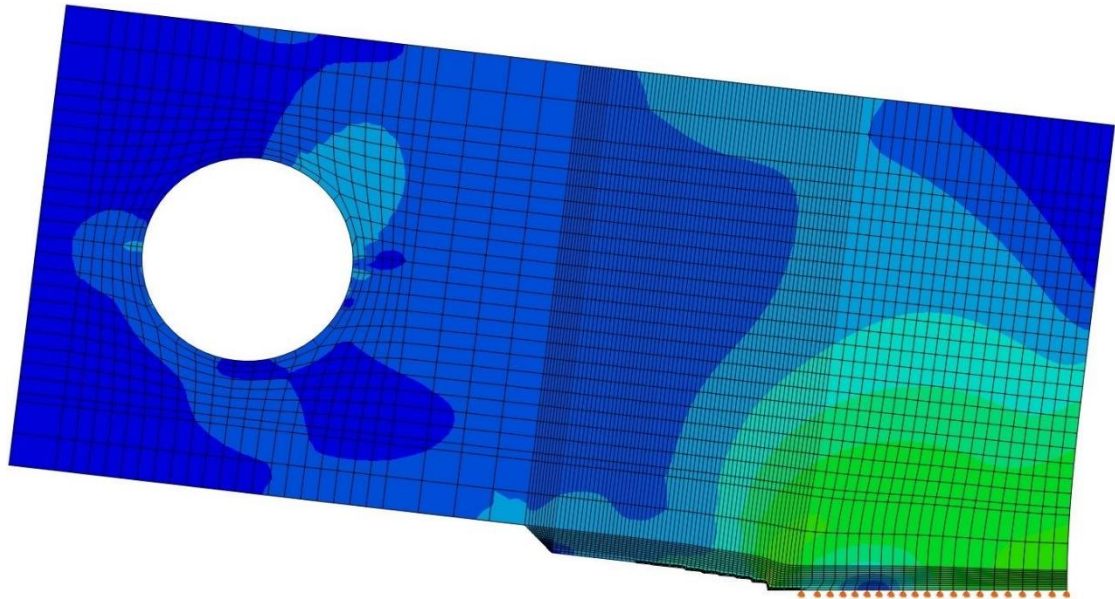


Figure 5-10 Released elements of the growing crack mode

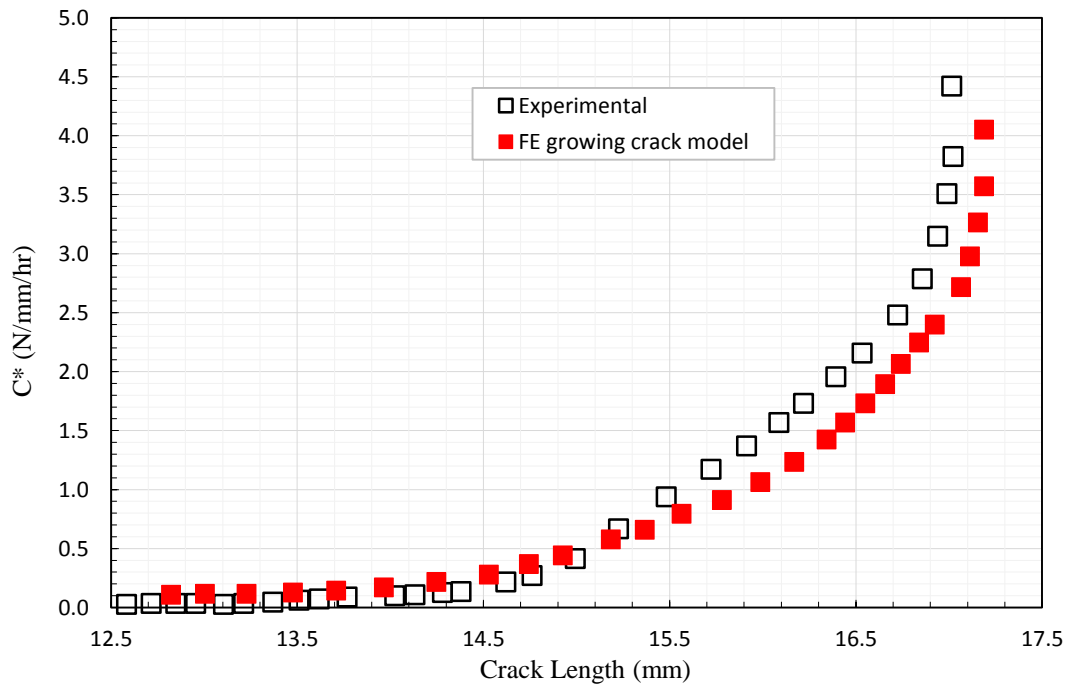


Figure 5-11 FE C* predictions for growing crack models vs. experimental data

The benefit of using the growing crack model is the ability to obtain the load line displacement curves and to calculate the creep crack growth rates, which used in comparing the da/dt vs. C^* from the experimental data with the FE results. Figure 5-12 present this comparison for the P91 WM at 600°C. It can be seen that the FE results, obtained using the growing crack model, are in good agreement with the experimentally calculated results. Creep crack growth correlation when using plane strain and plane stress C^* FE predictions, clearly, it can be seen that for the same C^* the plane strain conditions produce higher creep crack growth rates than the plane stress conditions do. Similarly, for the plane strain conditions, WM CT specimens exhibit higher scatter than the BM CT specimens under the plane stress conditions. Furthermore, both the plane strain and the plane stress conditions have the same slope for weldment CT specimens.

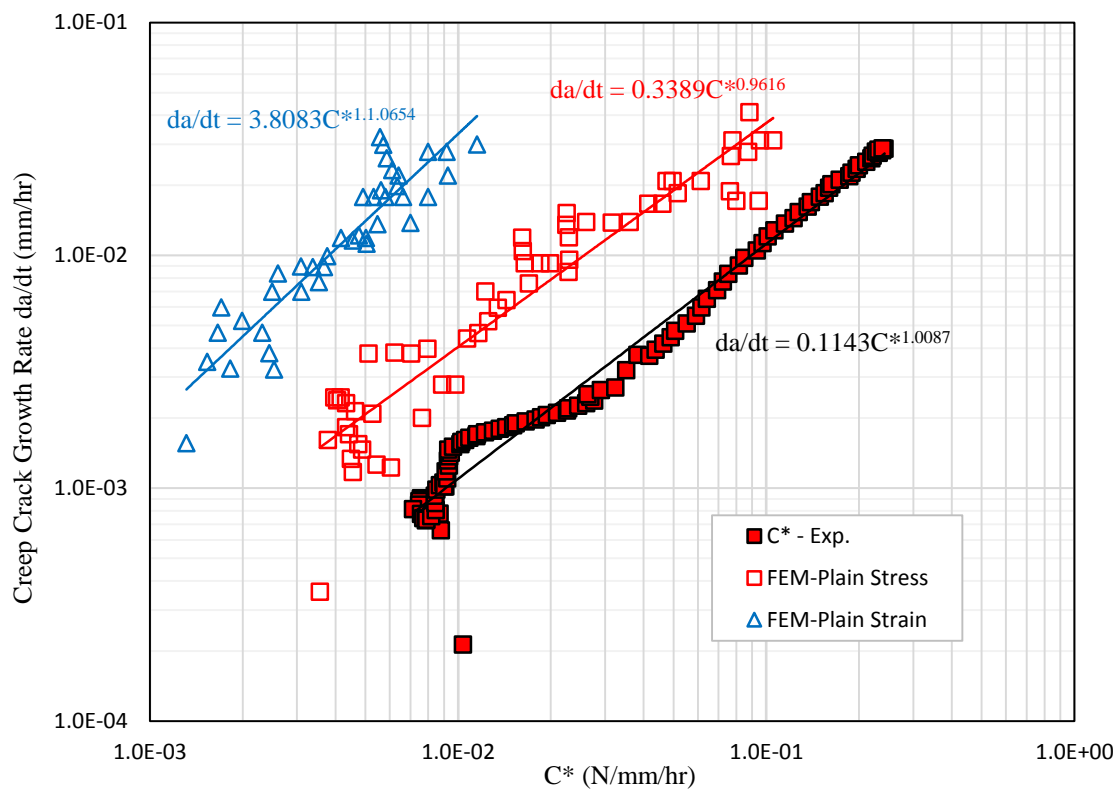


Figure 5-12 Comparison of FE obtained C^* vs. CCG with experimental data [87]

5.1.4 FE Evaluations of C^* by Secondary and Average Creep Strain Rates

As briefly described in Section 2.2.5, predictions of deformation in a component will be underestimated when using the minimum creep strain rate $\dot{\epsilon}_s$, that is because the components of deformation related to tertiary and primary creep are neglected and only the steady state deformation is considered. Therefore, if Norton's equation is to be used to predict deformation of "average" strain rate $\dot{\epsilon}_A$, defined in Figure 2-13, would be an alternative method which would produce more representative deformation rates for extended times. The average creep rate $\dot{\epsilon}_A$ is defined by:

$$\dot{\epsilon}_A = A_A \sigma^{n_A} \quad (5-1)$$

where $\dot{\epsilon}_A$ is the average creep strain rate and A_A and n_A are material constants, which are obtained in a similar way to that used to obtain A and n of the minimum creep rate, by plotting $\log(\dot{\epsilon}_A)$ against $\log(\sigma)$, from the straight line of the best fit to the test data the slope of the line is n and the intercept of the line is $\log(\sigma)$.

Table 5-3 presents the values of Norton equation constants for minimum A , n , and average A_A , n_A for the P91 steel weldment at 600°C.

Table 5-3 Material constants of minimum and average creep rates of P91 weldment at 600 °C

Material	A	n	A_A	n_A
P91 BM-600 °C	1.570×10^{-45}	18.510	1.478×10^{-39}	12.515
P91 WM-600 °C	5.990×10^{-24}	8.550	8.408×10^{-26}	9.728
P91 HAZ-600 °C	7.160×10^{-35}	14.350	6.740×10^{-29}	9.702

C^* analyses using FEM by ABAQUS were conducted for P91 BM, WM and HAZ CT specimens with different loading conditions and same initial crack lengths. C^* values were taken as the steady state value of the contour integral $C(t)$.

Figure 5-13 shows the variation of the FE C^* values with creep crack extension for P91 weldment including comparison with the experimental results, the FE and Experimental

were calculated using minimum strain rate material constants, i.e. A and n , and average creep strain rate constants, i.e. A_A and n_A . Clearly seen that the FE C^* values calculated using minimum constants agree well with experimental results. However, the FE C^* values calculated using the average constants are higher in all weldment different materials that is simply due to the fact that average values cover all three creep regimes and extend to longer time.

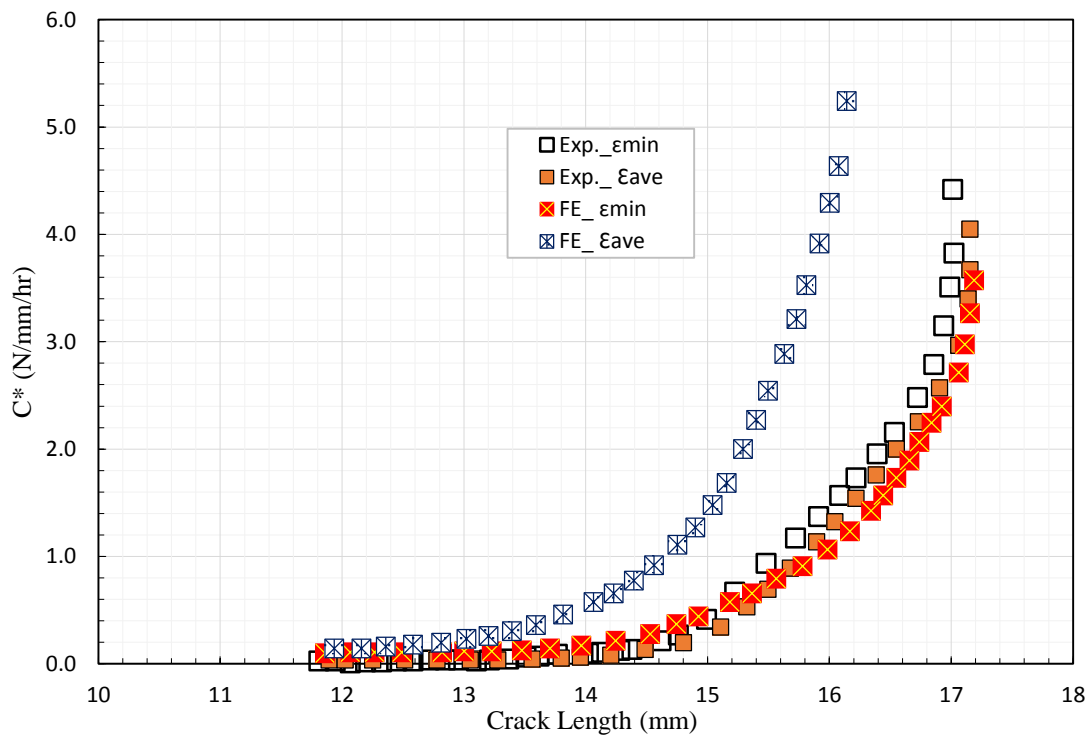


Figure 5-13 FE C^* versus creep crack length for minimum and average creep strain rate

5.2 Creep and Damage Models of P91 Steel Weldments

The practical experience and approaches to creep modeling in welded structures using FEM during the last 10 years considering the partition of the weldment volume to three zones considering different material behavior under the creep conditions [105].

Creep damage modelling in cracked components to study the rupture life of components made of engineering materials under creep deformation conditions to simulate CCG

behavior of materials using FE simulations. In the previous section, fracture mechanics approaches have been used to predict creep crack growth in CT specimens for P91 weldment. However, it is difficult to use fracture mechanics for cases other than those used to predict the steady-state behavior of components. Therefore, damage mechanics approaches have been used to model all creep stages, i.e. primary, secondary and tertiary creep. Damage mechanics can, also, account for material deterioration, which will allow accurate predictions of failure times and location of components.

The approach is to simulate crack growth by element removal when the damage parameter ω , reaches a critical value at two integration points in an element located ahead of the crack tip, the crack tip node releases and virtual crack propagation is modelled [87], as presented in Figure 5-14. In this method, which is often referred to as node release model, the crack path has to be specified prior to CCG simulations. The defined crack path in node release model is usually along the symmetry line at the mid-height of the specimen geometry [48].

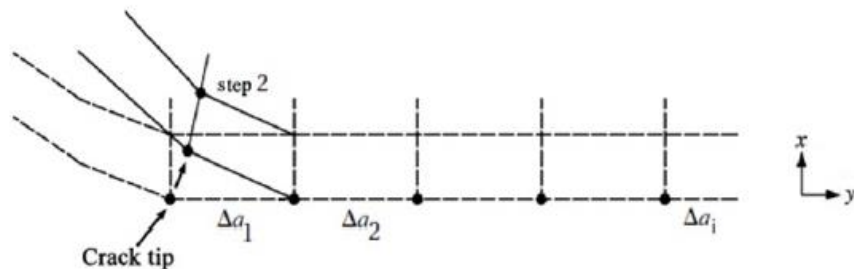


Figure 5-14 Schematic of node release modeling for creep crack growth [87]

Damage mechanics have been used to predict creep crack growth in CT specimens, using the Abaqus Student Edition FE package [76]. A FORTRAN subroutine, CR_DAMAGE subroutine [77], was used to implement the damage models for the FE analyses. Considering two creep damage models were used to predict deformation and lifetime of

creep behavior of components namely the Kachanov and Rabotnov model introduced in Section 3.3.1 and the Liu and Murakami model presented in Section 3.3.2. It is necessary to determine several material constants to facilitate these damage models. The experimental results given in Chapter 4 were used to determine these material constants.

5.2.1 Determination of Material Constants for Creep Damage Models

Creep behavior is often represented by coupled, continuum damage constitutive equations, which can be used in finite element analyses to predict the time-dependent deformation and creep failure times of engineering components, and structures at elevated temperatures. The accuracy of these predictions is strongly dependent upon the accuracy of the material constants in the creep continuum damage constitutive equations.

In order to determine the material constants in the constitutive equations of a material model, the common practice is to reduce the tri-axial model to its uniaxial form and then to fit the uniaxial constitutive equations to the test data obtained from sets of uniaxial creep tests at desired temperatures. Most of the material constants in constitutive equations can be determined from uniaxial test data; however, for some material constants, bi-axial tests or multi-axial finite element damage analysis has to be employed. The uniaxial parameters A , n , ϕ , B , χ and m shown in equations (3-6) and (3-7) can be determined by fitting a group of creep test strain curves for different stress levels at fixed temperature to the theoretical strain equation (3-10). To obtain the α values, notched specimen rupture testing can be used in conjunction with FE damage modelling of notched bar rupture tests [70].

5.2.1.1 Determination of Norton Model Material Constants (A and n)

Norton's law is the most commonly used model to describe the secondary creep region (steady state region), because of its simplicity and accuracy [106].

$$\dot{\epsilon}_c = A\sigma^n \tag{5-2}$$

where A and n are temperature dependent material constants, σ is the stress and $\dot{\epsilon}_c$ is the minimum strain rate which depend only on the stress and the temperature. The material constants A and n were obtained using the uniaxial creep tests of specimens for P91 steel at 600°C, by plotting the minimum strain rate against the applied stresses on a log-log scale and then determining a line of best fit. The slope of the line of best fit is n and the intercept is $\log(A)$, which are presented in Table 5-3

5.2.1.2 Determination of Material Constants for Damage Models (M, χ, B, ϕ, α and q_2)

The most commonly used damage models are the Kachanov and Rabotnov material behavior model [61], and the Liu and Murakami model [64]. Both are capable of modeling the entire creep strain curves. The models consist of pairs of coupled creep and damage equations that are capable of representing the damage in the material during creep, both models have been described in Sections 3.3.1 and 3.3.2 respectively. The material constants for Kachanov-Rabotnov and Liu-Murakami models, i.e., (M, χ, B, ϕ, α and q_2) for P91 steel weldment zones BM, WM and HAZ at 600 °C have been obtained using uniaxial creep strain versus time curves results for weldment materials which are presented in Figure 5-15.

In practice, only initial estimates of the model's material constants are determined directly from experimental data. These initial estimates are then fine tuned using an optimization procedure; fitting the predicted behavior of a material model to the true experimental response. An optimization iteration (i.e. an instantaneous solution for the optimum set of material constants) is based on the evaluation of an objective function. For the optimization of creep material parameters, the objective function may take the form of Equation (5-3), where M_1 is the number of creep tests performed and M_2 is the number of data points for the i^{th} creep curve. Experimental and predicted strain values ϵ_j^{exp} and $\epsilon_j^{pre}(x)$ respectively, where x is a set of material constants are compared for each data

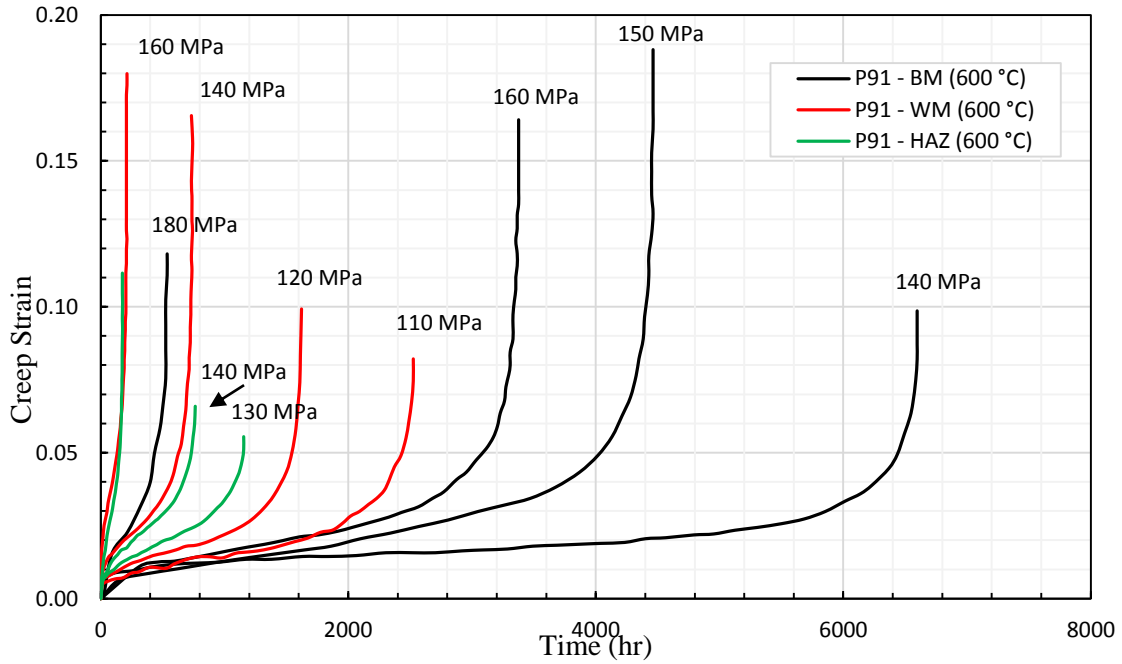


Figure 5-15 Uniaxial creep strain versus time curves for P91 weldment at 600 °C

$$F(x) = \sum_{i=1}^{M_1} \left\{ \left[\sum_{j=1}^{M_1} (\varepsilon_j^{pre}(x) - \varepsilon_j^{exp})^2 \right]_i + \omega_i \frac{|t_{fi}^{pre}(x) - t_{fi}^{exp}|}{t_{fi}^{exp}} \right\} \rightarrow \min \quad (5-3)$$

point in each creep curve. Predicted and experimental times to failure t_{fi}^{pre} and t_{fi}^{exp} respectively are also compared by using the weighting value ω_i to ensure that times and strains are accounted for with similar magnitudes.

Material constants M and χ can be determined in a straightforward manner using the minimum strain rate and failure times of uniaxial creep data, given by

$$t_f = \frac{1}{M\sigma^\chi} \quad (5-4)$$

values of constants M and χ can be determined by plotting $\text{Log}(t_f)$ versus $\text{Log}(\sigma)$. By taking $\text{Log}(\)$ function to Equation (5-4) and becomes

$$\log(t_f) = -\log(M) - \chi \log(\sigma) \quad (5-5)$$

M and χ values can be obtained as the slope of the line of the best fit is $-\chi$ and the intercept is $-\text{Log}(M)$, and

$$M = B(1 + \phi) \quad (5-6)$$

Similarly, the material constant ϕ can be determined by fitting a set of uniaxial creep curves calculated using Equation (3-10) to the corresponding experimental creep curves at different values of ϕ , keeping all the other material constants the same. The ϕ value that gives the best fitting is then taken as the correct value. Then, the B value is updated whenever the ϕ value changes, according to Equation (5-6)

The material constant m is initially set to zero until the exact value of ϕ was obtained, then, ϕ kept constant and the m value is changed accordingly to enhance the fitting, not much improvement achieved to the fitting by adjusting m value, so it is kept equal to zero for all weldments material. Other material constants, such as q_2 and α , are determined using fitting to the overall experimental data. P91 Material constants for damage models at 600°C (σ in MPa and time in hr) are presented in Table 5-4

Table 5-4 P91 weldment constants for damage models at 600 °C

Material	A	n	m	B	ϕ	χ	α	q_2
P91 BM	1.478x10 ⁻³⁹	12.51	0	2.335x10 ⁻²⁷	9.745	9.588	0.515	2.7
P91 WM	8.408x10 ⁻²⁶	9.728	0	7.354x10 ⁻²⁸	13.667	9.751	0.620	6.0
P91 HAZ	6.740x10 ⁻²⁹	9.702	0	1.123x10 ⁻¹⁶	9.747	5.914	0.490	3.6

5.3 CCG Predictions by Damage Models

Damage mechanics have been used to predict creep crack growth (CCG) in P91 weldment CT specimens. In order to simulate the actual CT specimens, reported in Chapter 4, FE analyses were conducted by examining 2D FE model of a CT specimen with $W = 25$ mm, $B = 12.5$ mm for $a/W = 0.50$ and using a fine-meshed model as presented in Figure 5-9,

of mesh size at the crack tip is approximately 0.010 mm, which is similar to the grain size of the P91 steel examined. All finite element analyses were conducted using ABAQUS 6.14-1 and a typical fine mesh with 1327 elements were used with 4204 nodes. Two methods for modelling crack extension were considered. The first, is The 2D CT growing crack model considered in Section 5.1.3 will be identified as the fixed-node model, considers that the crack has propagated when damage ω , as derived from equations (10)–(12), reaches 0.999 at two integration points ahead of the crack tip. There is no change in the boundary conditions and the damage parameter simply acts as an indicator to locate the position of the crack tip as damage spreads throughout the specimen. In the second method, identified as the node-release model, the node at the crack tip is released when ω reaches 0.999 and as a result the crack propagates through the mesh along the axis of symmetry. Figure 5-16 shows a typical damage contours for a two-dimensional elastic–plastic creep damage analysis using the node-release method, in a typical plane strain analyses. SDV1 stands for the first solution dependent state variable, which denotes the damage variable ω . It can be seen that the damage zone is accumulated ahead of the initial crack tip so that the crack grows in the symmetric plane.

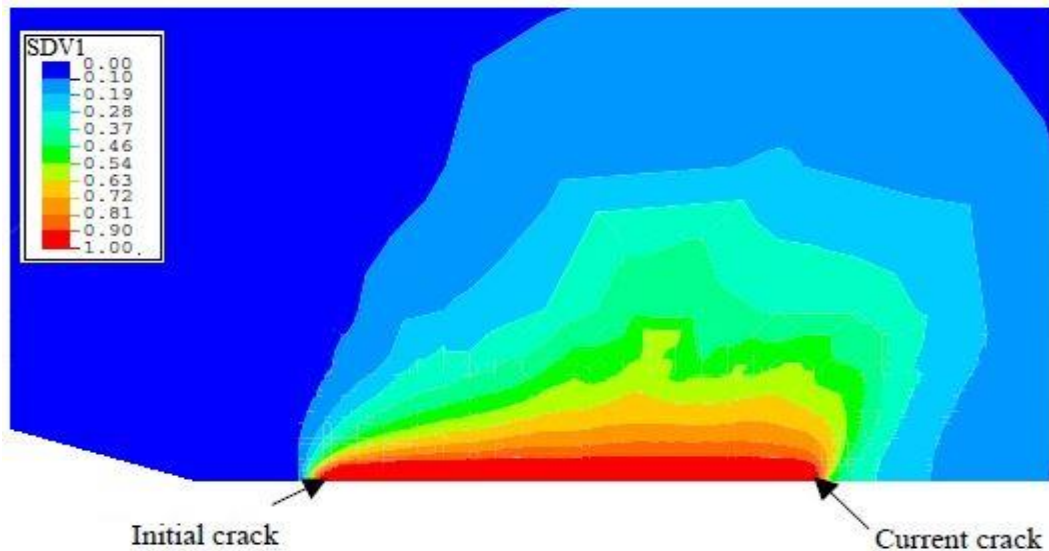


Figure 5-16 Damage contour plot for creep analysis using the node release model

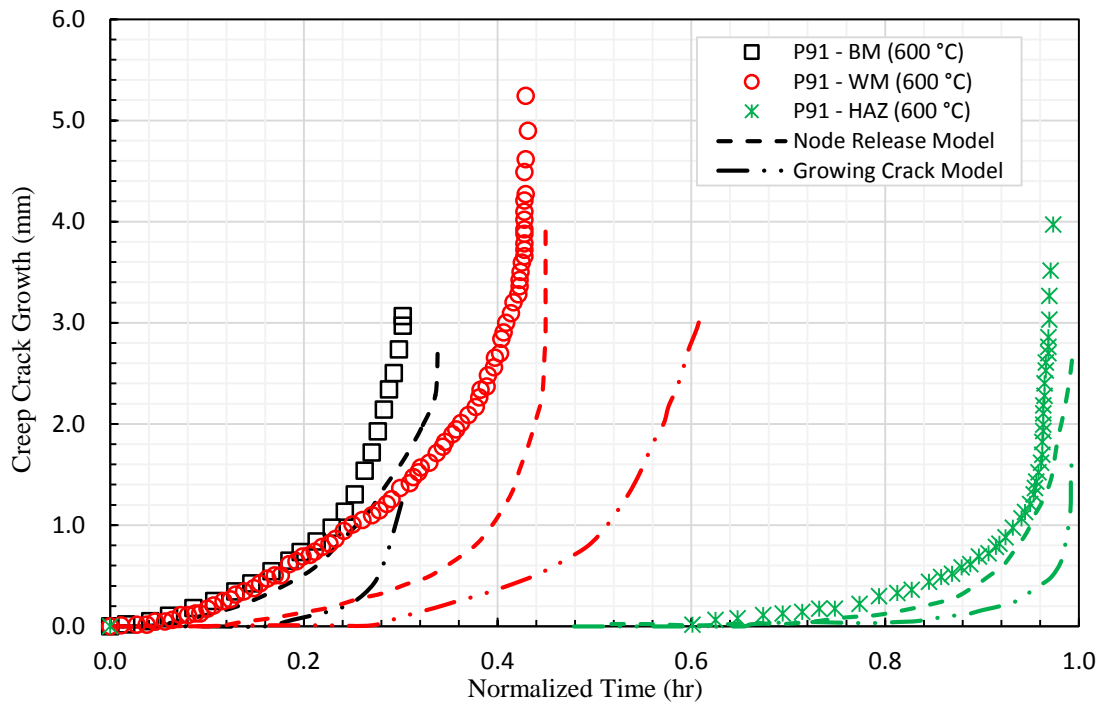


Figure 5-17 Predicted crack growth for node-release and growing crack models

The difference in the predicted creep crack growth with time for the two models as presented in Figure 5-19 for the applied load is 3 kN. The experimental data for BM, WM, and HAZ of P91 are also shown for comparison, therefore the extent of crack growth predicted by the node-release model is greater than that from the growing crack model, and is closer to the experimental data. However, in all cases the predicted amount of crack growth is less than that observed in the experiments.

Using 3D CT models, which have the same geometry and dimensions as the tested CT specimens. Another reason to use the 3D models is that the FE results are more sensitive to whether plane strain elements or plane stress elements were used. The FE analyses were carried out at the same loads as those used for the experiments. The appropriate boundary conditions were applied to the models. The Liu and Murakami damage model, presented in Section 3.3.2, was used, to obtain damage accumulation in the models In order to avoid the very high damage, and hence high strain rates which occur for the Kachanov and Rabotnov model when ω approaches unity (these can cause convergence

problems in FE creep analyses). Experimentally determined material constants were used for the P91 weldment at 600 °C.

Based on the geometry and dimensions of the CT specimen, shown in Figure 5-1, a 3D FE CT model has been created. Due to the symmetry of the CT model, only one-quarter of the specimen was modelled with half of thickness value of 6.25 mm, as shown in Figure 5-19 (a). The crack propagation is controlled by a field variable defined in the USDFLD user subroutine so that as soon as the damage reaches a value of 0.99, the elastic modulus E is gradually reduced to a unit value. With a low elastic modulus, the element is no longer able to support stresses simulating crack propagation conditions. In this simulation, side grooves were considered in order to obtain a realistic representation of the actual specimen that was used in the experimental CCG tests. For this purpose, eight nodes hexahedral elements with reduced integration were used Figure 5-19 (b) [107].

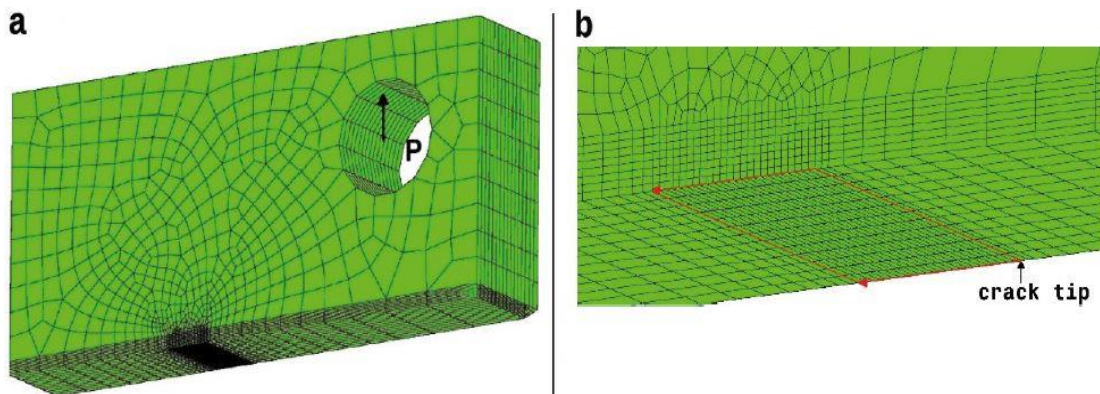


Figure 5-18 FE simulations of P91 (a) 3D model CT specimen (b) Crack tip detail [107]

The crack propagation rate da/dt as a function of the normalized C^* for the numerical simulations, the experimental results and the comparison with the $C(t)$ integral calculated using a large contour as the path surrounding the entire ligament. All the data in Figure 5-19 are plotted starting from the transient time t_r of 35 hours calculated as per definition by ASTM E1457-15 standard [3]. The transient time was also verified through the finite element analysis by evaluating the $C(t)$ integral at two different contours, one

small close to the crack tip that was automatically updated at every node release and the other significantly larger in order to include the entire ligament. The two contour integrals trend to a unique value after 30 hours of simulation demonstrating the path independence of $C(t)$ thus indicating that the steady-state creep conditions are reached quickly under these test conditions. A significant similarity was found between the experimental data and the 3D simulations at large crack sizes leading to the similar final crack front. On the other hand, the 2D-simulation shows considerable differences in the calculated C^* and the numerical $C(t)$ integral. However, numerical simulations and experimental data suggest that the relationship between crack propagation rate da/dt and C^* is not unique as seen in both experiments and simulations [107].

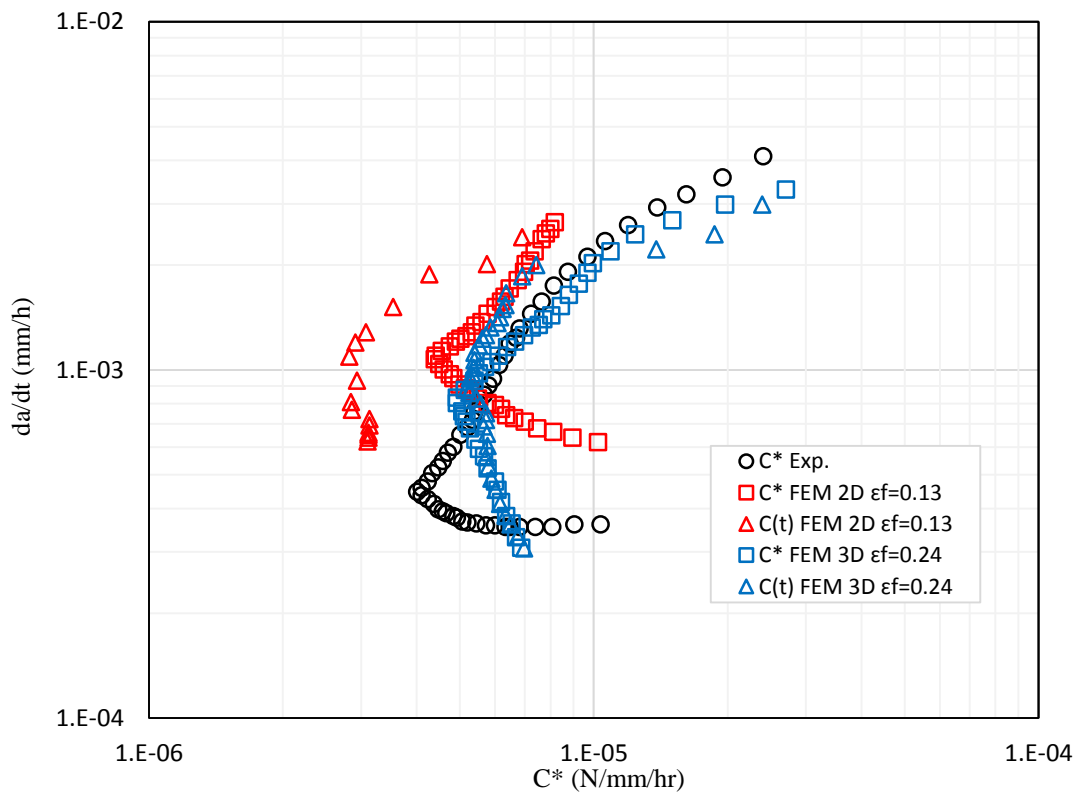


Figure 5-19 FE simulation results of C^* and comparison with the experimental CCG data [107]

6 CONCLUSIONS AND RECOMMENDATIONS

In the power generation and nuclear industries, predicting the life of aging equipment has become both a safety issue and an economic necessity. Processes such as creep crack initiation and growth limit the lifetime of components operating at high temperatures in the range of 500-650 °C. Due to the existence of welding residual stresses and inhomogeneous properties in weldments, defects may initially exist and propagate in this region of the weldment. For this reason, research work on the creep behavior of welds in structural components is of great importance and has been carried out in our study.

This thesis dealt with the study of the creep crack growth, creep damage modelling and resistance properties of P91 (9Cr1Mo-NbV) power plant steel. The methodological approach used in this work was strongly focused on the application of time-dependent fracture mechanics concepts in creep behavior to structures with the aim to:

- Present a critical review of the classical approaches to high temperature assessments of steel structures under creep conditions.
- Examine in detail the experimental procedures of creep flow, creep crack initiations and growth testing of P91 weldment material and analysis of results data reached.
- Study a numerical approach to simulate time-dependent crack propagation in components by means of accurate FE analyses.

The starting point was the understanding of the crack tip parameters that govern the initiation and propagation of defects under creep conditions, and their transposition to large scale components in order to analyze the effects of critical operating conditions, as high temperatures and stresses. In addition to this, the finite element method was used to recreate not only the experimental test conditions but also the crack tip parameters evolution in order to validate its application to estimate the residual life of components.

In this thesis, the results of creep and creep crack growth (CCG) tests, which were conducted on P91 welds, are reported. These tests were carried out on welds constituents, i.e. base metal (BM) and weld metal (WM), and heat affected zone (HAZ), for the P91

material at 600°C. For the cross-weld tests, interest was focused on the Type IV region, a narrow zone at one end of the heat affected zone (HAZ) at the side of the BM. The importance of the distinct weld zones on the creep rupture strength of various stresses and crack extensions has also been investigated. Also reported, in this thesis, are the results of the Finite Element analyses for predicting the creep and creep crack growth in the P91 weldment.

C* has successfully correlated creep crack growth behavior of the P91 steel weldment for CT specimen, because it is consistent with the time-dependent failure mechanism that prevails at operating temperatures. The results of experimental observations generally show significant differences in the creep properties in weldment zones with different microstructure. Thus, HAZ has higher creep strain rate and less time to rupture comparing to the same characteristics of base material and weld metal. In general, results of finite element creep modeling predicted the critical damage accumulation and further rupture with crack initiation in the fine-grained and inter-critical HAZ. Such a type of fracture agrees with the experiments, and the weldment crack location is of type IV. However, failures due to cracks within the weld metal have been encountered in practice, these cracks have types I and II in the classification scheme for damage types in weldments. The existence of the weldment zones can drastically reduce the creep life of the welded connection compared to a homogeneous component. Typical reductions in predicted steady-state creep rupture life of about 75 %.

The experimental results obtained for the P91 steel weldment at 600 °C, that are presented in Chapter 4 have been shown to be able to be used to obtain a full set of material constants, for a variety of creep models, including the Norton's law, Kachanov and Rabotnov model introduced in Section 3.3.1 and the Liu and Murakami model presented in Section 3.3.2

A three material representation i.e. the base metal, the weld metal and the weakest HAZ, were chosen to model creep flow and damage behavior of weldments. Therefore, finite element (FE) calculations were performed with using the models fitted for the three materials. The results of FE calculations exhibits a quite good agreement with

experiments on cross-weld specimens. It was finally shown that the model could be used to predict the creep lifetime of industrial components.

The discussion on FE model performed in Chapter 5 is based on a 2D axi-symmetric model. 3D FEM model could be used to examine the entire creep curves. However, this route would only be advisable once there is increased confidence in the material properties used. In addition, since creep damage is significantly sensitive to creep ductility and geometrical constraint, further understanding of the role of ductility dependency on the model is needed by modelling different shapes of specimens with different material properties. Further specific tests can provide reliable creep ductility examination which will assist in the life assessment of structural components. Furthermore, modelling and meshing improvements, for example simulating actual grain shapes and sizes may allow a more realistic approach to predict these cracks.

In summary, it is possible to successfully predict CCG in cracked bodies using a damage mechanics approach. This requires accurate material properties and an appropriate material damage model. The Liu/Murakami damage model has been found to be suitable for use in predicting CCG in cracked bodies. Further, both the notched bar and the CT specimens approaches can be used to define the material multiaxiality parameter α .

Improving the creep strength of weldments is a great challenge. Indeed, it was shown that even if the creep strength of the base metal is improved the gap in creep strength between the base metal and the weldment is still high. The solutions to limit the loss of creep strength due to welding are obviously the optimization of the post weld heat treatment. A normalizing treatment of the welded components would be the best way to improve the weldment creep strength but this operation is hardly realizable on industrial components. The half tempering procedure which consists in a tempering of the base metal in the temperature range between 600°C and 650°C and a post weld heat treatment at 750°C is also probably quite interesting.

7 References

- [1] T. H. Hyde and W. Sun, "Creep of Welded Structures," vol. 212, no. May, pp. 171–182, 2001.
- [2] U. Ceyhan, "High Temperature Deformation and Fracture Assessment of Similar Steel Welds," Technical University Clausthal, Germany, 2006.
- [3] S. T. Method, "Standard Test Method for Measurement of Creep Crack Growth Times in Metals 1," vol. 2, pp. 1–27, 2015.
- [4] T. H. Hyde, W. Sun, and J. A. Williams, "Creep analysis of pressurized circumferential pipe weldments - A review," *J. Strain Anal. Eng. Des.*, vol. 38, no. 1, pp. 1–30, 2003.
- [5] A. Sedmak, M. Swei, and B. Petrovski, "Creep crack growth properties of P91 and P22 welded joints," *Fatigue Fract. Eng. Mater. Struct.*, vol. 40, no. 8, pp. 1267–1275, 2017.
- [6] J. Brozda and M. Zeman, "Weldability of 9Cr-1Mo-Nb, V P91 steel intended for service in the power industry," *Weld. Int.*, vol. 10, no. 5, pp. 370–380, 1996.
- [7] J. Q. Zhang, B. Y. Yao, T. J. Li, F. G. Liu, and Y. L. Zhang, "Numerical simulation of mechanical controlling parameters for Type IV cracking on the welding joints of martensitic heat-resistant steel," *Front. Mater. Sci. China*, vol. 4, no. 2, pp. 210–216, 2010.
- [8] F. Abe, T.-U. Kern, and R. Viswanathan, *Creep-resistant steels*, 1st ed. Cambridge, England: Woodhead Publishing; CRC Press, 2008.
- [9] J. A. Francis, W. Mazur, and H. K. D. H. Bhadeshia, "Review Type IV cracking in ferritic power plant steels," *Mater. Sci. Technol.*, vol. 22, no. 12, pp. 1387–1395, 2006.
- [10] K. Nicol, *High temperature steels in pulverised coal technology High temperature steels in pulverised coal technology*, no. April. 2014.
- [11] A. Shibli, "Aberrant P91 and its inspection, monitoring and life assessment," *Mater. High Temp.*, vol. 34, no. 5–6, pp. 442–447, 2017.
- [12] D. M. Madyira, J. A. Liebenberg, and A. Kaymacki, "Comparative Characterization of P91 and 10CrMo9-10 Creep Resistant Steel Welds," *Procedia Manuf.*, vol. 8, no. October 2016, pp. 345–352, 2017.
- [13] B. Dogan, "Creep Deformation and Failure Assessment of Steel Weldments," in *Volume 9: Eighth International Conference on Creep and Fatigue at Elevated Temperatures*, 2007, pp. 299–305.
- [14] K. M. Nikbin, "The role of defect assessment in elevated temperature component design and remaining life estimation codes," in *CREEP7*, 2001, pp. 123–130.
- [15] H. Riedel, *Fracture at High Temperatures*. Berlin, Heidelberg: Springer Berlin Heidelberg, 1987.

- [16] G. . Webster and R. . Ainsworth, *High Temperature Component Life Assessment*. Dordrecht: Springer Netherlands, 1994.
- [17] M. Yatomi and M. Tabuchi, "Issues relating to numerical modelling of creep crack growth," *Eng. Fract. Mech.*, vol. 77, no. 15, pp. 3043–3052, 2010.
- [18] L. Zhao, H. Jing, L. Xu, Y. Han, and J. Xiu, "Analysis of creep crack growth behavior of P92 steel welded joint by experiment and numerical simulation," *Mater. Sci. Eng. A*, vol. 558, pp. 119–128, 2012.
- [19] X. Ling, S.-T. Tu, and J.-M. Gong, "Damage Mechanics Considerations for Life Extension of High-Temperature Components," *J. Press. Vessel Technol.*, vol. 122, no. 2, pp. 174–179, 2000.
- [20] S. H. Wang, D. K. Matlock, and D. L. Olson, "High Temperature Impression Creep Testing of Weldments," *Weld. Res.*, pp. 153–158, 1985.
- [21] "Advanced Creep - European Creep Collaborative Committee (ECCC)." [Online]. Available: <http://www.ommi.co.uk/etd/eccc/advancedcreep/com.html>. [Accessed: 26-Nov-2017].
- [22] N. Taylor, M. Kocak, and S. Webster, "European Fitness-for-service Network," *Fitnet*, p. 127, 2006.
- [23] H. Tada, P. C. Paris, and G. R. Irwin, *The Stress Analysis of Cracks Handbook, Third Edition*. ASME Press, 2000.
- [24] S. Al Laham and S. Branch, "Stress intensity factor and limit load handbook," *Br. Energy Gener.*, no. 2, 1999.
- [25] T. L. Anderson, *Fracture Mechanics: Fundamentals and Applications*, 3rd ed. CRC Press, 2004.
- [26] F. M. Burdekin and D. E. W. Stone, "The crack opening displacement approach to fracture mechanics in yielding materials," *J. Strain Anal. Eng. Des.*, vol. 1, no. 2, pp. 145–153, 1966.
- [27] J. R. Rice and G. F. Rosengren, "Plane strain deformation near a crack tip in a power-law hardening material," *J. Mech. Phys. Solids*, vol. 16, no. 1, pp. 1–12, 1968.
- [28] J. R. Rice, "A Path Independent Integral and the Approximate Analysis of Strain Concentration by Notches and Cracks," *J. Appl. Mech.*, vol. 35, no. 2, p. 379, 1968.
- [29] J. W. Hutchinson, "Plastic stress and strain fields at a crack tip," *J. Mech. Phys. Solids*, vol. 16, no. 5, pp. 337–342, 1968.
- [30] J. W. Hutchinson, "Singular behaviour at the end of a tensile crack in a hardening material," *Journal of the Mechanics and Physics of Solids*, vol. 16, no. 1. pp. 13–31, 1968.
- [31] H. Zhou, F. Biglari, C. M. Davies, A. Mehmanparast, and K. M. Nikbin, "Evaluation of fracture mechanics parameters for a range of weldment geometries with different mismatch ratios," *Eng. Fract. Mech.*, vol. 124–125, pp. 30–51, 2014.

- [32] C. M. Davies, M. Kourmpetis, N. P. O 'dowd, K. M. Nikbin, N. Reno, and R. E. Link, "Experimental Evaluation of the J or C* Parameter for a Range of Cracked Geometries," *J. ASTM Int. Pap. ID JAI13221*, vol. 314, no. 11, pp. 14–2017, 2006.
- [33] X. T. Miao, C. Y. Zhou, and X. H. He, "Analysis of Limit Loads for CT Specimens with Cracks Based on Extended Finite Element Method," *Procedia Eng.*, vol. 130, pp. 763–774, 2015.
- [34] R. A. Ainsworth, "The assessment of defects in structures of strain hardening material," *Eng. Fract. Mech.*, vol. 19, no. 4, pp. 633–642, 1984.
- [35] M. F. Ashby, D. R. H. Jones, and C. 21, "Chapter 21 - Kinetic Theory of Diffusion," in *Engineering Materials 1 (Fourth Edition)*, 4th ed., Elsevier, 2012, pp. 325–336.
- [36] B. Farahmand, *Virtual testing and predictive modeling: For fatigue and fracture mechanics allowables*, 1st ed. Kirkland, Washington: Springer US, 2009.
- [37] S. R. Holdsworth *et al.*, "Factors influencing creep model equation selection," *Int. J. Press. Vessel. Pip.*, vol. 85, no. 1–2, pp. 80–88, 2008.
- [38] M. Yatomi, K. M. Nikbin, and N. P. O'Dowd, "Creep crack growth prediction using a damage based approach," *Int. J. Press. Vessel. Pip.*, vol. 80, no. 7–8, pp. 573–583, 2003.
- [39] A. Strang, *Materials for high temperature power generation and process plant applications*, 1st ed. Whitehurst & Clark, 2000.
- [40] J. C. Vaillant, B. Vandenberghe, B. Hahn, H. Heuser, and C. Jochum, "T/P23, 24, 911 and 92: New grades for advanced coal-fired power plants-Properties and experience," *Int. J. Press. Vessel. Pip.*, vol. 85, no. 1–2, pp. 38–46, 2008.
- [41] K. S. Chandravathi, K. Laha, K. B. S. Rao, and S. L. Mannan, "Microstructure and tensile properties of modified 9Cr-1Mo steel (grade 91)," *Mater. Sci. Technol.*, vol. 17, no. May, pp. 559–565, 2001.
- [42] J. W. Hutchinson, "Fundamentals of the Phenomenological Theory of Nonlinear Fracture Mechanics," *J. Appl. Mech.*, vol. 50, no. 4b, p. 1042, 1983.
- [43] W. Ramberg and W. R. Osgood, "Description of stress-strain curves by three parameters.pdf," *National Advisory Committee For Aeronautics*. p. Technical Note No. 902, 1943.
- [44] H. F. Chen, Y. H. Liu, Z. Z. Cen, and B. Y. Xu, "On the solution of limit load and reference stress of 3-D structures under multi-loading systems," *Eng. Struct.*, vol. 21, no. 6, pp. 530–537, 1999.
- [45] A. Saxena, "Creep crack growth in high temperature ductile materials," *Eng. Fract. Mech.*, vol. 40, no. 4–5, pp. 721–736, 1991.
- [46] R. Viswanathan, *Damage Mechanisms and Life Assessment of High Temperature Components*, 2nd ed. ASM INTERNATIONAL, 1989.
- [47] N. L. Goldman and J. W. Hutchinson, "Fully plastic crack problems: The center-cracked

- strip under plane strain," *Int. J. Solids Struct.*, vol. 11, no. 5, pp. 575–591, 1975.
- [48] K. M. Nikbin, D. J. Smith, and G. a. Webster, "Prediction of Creep Crack Growth from Uniaxial Creep Data," *Proc. R. Soc. A Math. Phys. Eng. Sci.*, vol. 396, no. 1810, pp. 183–197, 1984.
- [49] A. SAXENA, "Creep crack growth in high temperature ductile materials☆," *Eng. Fract. Mech.*, vol. 40, no. 4–5, pp. 721–736, 1991.
- [50] M. Yatomi, C. M. Davies, and K. M. Nikbin, "Creep crack growth simulations in 316H stainless steel," *Eng. Fract. Mech.*, vol. 75, no. 18, pp. 5140–5150, 2008.
- [51] D. R. Tobergte and S. Curtis, "Comparison of creep initiation and growth in four steels tested in HIDA," *J. Chem. Inf. Model.*, vol. 53, no. 9, pp. 1689–1699, 2013.
- [52] M. Yatomi, N. P. O'Dowd, K. M. Nikbin, and G. A. Webster, "Theoretical and numerical modelling of creep crack growth in a carbon-manganese steel," *Eng. Fract. Mech.*, vol. 73, no. 9, pp. 1158–1175, 2006.
- [53] S. Maleki, Y. Zhang, and K. Nikbin, "Prediction of creep crack growth properties of P91 parent and welded steel using remaining failure strain criteria," *Eng. Fract. Mech.*, vol. 77, no. 15, pp. 3035–3042, 2010.
- [54] R. A. Ainsworth, "The initiation of creep crack growth," *Int. J. Solids Struct.*, vol. 18, no. 10, pp. 873–881, 1982.
- [55] C. M. Stewart and A. P. Gordon, "Analytical Method to Determine the Tertiary Creep Damage Constants of the Kachanov-Rabotnov Constitutive Model," *Vol. 9 Mech. Solids, Struct. Fluids*, pp. 177–184, 2010.
- [56] K. Naumenko and H. Altenbach, *Modeling of creep for structural analysis. Foundations of Engineering Mechanics*. 2007.
- [57] D. Hayhurst, P. Brown, and C. Morrison, "The Role of Continuum Damage in Creep Crack-Growth," *Philos. Trans. R. Soc. a-Mathematical Phys. Eng. Sci.*, vol. 311, no. 1516, p. 131–+, 1984.
- [58] C.-S. Oh, N.-H. Kim, S.-H. Min, and Y.-J. Kim, "Finite Element Damage Analyses for Predictions of Creep Crack Growth," *ASME 2010 Press. Vessel. Pip. Conf. Vol. 6, Parts A B*, pp. 331–335, 2010.
- [59] L. Kachanov, "Rupture Time Under Creep Conditions," *Int. J. Fract.*, vol. 97, no. 8, pp. 11–18, 1999.
- [60] Y. N. Rabotnov, "Creep rupture," *Proc. TWELFTH Int. Congr. Appl. Mech.*, pp. 342–349, 1968.
- [61] C. M. Stewart and A. P. Gordon, "Constitutive Modeling of Multistage Creep Damage in Isotropic and Transversely Isotropic Alloys With Elastic Damage," *J. Press. Vessel Technol.*, vol. 134, no. 4, p. 41401, 2012.

- [62] T. H. Hyde, M. Saber, and W. Sun, "Testing and modelling of creep crack growth in compact tension specimens from a P91 weld at 650°C," *Eng. Fract. Mech.*, vol. 77, no. 15, pp. 2946–2957, 2010.
- [63] D. François, A. Pineau, and A. Zaoui, *Mechanical Behaviour of Materials*, vol. 191. Dordrecht: Springer Netherlands, 2013.
- [64] Y. Liu and S. Murakami, "Damage Localiztion of Conventional Creep Damage Models and Proposition of a New Model for Creep Damage Analysis," *JSME Int. J.*, vol. 41, no. 1, pp. 57–66, 1998.
- [65] S. Murakami and Y. Liu, "Mesh-Dependence in Local Approach to Creep Fracture," *Int. J. Damage Mech.*, vol. 4, no. 3, pp. 230–250, 1995.
- [66] A. C. F. Cocks and M. F. Ashby, "Integranular fracture during power-law creep under multiaxial stresses," *Met. Sci.*, no. September, pp. 395–402, 1980.
- [67] J. F. Wen and S. T. Tu, "A multiaxial creep-damage model for creep crack growth considering cavity growth and microcrack interaction," *Eng. Fract. Mech.*, vol. 123, pp. 197–210, 2014.
- [68] T. H. Hyde, M. Saber, and W. Sun, "Creep crack growth data and prediction for a P91 weld at 650 °C," *Int. J. Press. Vessel. Pip.*, vol. 87, no. 12, pp. 721–729, 2010.
- [69] T. H. Hyde, L. Xia, and A. A. Becker, "Prediction of creep failure in aeroengine materials under multi-axial stress states," *Int. J. Mech. Sci.*, vol. 38, no. 4, pp. 385–403, Apr. 1996.
- [70] T. H. Hyde, W. Sun, and A. Tang, "Determination of material constants in creep continuum damage constitutive equations," *Strain*, vol. 34, no. 3, pp. 83–90, 1998.
- [71] T. H. Hyde, M. Saber, and W. Sun, "Testing and modelling of creep crack growth in compact tension specimens from a P91 weld at 650°C," *Eng. Fract. Mech.*, vol. 77, no. 15, pp. 2946–2957, 2010.
- [72] M. Saber, D. W. J. Tanner, W. Sun, and T. H. Hyde, "Determination of creep and damage properties for P92 at 675°C," *J. Strain Anal. Eng. Des.*, vol. 46, no. 8, pp. 842–851, 2011.
- [73] D. W. J. Tanner, A. A. Becker, and T. H. Hyde, "High temperature life prediction of a welded IN718 component," *J. Phys. Conf. Ser.*, vol. 181, no. 1, 2009.
- [74] T. H. Hyde, A. A. Becker, W. Sun, A. Yaghi, J. A. Williams, and S. Concari, "Determination of Creep Properties for P91 Weldment Materials At 625°C," *5th Int. Conf. Mech. Mater. Des.*, pp. 1–13, 2006.
- [75] C. J., W. Sun, T. H., M. Saber, and A. A., "Application of the Liu and Murakami Damage Model for Creep Crack Growth Predictions in Power Plant Steels," in *Computational and Numerical Simulations*, InTech, 2014.
- [76] Dassault Systèmes Simulia Corp., "Analysis User's Manual Volume 1: Introduction, Spatial modeling, execution and output," *Abaqus 6.12*, vol. I, p. 831, 2012.

- [77] K. Hibbitte, "ABAQUS user subroutines reference manual," *Hks Inc*, 2005.
- [78] G. Eggeler *et al.*, "Analysis of creep in a welded {P91} pressure-vessel," *Int. J. Press. Vessel. Pip.*, vol. 60, no. 3, pp. 237–257, 1994.
- [79] B. Dogan, K. Nikbin, B. Petrovski, U. Ceyhan, and D. W. Dean, "Code of practice for high-temperature testing of weldments," *Int. J. Press. Vessel. Pip.*, vol. 83, no. 11–12, pp. 784–797, 2006.
- [80] B. Dogan and B. Petrovski, "Creep crack growth of high temperature weldments," *Int. J. Press. Vessel. Pip.*, vol. 78, no. 11–12, pp. 795–805, 2001.
- [81] R. C. Rd and G. Potirniche, "Prediction and Monitoring Systems of Creep-Fracture Behavior of 9Cr- 1Mo Steels for Reactor Pressure Vessels," no. 9, 2013.
- [82] S. Holmström, "Defining a negligible creep temperature curve for Gr. 91 steel," *Int. J. Press. Vessel. Pip.*, vol. 146, pp. 198–202, 2016.
- [83] E1457-07e4, "Standard Test Method for Measurement of Creep Crack Growth Times in Metals," *ASTM B. Stand.*, vol. 2, pp. 1–24, 2007.
- [84] A. Saxena, "Nonlinear Fracture Mechanic for Engineering." p. 472, 1998.
- [85] ASTM Standard E647 – 13a, "Standard Test Method for Measurement of Fatigue Crack Growth Rates," *Am. Soc. Test. Mater.*, pp. 1–50, 2014.
- [86] K. Van Minnebruggen, S. Hertelé, M. A. Verstraete, and W. De Waele, "Crack growth characterization in single-edge notched tension testing by means of direct current potential drop measurement," *Int. J. Press. Vessel. Pip.*, vol. 156, pp. 68–78, 2017.
- [87] M. Swei *et al.*, "Creep crack growth behavior of P91 steel weldments," *Therm. Sci.*, no. 0, pp. 240–240, 2017.
- [88] H. Y. Lee, W. G. Kim, and N. H. Kim, "Behavior of Grade 91 material specimens with and without defect at elevated temperature," *Int. J. Press. Vessel. Pip.*, vol. 125, pp. 3–12, 2015.
- [89] C. M. Davies, D. W. Dean, K. M. Nikbin, and N. P. O'Dowd, "Interpretation of creep crack initiation and growth data for weldments," *Eng. Fract. Mech.*, vol. 74, no. 6, pp. 882–897, 2007.
- [90] T. S. P. Austin and G. A. Webster, "Prediction of Creep Crack Growth Incubation Periods," *Fatigue Fract. Eng. Mater. Struct.*, vol. 15, no. 11, pp. 1081–1090, 1992.
- [91] B. Dogan, B. Petrovski, and U. Ceyhan, "Crack initiation and defect assessment at high temperatures," vol. 85, no. 1, pp. 0–4.
- [92] B. Dogan, U. Ceyhan, and B. Petrovski, "SIGNIFICANCE OF CREEP CRACK INITIATION FOR DEFECT ASSESSMENT," vol. 85, no. 1, pp. 62–70, 2006.
- [93] K. M. Nikbin, G. A. Webster, and D. J. Smith, "An engineering approach to the prediction

- of creep crack growth," *ASME, Trans. J. Eng. Mater. Technol.*, vol. 108, no. April 1986, pp. 186–191, 1986.
- [94] M. Manjgo, "Behaviour of P91 Steel Simulated Haz At 600°C," *Int. Res. Conf.*, no. September, pp. 161–164, 2011.
- [95] R. a. Ainsworth, D. G. Hooton, and D. Green, "Failure assessment diagrams for high temperature defect assessment," *Eng. Fract. Mech.*, vol. 62, no. 1, pp. 95–109, 1999.
- [96] F. Karlsruhe, W. Berichte, and F. Report, "Defect assessment procedures for high temperature applications," 2009.
- [97] J. Ewald, S. Sheng, A. Klenk, and G. Schellenberg, "Engineering guide to assessment of creep crack initiation on components by Two-Criteria-Diagram," *Int. J. Press. Vessel. Pip.*, vol. 78, no. 11, pp. 937–949, 2001.
- [98] F. A. Leckie and D. R. Hayhurst, "Constitutive equations for creep rupture," *Acta Metall.*, vol. 25, no. 9, pp. 1059–1070, 1977.
- [99] D. Petersen, G. Belloni, E. Gariboldi, A. Lo Conte, M. Tono, and P. Speranzoso, "On the Experimental Calibration of a Potential Drop System for Crack Length Measurements in a Compact Tension Specimen," *J. Test. Eval.*, vol. 30, no. 6, p. 11149, 2002.
- [100] C. M. Davies, N. P. O'Dowd, K. M. Nikbin, and G. A. Webster, "An analytical and computational study of crack initiation under transient creep conditions," *Int. J. Solids Struct.*, vol. 44, no. 6, pp. 1823–1843, 2007.
- [101] C. S. Oh, N. H. Kim, Y. J. Kim, J. H. Baek, Y. P. Kim, and W. S. Kim, "A finite element ductile failure simulation method using stress-modified fracture strain model," *Eng. Fract. Mech.*, vol. 78, no. 1, pp. 124–137, 2011.
- [102] L. Xia, A. A. Becker, and T. H. Hyde, "An Assessment of the C* and KI Parameters for Predicting Creep Crack Growth in a Ni-Base Superalloy (Waspaloy) at 700°C," *Int. J. Fract.*, vol. 92, no. 1, pp. 39–54, 1998.
- [103] S. Halighongde, A. A. Becker, and T. H. Hyde, "Finite Element Analysis of creep crack growth using the C* parameter in multi-domain problems," *International Conf. Comput. Civ. and Build. Eng.*, no. 1, pp. 1–6, 2010.
- [104] Y. K. Park, K. S. Kim, Y. K. Chung, and J. J. Park, "Creep Crack Growth in X20CrMoV 12 1 Steel and Its Weld Joint," *J. Press. Vessel Technol.*, vol. 123, no. 2, p. 191, 2001.
- [105] I. A. Shibli, "Performance of P91 Thick Section Welds Under Steady and Cyclic Loading Conditions : Power Plant and Research Experience," *Ommi*, vol. 1, no. 3, pp. 1–17, 2002.
- [106] J. Bolton, "A 'characteristic-strain' model for creep," *Mater. High Temp.*, vol. 25, no. 3, pp. 197–204, 2008.
- [107] A. Saxena *et al.*, "Experimental and simulated displacement in cracked specimen of P91 steel under creep conditions," *Procedia Struct. Integr.*, vol. 2, pp. 911–918, 2016.

Прилог 1.

Изјава о ауторству

Потписани-а Мохамед Етоухами Свеи

број индекса Д1/2014

Изјављујем

да је докторска дисертација под насловом

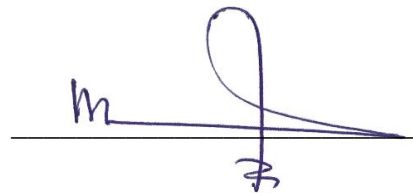
CREEP CRACK GROWTH IN STEEL WELDED JOINTS

РАСТ ПРСЛИНЕ УСЛЕД ПУЗАЊА У ЗАВАРЕНИМ СПОЈЕВИМА ОД ЧЕЛИКА

- резултат сопственог истраживачког рада,
- да предложена дисертација у целини ни у деловима није била предложена за добијање било које дипломе према студијским програмима других високошколских установа,
- да су резултати коректно наведени и
- да нисам кршио/ла ауторска права и користио интелектуалну својину других лица.

Потпис докторанда

У Београду, 15.05.2018



Прилог 2.

Изјава о истоветности штампане и електронске
верзије докторског рада

Име и презиме аутора Мохамед Етоухами Свеи

Број индекса Д1/2014

Студијски програм Докторске студије

Наслов рада CREEP CRACK GROWTH IN STEEL WELDED JOINTS

РАСТ ПРСЛИНЕ УСЛЕД ПУЗАЊА У ЗАВАРЕНИМ СПОЈЕВИМА ОД ЧЕЛИКА

Ментор Александар Седмак

Потписани/а Мохамед Етоухами Свеи

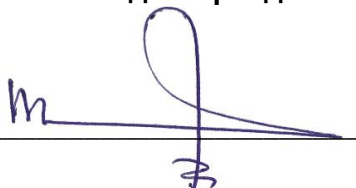
Изјављујем да је штампана верзија мог докторског рада истоветна електронској верзији коју сам предао/ла за објављивање на порталу **Дигиталног репозиторијума Универзитета у Београду**.

Дозвољавам да се објаве моји лични подаци везани за добијање академског звања доктора наука, као што су име и презиме, година и место рођења и датум одбране рада.

Ови лични подаци могу се објавити на мрежним страницама дигиталне библиотеке, у електронском каталогу и у публикацијама Универзитета у Београду.

Потпис докторанда

У Београду, 15.05.2018



Прилог 3.

Изјава о коришћењу

Овлашћујем Универзитетску библиотеку „Светозар Марковић“ да у Дигитални репозиторијум Универзитета у Београду унесе моју докторску дисертацију под насловом:

CREEP CRACK GROWTH IN STEEL WELDED JOINTS

РАСТ ПРСЛИНЕ УСЛЕД ПУЗАЊА У ЗАВАРЕНИМ СПОЈЕВИМА ОД ЧЕЛИКА

која је моје ауторско дело.

Дисертацију са свим прилозима предао/ла сам у електронском формату погодном за трајно архивирање.

Моју докторску дисертацију похрањену у Дигитални репозиторијум Универзитета у Београду могу да користе сви који поштују одредбе садржане у одабраном типу лиценце Креативне заједнице (Creative Commons) за коју сам се одлучио/ла.

1. Ауторство
2. Ауторство - некомерцијално
3. Ауторство – некомерцијално – без прераде
4. Ауторство – некомерцијално – делити под истим условима
5. Ауторство – без прераде
6. Ауторство – делити под истим условима

(Молимо да заокружите само једну од шест понуђених лиценци, кратак опис лиценци дат је на полеђини листа).

У Београду, _____ 15.05.2018. _____

Потпис докторанда

1. Ауторство - Дозвољаваате умножавање, дистрибуцију и јавно саопштавање дела, и прераде, ако се наведе име аутора на начин одређен од стране аутора или даваоца лиценце, чак и у комерцијалне сврхе. Ово је најслободнија од свих лиценци.
2. Ауторство – некомерцијално. Дозвољаваате умножавање, дистрибуцију и јавно саопштавање дела, и прераде, ако се наведе име аутора на начин одређен од стране аутора или даваоца лиценце. Ова лиценца не дозвољава комерцијалну употребу дела.
3. Ауторство - некомерцијално – без прераде. Дозвољаваате умножавање, дистрибуцију и јавно саопштавање дела, без промена, преобликовања или употребе дела у свом делу, ако се наведе име аутора на начин одређен од стране аутора или даваоца лиценце. Ова лиценца не дозвољава комерцијалну употребу дела. У односу на све остале лиценце, овом лиценцом се ограничава највећи обим права коришћења дела.
4. Ауторство - некомерцијално – делити под истим условима. Дозвољаваате умножавање, дистрибуцију и јавно саопштавање дела, и прераде, ако се наведе име аутора на начин одређен од стране аутора или даваоца лиценце и ако се прерада дистрибуира под истом или сличном лиценцом. Ова лиценца не дозвољава комерцијалну употребу дела и прерада.
5. Ауторство – без прераде. Дозвољаваате умножавање, дистрибуцију и јавно саопштавање дела, без промена, преобликовања или употребе дела у свом делу, ако се наведе име аутора на начин одређен од стране аутора или даваоца лиценце. Ова лиценца дозвољава комерцијалну употребу дела.
6. Ауторство - делити под истим условима. Дозвољаваате умножавање, дистрибуцију и јавно саопштавање дела, и прераде, ако се наведе име аутора на начин одређен од стране аутора или даваоца лиценце и ако се прерада дистрибуира под истом или сличном лиценцом. Ова лиценца дозвољава комерцијалну употребу дела и прерада. Слична је софтверским лиценцама, односно лиценцама отвореног кода.